Characterizing Artifact Generated by Passive Medical Devices in Modern Low-Field MRI: A Comparative Evaluation with Routine Clinical Practice

by

Robert Weaver

Submitted in partial fulfilment of the requirements
for the degree of Master of Applied Science

at

Dalhousie University
Halifax, Nova Scotia
November 2023

Dalhousie University is located in Mi'kma'ki, the
ancestral and unceded territory of the Mi'kmaq.
We are all Treaty people.

# Table of Contents

## List of Tables

## List of Figures

# Abstract

Following implantation of a medical device, MRI follow-up imaging is often performed to evaluate device function, assess healing, and monitor treatment progression. Metallic components in devices create artifacts that affect diagnostic image quality in MRI. Modernized low-field MRIs now entering the clinic offer theoretical advantages over 1.5 T and 3 T MRI for imaging near metal. How these theoretical advantages translate to practice remains largely untested. An artifact characterization pipeline is developed here for the systematic evaluation of metal artifact created by 0.5 T, 1.5 T and 3 T MRI systems. Three high-use passive devices are evaluated *in vitro* with routine brain imaging protocols in current clinical use at our institution. Results generally indicate reduced artifact with 0.5 T, but artifact mitigating trade-offs within 1.5/3 T protocols were found to have considerable effects. The reduced trade-offs in 0.5 T protocols suggest an advantage for imaging near metallic devices in practice.

# List of Abbreviations and Symbols Used

**Abbreviations**

| | |
|---|---|
| ANOVA | Analysis of variance |
| AP | Anterior-posterior |
| ASTM | ASTM International |
| bSSFP | Balanced steady-state free precession |
| BH | Benjamini Hochberg |
| BW | Bandwidth |
| CSF | Cerebrospinal fluid |
| DWI | Diffusion-weighted imaging |
| EPI | Echo planar imaging |
| FDA | Food and Drug Administration |
| FDR | False discovery rate |
| FE | Frequency encoding |
| FIESTA | Fast imaging employing steady-state acquisition |
| FIESTA-C | Fast imaging employing steady-state acquisition – constructive |
| FOV | Field of view |
| GRE | Gradient echo |
| iMRI | Interventional magnetic resonance imaging |
| LR | Left-right |
| MIP | Maximum intensity projection |
| MR | Magnetic resonance |
| MRI | Magnetic resonance imaging |
| nd | No discovery |
| PE | Phase encoding |
| PETG | Polyethylene terephthalate glycol |
| PGSE | Pulsed gradient spin echo |
| PROPELLER | Periodically rotated overlapping parallel lines with enhanced reconstruction |
| QA | Quality assurance |
| RF | Radiofrequency |
| ROI | Region of interest |

| | |
|---|---|
| SAR | Specific absorption rate |
| SD | Standard deviation |
| SE | Spin echo |
| SEMAC | Slice encoding for metal artifact correction |
| SNR | Signal-to-noise ratio |
| SI | Superior-inferior |
| T1 FLAIR | T1-weighted fluid attenuated inversion recovery |
| T2 FLAIR | T2-weighted fluid attenuated inversion recovery |
| T2WI | T2-weighted imaging |
| TOF-MRA | Time-of-flight magnetic resonance angiography |
| US | United States |
| VAT-SE | View angle titling - spin echo |

## Symbols

| | |
|---|---|
| $B_0$ | Main magnetic field strength |
| $B$ | Magnetic field |
| $\Delta B$ | Perturbing magnetic field |
| $e$ | Euler's number |
| $G$ | Magnetic gradient magnitude |
| $M$ | Net magnetization vector |
| $M_{xy}$ | Transverse magnetization vector |
| $M_z$ | Longitudinal magnetization vector |
| T1 | Longitudinal relaxation time constant |
| T2 | Transverse relaxation time constant |
| $\gamma$ | Gyromagnetic ratio |
| $\chi$ | Magnetic susceptibility |
| $\omega$ | Larmor frequency |
| $\omega_0$ | Larmor frequency at $B_0$ |

# Acknowledgements

# Chapter 1: Introduction

This document is divided into five chapters covering the work's various aspects. The subject is introduced in Chapter 1, and the relevant theory and background information are provided in Chapter 2. Chapter 3 and Chapter 4 offer a detailed description of the research methodology and present the results, respectively. Finally, Chapter 5 provides a discussion of the work and its conclusions.

## 1.1    Preamble

The use of magnetic resonance imaging (MRI) in the clinical setting continues to expand rapidly, with per capita MRI exams increasing by 45% in Canada over the past decade[1]. One important and growing application of MRI is for follow-up imaging to evaluate tissues near magnetic resonance (MR) conditional passive medical devices, an often challenging area to obtain sufficient diagnostic image quality[2–5]. Manufacturers of MRI scanners have recently begun to bring modernized low-field MRI systems to market, which may provide an advantage for imaging in regions with large magnetic susceptibility-induced field distortions, such as near an MR conditional device.

This work aims to contribute to the information deficit surrounding the performance of modern low-field MRI. The primary objective is to characterize the artifacts produced by three passive medical devices on a modern low-field MRI scanner and compare these results to modern mid- and high-field systems. The work presented here is completed through the lens of clinical relevancy, anchoring to pulse sequences used within the routine brain protocol for each machine. This allows for a like-for-like comparison because, in practice, pulse sequences are protocolled on the scanner where they will be used, and parameter matching is uncommon. However, one matched pulse

sequence is evaluated to provide insight into the effects of field strength alone. An artifact characterization framework is created following a United States (US) Food and Drug Administration (FDA) consensus standard for measuring metal artifacts created by passive devices on MRI images[6]. This work provides insight into the potential for low-field MRI to image near MR-conditional devices in the clinical context and incentivizes future *in vitro* and *in vivo* research.

## 1.2    Clinical MRI and Historical Context

### 1.2.1    Overview

As one of the premier medical imaging techniques, MRI is used extensively to diagnose pathology, plan medical procedures, and monitor therapies and medical conditions. This non-ionizing, non-invasive imaging modality is used to probe nearly all regions of the body. In addition to providing structural and anatomical information, the ability to differentiate soft tissues based on their composition and distinguish lesion from healthy tissues sets MRI apart[7]. MRI has also found great utility in hybrid imaging systems, such as positron emission tomography-MRI[8], and for use during interventional procedures (iMRI)[9].

An MRI scanner creates an image by exploiting the magnetic properties of atomic nuclei, most commonly hydrogen nuclei. A strong homogenous main magnetic field ($B_0$) enables radiofrequency (RF) excitation pulses generated by a transmit RF coil to generate measurable signals within the patient's body. Gradient magnet coils produce temporally and spatially varying magnetic fields in each cardinal direction. This allows for spatial encoding of this signal as it is simultaneously recorded by one or more RF receive coils. Measured signals are demodulated and reconstructed into an image using the Fourier

transform or a more advanced image reconstruction method. The elegance of MRI arises from the near-infinite ways signals may be excited, manipulated, and measured. In a musical analogy, where sheet music provides instructions for creating a sonata from a series of simple notes and chords, the term pulse sequence describes the progression of RF and gradient pulses that are played out to capture an MR image. It should be noted that this is a vast oversimplification of the process, and a more nuanced discussion is provided in Chapter 2.

Since the first clinical diagnostic whole-body MRI scan was conducted in 1980 at the University of Aberdeen[10,11], the benefits of the technology have been clear, leading to rapid advancements and new forms of the original design. Despite the multitude of variants now in clinical practice, a clinical MRI scanner can generally be described based on its shape and the strength of $B_0$. The prototypical shape factor for an MRI is closed-bore, where the main superconducting magnet, gradient coils, radiofrequency transmit coil, and other hardware are packaged into an annular shape. Patients lay on an exam table where RF receive coils are placed over the anatomic region of interest before the table is moved into the annular space of the MRI scanner for imaging. Although closed-bore is most commonly encountered, open MRI scanners, which typically use two separate parallel flat magnets, provide better in-scan access to the patient at the expense of signal-to-noise ratio (SNR)[12].

### 1.2.2 Historical Context for MRI Field Strength

Mid-field* MRI scanners with 1.5 Tesla (T) main magnetic field strengths currently

---

*MRI scanner field strength ranges defined here as follows:
ultra-low field < 0.1 T ≤ low-field < 1 T ≤ mid-field < 3 T ≤ high-field < 7 T ≤ ultra-high field

dominate the clinical landscape. These workhorse machines became the industry standard in the 1990s. Operating at 1.5 T represents a 107-fold increase in magnetic field strength over the now-historical scanner from Aberdeen. Due to the proportionality observed between signal amplitude and $B_0$, advancing towards higher field strengths has long been desirable. High-field systems, typically operating at 3 T, also comprise a sizeable portion of the clinical population in use today, with ultra-high field systems beginning to infiltrate the clinical setting[13,14]. These continual gains in SNR have been noteworthy in MRI, where long exam times remain one of the major drawbacks to the modality. This is due to the interplay between SNR and scan time, where pulse sequence parameters may be altered to exchange one for the other[15].

One major drawback to higher field MRI systems is their purchase price. The cost of exceptional superconducting magnets, high-performance power electronics, and other specialty hardware required to build a clinical MRI scanner is approximately proportional to the magnitude $B_0$. The often-quoted estimated purchase price of a clinical MRI scanner is US\$1 million per T [13], indicating that a 3 T scanner costs approximately US\$3 million. In addition to purchase cost factors, healthcare institutions must consider many siting requirements, as these are large, heavy, sensitive, and cryogenically cooled machines. The US Department of Veterans Affairs lays out considerations for siting a new MRI system at its medical centers, with factors such as the structural design and vibrational isolation of the MR suite often resulting in additional costs for higher field MRI systems[16,17]. The 1.5 T MRI scanner has traditionally offered a good trade-off between performance and price. This is evidenced in the sales data, with 1.5 T systems still representing two out of every three MRI scanners sold today[13].

### 1.2.3 MRI Protocols and Pulse Sequences

MRI protocols are specific collections of pulse sequences and imaging instructions used to produce a series of clinically useful images to provide direction for a patient's care. Choosing an appropriate imaging protocol is at the radiologist's discretion as they will ultimately be responsible for interpreting and reporting the findings[18]. As expected from an imaging modality with limitless pulse sequence variations, numerous protocols have been developed to address the imaging needs of diverse clinical indications and the preferences of attending radiologists[19,20]. Despite the large number of available protocols, the most used, or routine, protocols often account for a disproportionally large proportion of prescribed exams. This is evidenced in research by Brown & Marotta, who presented a summary of all prescribed brain MRI exams over 18 months at St. Michael's Hospital in Toronto, Ontario. They found that of the 41 available protocols for imaging the brain, two variants of their routine *fast brain* protocol accounted for nearly 38% of all prescribed brain exams[21].

Several types and variations of pulse sequences are often selected as part of a protocol based on the clinical value they provide to radiologists. The imaging parameters of these pulse sequences must be carefully chosen as they not only affect the utility of the images but changing one parameter often negatively influences another[22–24]. The process of selecting and tuning pulse sequences for a particular task is often referred to as clinical protocolling. The primary imaging parameter trade-offs during the clinical protocolling process involve balancing SNR, scan time, scan coverage, resolution, image contrast (i.e., the contrast between tissues with different magnetic properties), and resistance to various

artifacts[15]. System-specific factors[*] affecting these parameters must also be considered when protocolling. Some situations require imaging parameters to be heavily prioritized over others to produce diagnostically useful images[25]. For example, when protocolling a pulse sequence for abdominal imaging during a single breath-hold, a high value may be placed on short scan time[15,26]. However, many pulse sequences are protocolled for general diagnostic utility, providing a good mixture of SNR, resolution, and contrast within an appropriate field of view while minimizing scan time and providing reasonable artifact resistance[25].

## 1.3 Modernization of Low-Field Magnetic Resonance Imaging

### 1.3.1 Advances in Conventional Clinical Field MRI

Over the last three decades, there have been considerable advances in 1.5 T and 3 T MRI technology that are now being translated and exploited on low-field systems. These improvements often allow for increases in SNR and/or decreases in overall scan times. Hardware modernization and pulse sequence technique developments are the two primary categories where progress has been made, with advances in one category often resulting in subsequent improvements in the other[12].

Two notable improvements to MRI hardware include the introduction of high-performance gradients and the implementation of phased RF receive arrays. Modernized gradients have greater thermal efficiency than their predecessors, allowing them to reaching higher peak amplitudes in shorter periods of time (i.e., higher slew rate) with greater linearity[27]. This translates to the ability to perform the many fast imaging pulse sequences that require strong and fast gradient switching. These fast imaging pulse

---

*For example, $B_0$ affects available SNR, contrast, and the prevalence and severity of artifacts.

sequences with inherently high SNR and SNR efficiency (i.e., SNR per unit time) were developed for clinical application in the 1990s [15,27,28]. Although some fast imaging methods were conceived long before their clinical introduction, the hardware was not developed sufficiently to become reality until much later[15,29].

In the seminal work by Roemer et al[30] in 1990, phased RF receive array principles initially developed for radar applications were adapted to MRI. This resulted in drastic SNR increases. The initially tested 4-channel phased array[*] was found to more than double the SNR when compared to a single RF coil in a spinal imaging study[30].

In the case of high-performance gradients, hardware limitations were overcome to allow previously suggested pulse sequences to be developed for use on clinical MRI. The opposite is true for phased RF receive arrays. In 1997, Sodickson and Manning exploited the observation that MR data collected using phased RF receivers contained more information than previously thought. Mainly, each RF coil measured an MR signal, but that signal was heavily influenced by its spatial location. These researchers proposed a method to coherently under-sample the MR signal, thus reducing acquisition times while exploiting RF coil spatial sensitivity information to estimate the uncollected data. The resulting method, now part of a family of parallel imaging (PI) techniques, reduced scan times by a factor of two while only reducing SNR by a factor of $\sqrt{2}$[†] [31,32]. More recently, advanced image reconstruction techniques, such as compressed sensing and machine learning-based methods, are becoming available to clinicians. These techniques also

---

*Four partially overlapped and tuned RF receive coils, each recording an MR signal. The signals are combined using a sum of squares method during image reconstruction.
†Any integer ratio of undersampling is possible with Sodickson & Manning's method. The SNR is proportionally reduced by at least the square root of the undersampling integer.

exploit the concept of information overlap between MR signals recorded on multi-channel RF receivers. Scan times are decreased further through under-sampling while regaining the lost SNR through their reconstruction and post-processing methods[27].

The above innovations are not an exhaustive list of the MRI developments over the past three decades. Many other important advances, including the modernization of pulse sequences, improved system architectures, and a myriad of sensor and computational performance increases, have been implemented to extract more performance[27,33,34]. The key takeaway is that many of the technological developments are translational to low-field MRI and are generally cost-efficient ways of increasing SNR and/or decreasing scan time[13,17].

## 1.3.2  Motivation for Modernizing Low-Field MRI

Despite the myriad of clinical advantages associated with MRI use, challenges such as high overhead and operational cost, extensive siting requirements, and limited patient access in many parts of the world remain today. Modern low-field MRI looks to improve on these issues by providing diagnostically useful images in specific clinical situations at a fraction of the cost of 1.5 T and 3 T systems. Furthermore, modernized low-field systems may also provide improved patient safety and imaging advantages relative to the 1.5 T and 3 T systems in several clinical niches[17].

Potential safety improvements with low-field MRI over higher field systems primarily surround the decreases in force and torque on magnetic objects and their reduced specific absorption rate (SAR)[17,33]. The forces and torques exerted on a magnetic material (often metallic) are positively related to the strength of the MRI. This reduces the risks of patient harm due to magnetically induced force and torque on an implanted

medical device. The reduction in $B_0$ also reduces the size of the fringe field, which is the portion of the magnetic field that extends outside the MRI scanner. The risk of projectiles, which may occur if a strongly magnetic object is mistakenly brought into the MR environment, is also reduced by the decreased field strength and diminished fringe field[17,35]. A more localized fringe field may also have implications for iMRI[17].

SAR is a measure of RF power deposition that results from using RF excitation pulses. Deposited RF power is dissipated within the patient in the form of sensible heat, increasing the temperature of the patient. The US FDA, among other health and medical device regulators, place strict limits on SAR to ensure patient safety and avoid burns[36]. In practice, injuries associated with MRI are rare. However, a 10-year review found the most frequently reported adverse event to the FDA was a thermal event, such as excessive heating leading to a burn[37]. The benefit of low-field MRI is that for a given pulse sequence, SAR is proportional to the square of the main magnetic field strength[36]. For a 0.5 T scanner, this indicates a 9-fold reduction in SAR compared to a 1.5 T scanner.

Although more performance than safety-related, certain pulse sequences have high SAR values within the safe operating range which result in greater patient heating that can lead to reduced patient compliance and motion artifacts[38]. Lower acoustic noise associated with lower fields may also be beneficial for patient compliance, particularly for young and pediatric patients[17].

One fundamental clinical niche where low-field MRI may have an imaging advantage over 1.5 T and 3 T MRI is examining areas with large magnetic susceptibility-induced field distortions. Examples of these regions include the internal auditory canal, the paranasal sinuses, or near a metallic medical device[33]. The potential advantage of

low-field MRI lies in the field-dependent relationship between susceptibility-induced distortions and $B_0$, where a decrease in $B_0$ results in decreased susceptibility-induced field distortions. Historically, this potential imaging advantage could not be exploited clinically by moving to lower fields than 1.5 T due to the unacceptable SNR penalty of imaging on era low-field systems[13].

Based on the discussion above, imaging near metal-containing medical devices is a clear niche where low-field MRI may be the field strength of choice.

## 1.4    Metal in the MRI Environment

### 1.4.1    Safety Considerations for Medical Devices

Given the tremendous strength of the magnetic fields generated by MRI scanners, strict regulations and local protocols reduce the potential safety risks associated with an unsafe item or material entering the MRI environment. For the purposes of this work, we will restrict our discussion to medical devices and adopt the definitions provided by the US FDA[39].

Typically, for a medical device to enter the MRI environment, whether implanted within the patient or accompanying the patient, it must be tested and labeled. Three safety labels that may be assigned to a device: MR unsafe, MR conditional, and MR safe. At no time should an MR unsafe device enter the MRI environment, as it poses a known and unacceptable safety risk. Conversely, MR safe devices are typically nonmagnetic and pose no known safety risks in their interactions with MRI systems. MR conditional devices bridge the gap between entirely restricted and unrestricted medical devices. They often contain metallic components that are weakly magnetic. Interactions between an MR conditional device's magnetic components and the MRI scanner do not pose an

unacceptable safety risk to the patient when used under prescribed conditions[39,40].

Typical conditions include the magnetic field strength at which the device can be used,

maximum SAR limitations, and scan duration limits[39].

Within the MR conditional category, a delineation can be made between active

and passive medical devices. Active devices rely on an energy source for function, such

as electrical power from a battery, but do not include devices powered by the body or

gravity. Passive devices are, therefore, devices which do not require external power to

function. Frequently encountered active devices include pacemakers and

neurostimulation devices[35]. In comparison, common passive medical devices include

vascular devices such as stents, flow diverters, and embolization coils, surgical staples,

orthodontic brackets, bands, and archwires, and many elective and trauma orthopedic

devices[41].

Device testing and labeling is relevant for imaging patients with modernized low-

field systems. As the renaissance of low-field MRI has just begun, most medical devices

have only been tested and labeled for use in 1.5 T and 3 T systems. Fortunately, passive

devices labeled for use at 1.5/3 T will almost always be safe on lower-field MRIs.

Industry experts[35] are now developing guidance on approaching this problem at the

institutional level and providing recommendations on setting up local written policies and

protocols to address off-label uses systematically. Active devices are not as predictable as

passive devices and will continue to require complete formal testing and labeling before

use on low-field scanners[35].

### 1.4.2 Metal-Induced Artifacts

Imaging near MR conditional devices remains challenging despite the low associated

risks. The subtle interactions between the metallic components of the device and the various magnetic fields of the MRI scanner result in images distorted by metal artifacts. The three primary contributors to signal abnormalities near metallic devices are signal void in the device's location, magnetic susceptibility-induced artifacts, and RF shielding. Signal void in the device's location is naturally due to a lack of hydrogen nuclei in metal and is not considered problematic. Conversely, susceptibility-induced artifacts, and to a much lesser extent RF shielding, frequently affect the diagnostic quality of the images depending on the medical device and exam[4,5,26,42,43].

Metal artifacts can be mitigated by carefully selecting pulse sequence parameters or by using specialized sequences and techniques. These specialized techniques and sequences may be implemented on most modern clinical scanners but are frequently accompanied by an increase in scan time or decrease in resolution and are typically focused on orthopedic imaging[44–46].

$B_0$ is a factor specific to the design of a given MRI system that also contributes to the extent of metal artifact. The metallic materials in MR conditional medical devices are often magnetized to a greater extent than the body in an applied magnetic field. This results in susceptibility-induced field distortions in areas where the magnetic susceptibility of materials varies spatially. These field distortions affect how signal is excited and spatially encoded in MRI. In the ranges of materials used in MR conditional devices and MRI scanner field strengths, the magnetization of devices and tissues scale approximately linearly with $B_0$. Thus, at a lower magnetic field, the associated susceptibility-induced field distortions are reduced[47].

## 1.5    Research Motivation, Hypothesis and Thesis Objectives

### 1.5.1 Research Motivation

Modernized low-field MRI systems are just beginning to enter the clinical setting, incorporating many technological advances over their predecessors[13,48]. Consequently, these updated systems have not been studied extensively, nor have they had their role fully defined in the clinical setting. The performance of modern low-field MRI for imaging these regions, particularly compared to the 1.5 T and 3 T clinical systems, remains relatively unknown. Figure 1.1 provides a visual example of modern clinical 3 T and 0.5 T MRIs.
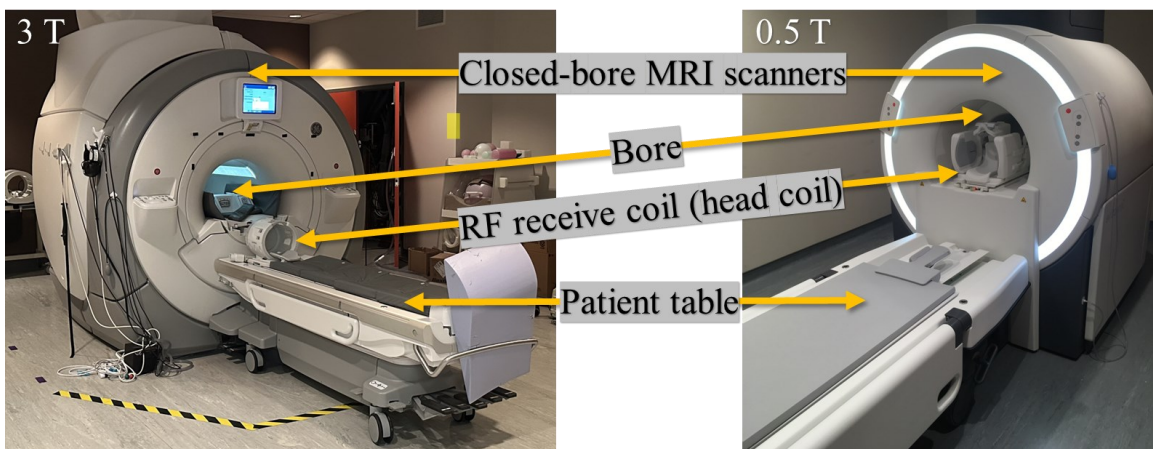


Figure 1.1 Photographs of modern 3 T (left) and 0.5 T (right) MRI scanners. Both systems are traditional closed-bore designs and are configured with multichannel RF receive coils used for imaging regions of the head and brain. The difference in size is readily apparent, with the patient tables being approximately the same size. These systems are located in the Biomedical Translation Imaging Center (BIOTIC) at the Queen Elizabeth II Health Sciences Centre (Halifax, Nova Scotia, Canada).

A logical place to begin benchmarking these machines is in areas where an advantage may be predicted based on *a priori* information. One such area is imaging in regions with large susceptibility variations, specifically near passive MR conditional medical devices. Passive devices were chosen as they have fewer testing and labeling requirements than active devices and may soon be systematically approved for off-label use at low field.

This *in vitro* (phantom-based) metal artifact study seeks to improve the understanding of modern low-field MRI performance with respect to the current practice. Routine brain imaging protocols developed for general diagnostic utility at our institution have been selected. The pulse sequence types are consistent across MRIs, but their parameters are not as they have been independently protocolled to provide diagnostically useful images on each scanner. These protocols represent the first set of pulse sequences a patient requiring brain imaging could be expected to receive. They have been developed for diagnostic utility and not specifically optimized for imaging near metal.

### 1.5.2 Hypothesis and Thesis Objectives

This study aims to contribute to a larger body of research being used to determine optimal clinical use cases for low-field MRI. The primary study objective will be to compare key artifact characteristics across field strengths for multiple passive MR conditional medical devices. Within this, our focus is to understand the field dependent variation in artifact width, a standardized measure of susceptibility-induced artifacts. The term "artifact width" is defined in ASTM International (ASTM) F2119-07 as the greatest straight-line distance measured from the periphery of the tested device to the furthest point where the artifact can be detected. Based on a decrease in magnetic susceptibility-induced field distortions at lower main magnetic field strength, we may formulate the following primary hypothesis:

**Images of passive medical devices produced by pulse sequences optimized for diagnostic utility within routine brain imaging protocols on three modern MRIs will have reduced susceptibility artifact width, as defined by ASTM F2119-07, at 0.5 T compared to 1.5 T or 3 T.**

Furthermore, this research set the following secondary objectives to support primary hypothesis testing and provide additional clinical context:

- Develop an ASTM-F2119-07-compliant imaging phantom for device testing.

- Create a framework for characterizing metal artifacts produced in MRI. A consistent and repeatable framework is required to test the expected volume of data. The framework includes a pipeline for rapidly measuring artifact width, a model of susceptibility distortion to contextualize the results, and an RF shielding assessment component.

- Review bulk artifact characteristics associated with device orientation relative to $B_0$. Device orientations are known to affect artifacts to varying degrees and it is not known how this applies to the tested devices.

- Discuss how trade-offs and decisions made during clinical protocoling may affect the observed artifact widths and characteristics. This is accomplished with the use of a matched (non-protocoled) pulse sequence that excludes the effects of clinical protocolling.

These objectives have all been accomplished, and their full descriptions are provided in the subsequent chapters.

# Chapter 2: Theory, Background, and Characterization Techniques

This chapter provides an overview of the classical mechanics description of MRI, introducing basic imaging mechanisms, exploring the effects of susceptibility-induced field distortions, and reviewing common methods to reduce their effects. Various susceptibility-induced artifact and RF shielding characterization techniques are also introduced and discussed.

## 2.1    MRI and Magnetic Susceptibility

Derivations provided in this section are based on those initially produced by Schenck[47]. Furthermore, a comprehensive mathematical and physical description of MRI is provided by Brown et al[23].

### 2.1.1    Imaging in Homogenous Fields

The human body contains an abundance of hydrogen nuclei (i.e., protons) within water, fat, and other macromolecules, from which the signal in clinical MRI is derived. Protons have a physical characteristic called spin angular momentum, often shortened to "spin". In the classic mechanical description, spin can be modeled as a circulating electric current, resulting in the creation of a magnetic moment. In the absence of external forces, the magnetic moment of hydrogen nuclei is randomly oriented in space. Applying a magnetic field (B), to a group of hydrogen nuclei aligns their magnetic moments with the magnetic field, with a slight majority aligning in the direction of the field and a minority in the opposite direction. We make the simplifying assumption here that B only has a z-component in MRI, where the z-direction is along the magnet's bore. The slight excess of aligned spins results in a net magnetization vector (M) pointing along B. The applied magnetic field also exerts a torque on each magnetic moment, causing them to precess

about B at a predictable frequency. This is called the resonant or Larmor frequency ($\omega$) and is calculated with the Larmor equation ($\omega = \gamma \cdot B$) where $\gamma$ is the gyromagnetic ratio (42.58 MHz/T for a hydrogen nucleus) and B is the magnetic field at a point of interest.

To produce a measurable signal, M is tipped out of alignment with B and into the transverse, or x-y, plane using a time-varying magnetic field (i.e., the RF excitation pulse) at the resonant frequency. The flip angle is the degree to which M is tipped away from B and into the x-y plane. M is now described by its longitudinal (i.e., z-component), $M_z$, and its transverse component, $M_{xy}$. Spins in the transverse plane will continue to precess around B, resulting in a changing magnetic field that can be measured by the RF receive coils. This process is dynamic, with spins returning to their equilibrium state through two independent relaxation processes. The first is called longitudinal relaxation, representing the recovery of $M_z$ to its equilibrium value, $M_0$. The second process is transverse relaxation which represents the loss of $M_{xy}$ due to a loss in the net phase coherence of spins in the transverse plane. Longitudinal and transverse relaxation processes can be characterized by exponential regrowth and decay curves with T1 and T2 representing their time constants, respectively. T1 and T2 for a given collection of spins will be affected by the local environment of those spins; for example, hydrogen nuclei bound to carbon in fat molecules will have different T1 and T2 values than hydrogen nuclei bound to oxygen in water. The varying compositions of tissues and local properties in the body allow MRI to leverage pulse sequences sensitized to different T1 and T2 values to produce tissue-specific image contrast.

The data acquisition process involves recording the signals emitted by excited spins as they undergo relaxation processes. A typical two-dimensional (2D) acquisition

will selectively excite a slice of signal before spatial encoding. Spatial information is encoded into the phase and frequency of excited spins using magnetic field gradients that predictably alter resonant frequencies based on location. Spatially encoded signals are acquired by RF receive coils and digitized as Fourier components that correspond to specific locations in the spatial-frequency domain (i.e., k-space). The location of each Fourier component in k-space is determined by the product of gradient amplitude and duration, such that gradients are used to traverse k-space. Cartesian acquisition methods that fill k-space line-by-line through linear combinations of applied gradients are the most common. Once k-space has been filled, an inverse Fourier transform is used to create an image.

Susceptibility-induced field distortions affect the ability to spatially encode signals. This process can be understood by following a simplified 2D acquisition with a homogenous field followed by a perturbed field. There are three gradient coils in MRI, each capable of altering the z-component of the B in one cardinal direction. In the absence of any field perturbations the z-component of the B at any position can be described by the following equation:

$$B = B_0 + G_x(t) \cdot x + G_y(t) \cdot y + G_z(t) \cdot z \qquad [1]$$

Where $G_x$, $G_y$, and $G_z$ are the magnitude of each gradient at time $t$, and $x$, $y$, and $z$ are the coordinates where B is being calculated. A stepwise process using linear gradients allows signal to be encoded in all dimensions. The first dimension is encoded through selective excitation of a 2D slice of specified thickness (i.e., slice thickness). A slice-select gradient is applied in the slice-select direction, which is chosen to be the z-direction. This reduces Equation [1] to:

$$B = B_0 + G_z(t) \cdot z \qquad\qquad [2]$$

Multiplying by the gyromagnetic ratio converts the predicted magnetic field at a position

to its associated precessional frequency:

$$\omega = \omega_0 + \gamma \cdot G_z \cdot z \qquad\qquad [3]$$

The slice select gradient, $G_z$, is applied in concert with a limited bandwidth (BW) RF

excitation pulse to excite a uniform slice of tissue. Figure 2.1 provides an example of

slice selection; here an RF pulse with 1 kHz BW centered at 8.5 kHz will excite a slice

that is 5 mm thick, centered at 42.5 mm. Arbitrary units have been used for convenience.
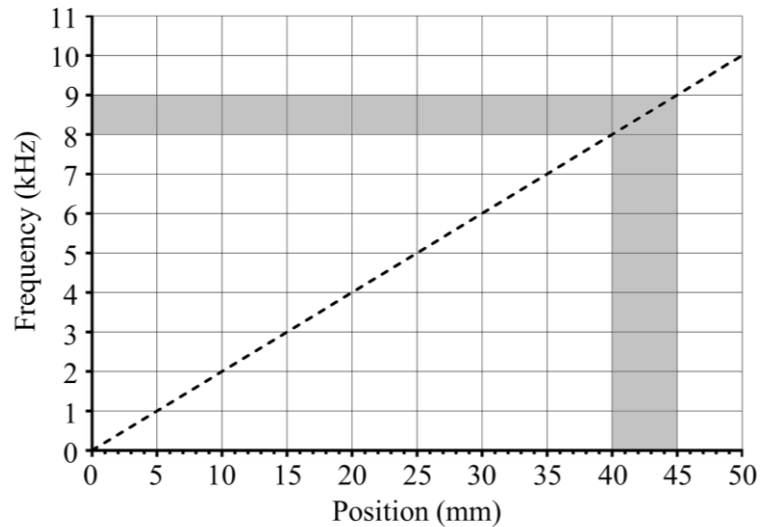


Figure 2.1 Diagram of 2D slice selection in a homogenous field. The grey path represents
the connection between RF pulse frequency and excited location.

A phase encoding (PE) gradient, $G_y$, is applied to temporarily change the resonant

frequency of excited spins to encode phase. Then, a frequency encoding (FE) gradient,

$G_x$, is applied while the signal is acquired and digitized to fill one line of k-space.

Equation [1] indicates the phase accumulated in PE by a spin and the frequency changes

in FE will be functions of position. The process is repeated until all lines of k-space have

been filled. It should be noted the acquisition matrix refers to the number of times the

signal is digitized during FE and the number of PE steps. Additionally, three-dimensional

19

(3D) acquisitions are now common, where a large slab is excited with two PE directions and one FE direction employed to spatially encode the signal.

## 2.1.2 Magnetic Susceptibility

Magnetic susceptibility ($\chi$) is a dimensionless material property that exists on a spectrum, with materials lying near the center being relevant to MRI. Materials that repel applied magnetic field lines are diamagnetic and have negative susceptibility values. In contrast, those that weakly attract magnetic field lines are paramagnetic and have positive magnetic susceptibility values. Within the range of main magnetic field strengths and materials that may safely be used in the MRI environment, the induced magnetization in a material is approximately proportional to $\chi \cdot B_0$. For reference, air has a susceptibility of 0.36 parts per million (ppm), while soft tissue is -9.05 ppm, and non-magnetic stainless steels, which frequently cause deleterious susceptibility artifacts in MRI, are on the order of 3520 – 6700 ppm[47].

When an applied field magnetizes a material, the induced magnetization will contribute to and perturb the overall magnetic field. The material's geometry and orientation relative to the applied field impact how the overall magnetic field is altered. For the purposes of this work, $\Delta B(x, y, z)$ is the perturbing magnetic field produced by device magnetization that distorts $B_0$ as a function of position. Figure 2.2 provides an example of how various shapes and sizes will alter the applied field[47].

a)  $B_0$  A —— A  z x

b)

Static Magnetic Field  $\chi B_0$  $\frac{2}{3}\chi B_0$  $\frac{1}{2}\chi B_0$  x
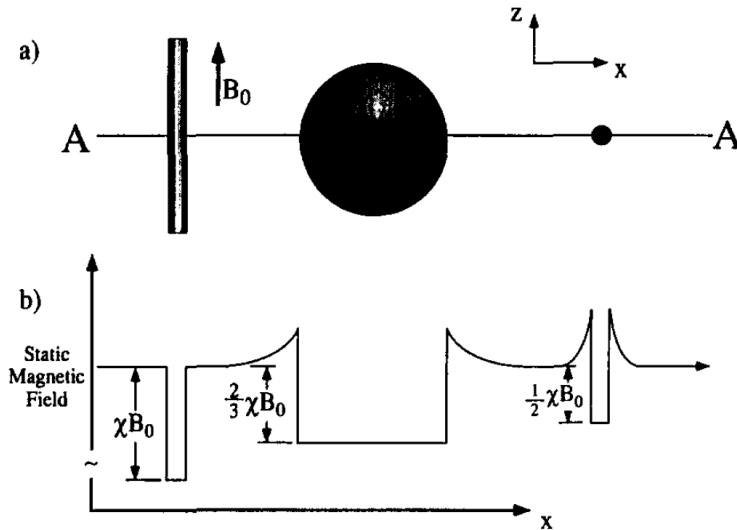
Figure 2.2 "Effect of sample shape, orientation and susceptibility on the static magnetic field"[47] reproduced from John Wiley and Sons under license number 5673760031340. © 1996 Am. Assoc. Phys. Med.

Examining Figure 2.2, subfigure (**a**) displays three shapes and their orientations to $B_0$, while subfigure (**b**) is a plot of magnetic field along the line A-A that provides insight into how those shapes, orientations, and magnetic susceptibilities affect the overall static magnetic field. The long cylinder oriented parallel to $B_0$ on the left side of subfigure (**a**) does not distort the static magnetic field. This is seen in subfigure (**b**) as the static magnetic field on either side of the device is homogeneous (i.e., constant with no slope) right up to the device boundary. Alternatively, when the same cylinder is oriented perpendicular to the magnetic field, depicted on the right side of subfigure (**a**), a considerable perturbing field is created that distorts the static magnetic field. The perturbing fields produced by the perpendicular cylinder are added to the background static magnetic field, resulting in the parabolic-shaped field distortions seen on either side of the cylinders location in subfigure (**b**).

## 2.1.3   Imaging in the Presence of Magnetic Susceptibility Distortions

In areas with large magnetic susceptibility distortions, the spatial encoding processes that

rely on frequency begin to break down. We can modify Equation [1] to account for the

perturbing field produced by the inclusion of a metal device in an otherwise homogenous

region:

$$B = B_0 + G_x(t) \cdot x + G_y(t) \cdot y + G_z(t) \cdot z + \Delta B(x, y, z) \qquad [4]$$

The magnetic field, and therefore the precessional frequency, will now vary from

expectations based on the perturbing field produced by the device. This would not be

problematic if not for the complexity, and often time dependence, associated with the

perturbing field. When spatial frequencies vary unexpectedly the excited slice is warped.

Figure 2.3 provides an example of the 2D slice selection process when the magnetic field

is distorted.
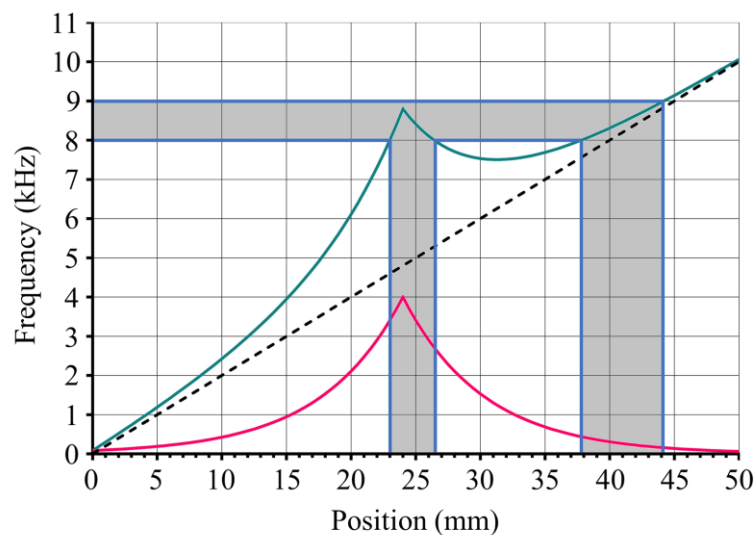


Figure 2.3 Diagram of 2D slice selection with a distorted field. The pink line represents
the perturbing field, while the green line represents the distorted field during slice
selection. The grey bands represent where a limited BW will excite signal. Arbitrary units
are provided for convenience.

Examining Figure 2.3, the same slice selective excitation is applied here as in

Figure 2.1; however, signal is now being excited in multiple locations in addition to the

last 1mm of the slice no longer being excited. On an MR image, this through-plane

distortion appears on images as pile-up artifacts where signal from multiple locations is mapped to one location, resulting in hyperintensities, and signal voids, where the signal has been displaced or was not excited. The effects can be reduced with thinner slices or narrow BW excitation pulses that reduce the amount of signal excited outside the desired slice, reducing signal pile-up artifacts at the a cost of reduced SNR, due to the reduction in the number of excited spins[43]. For 3D acquisitions, slab selective excitations may also be accompanied by additional through-plane distortions[26].

The distorted slice will then be subject to FE, where additional frequency errors will occur in the FE direction, which is the x-direction here. During frequency encoding, we can reduce Equation [4] to:

$$B = B_0 + G_x \cdot x + \Delta B(x, y, z) \tag{5}$$

If we consider the x' to represent the position in the image generated from acquired data during readout, we may rewrite Equation [5] as a function of encoded positions and FE gradient amplitude:

$$B - B_0 = G_x \cdot x + \Delta B(x, y, z) = G_x \cdot x'(x, y, z) \tag{6}$$

Where the positional error in x is defined as:

$$\Delta x = x - x'(x, y, z) \tag{7}$$

This allows us to rearrange [6] as:

$$x'(x, y, z) = x + \frac{\Delta B(x, y, z)}{G_x} \tag{8}$$

Examining Equation [8], we see that as the FE gradient amplitude increases, x'(x, y, z) approaches x, thus reducing positional errors. We can also consider the relationship between gradient amplitude, BW, and field of view (FOV):

$$G_x = \frac{BW}{\gamma \cdot FOV} \qquad [9]$$

Substituting this relationship into Equation [8] and removing the gyromagnetic ratio we are left with the following proportionality:

$$x'(x, y, z) \propto \frac{FOV}{BW} \qquad [10]$$

Here we see that increasing BW for a given FOV, or decreasing FOV for a given BW will reduce frequency encoding errors, but these are associated with a loss in SNR, or reduced scan area. This is a valuable relationship for our work, as the gradient amplitude values are not directly available from the clinical sequences, while FOV and BW are provided. In-plane distortions arise from the described FE errors and have a similar visual appearance to through-plane distortions.

A distinction is now made between the two categories of pulse sequences from which all clinical pulse sequences are based: spin echo (SE) and gradient echo (GRE). These sequences differ in how they manipulate the signal during acquisition. A basic GRE sequence applies a single RF excitation pulse before acquiring the signal. Alternatively, a basic SE sequence applies a 90° pulse followed by a 180° pulse prior to acquisition. This has a rephasing effect on spins, resulting in different contrast on SE relative to GRE images.

Concerning imaging near metal, GRE sequences often suffer from large areas of signal loss, as the increased range of precessional frequencies accelerates the loss of spin coherence. Alternatively, the refocusing pulses inherent to SE imaging eliminate the effects of signal loss from accelerated spin dephasing. This reduces signal voids on images but can increase signal pile-up as additional signal is available to be displaced

during FE. Despite this, substituting a SE for GRE sequence is frequently recommended if the contrast will be appropriate for the task. However, if GRE sequences are needed, increasing the in-plane resolution, or decreasing echo time (TE – the time between the RF excitation pulse and the middle of FE) can help alleviate dephasing signal loss[23].

Several methods specifically developed for imaging near metal have been developed but are associated with even greater trade-offs. One earlier method for imaging near metal is view angle titling (VAT-SE), which applies a small slice select gradient during readout to reduce in-plane distortion at the cost of a blurred and tilted view[26]. More advanced imaging techniques, such as slice encoding for metal artifact correction (SEMAC), apply multiple slice encoding steps to effectively measure the slice distortion, allowing correction during image reconstruction. Despite their high performance, these techniques are associated with drastic increases in scan time[49].

Figure 2.4 provides representative anatomical images of susceptibility-induced artifact on a knee containing orthopedic hardware. The characteristic signal pile-up and signal void is visible on the SE and VAT-SE images both in-plane and through-plane. The difference between a standard SE and the SEMAC technique shows an impressive reduction in artifact at the cost of scan time.
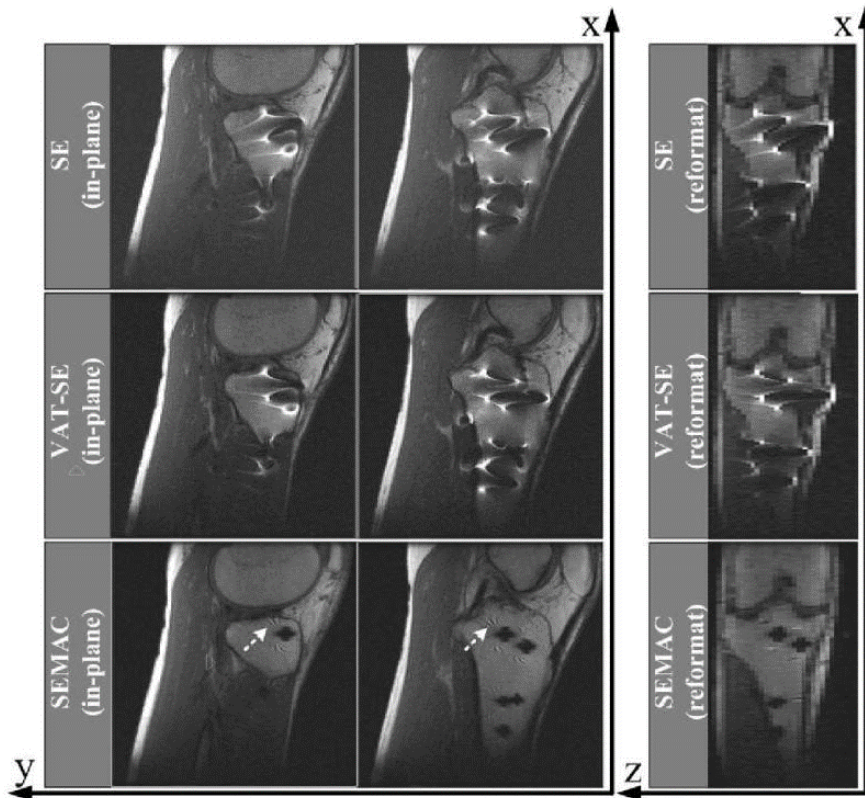
Figure 2.4 "Comparison of in vivo results of the subject with a metallic fixation device in his spine"[49] reproduced from John Wiley and Sons under license number 5673221150242. © 2009 Wiley-Liss, Inc.

## 2.2 Susceptibility Artifact Characterization Methods

In nearly all situations, susceptibility artifact is the primary contributor to metal artifact. Studies of susceptibility artifacts caused by metallic medical devices can generally be categorized as either *in vivo* or *in vitro*. However, it is not uncommon for published works to include both types. *In vivo* studies primarily involve scanning small cohorts of patients or research animals who have some type of MR-conditional device. In contrast, phantom studies use imaging phantoms to replicate important MRI-related properties of living tissues in a more controlled environment. Due to the complex anatomies surrounding medical devices *in vivo*, artifacts are assessed by trained radiologists or researchers with intimate knowledge of the subject matter. These studies are commonly

used for the validation of new artifact reduction pulse sequences only after extensive *in vitro* validation work has been completed. As such, *in vivo*-specific research will not be further considered in this work. For reference purposes, well-known examples of *in vivo* susceptibility artifact studies include the works of Olsen et al[44] , Lu et al[49], and Koch et al[50].

The general methodology across phantom studies examining susceptibility is very consistent. An appropriate phantom is developed and imaged using relevant pulse sequences on the MRI scanner of interest. Artifact on the resulting images is characterized using either quantitative or qualitative methods. The primary variations between studies include phantom design, medical device selection, pulse sequence selection, artifact definition, and artifact characterization and assessment methodology. Various studies are reviewed below with a focus on quantitative characterization methods to aid in developing an appropriate artifact characterization framework.

### 2.2.1 Grid-Based Methods

Several researchers have used grided phantoms to measure the geometric distortion produced by metallic devices to characterize susceptibility artifacts. The metallic device is placed atop a uniform grid within a phantom so the artifact can be assessed by performing measurements of grid distortion as a proxy for geometric distortion. Wichmann et al[51] used this method to evaluate the characteristics of aneurysm clips made from different materials, while Venook et al[52] used a similar version to assess orthopedic medical devices. One drawback to these works is that grid distortion measurements are typically performed manually, which introduces a degree of subjectivity, particularly in less experienced researchers. More important is the lack of scalability for studies which

use larger numbers of pulse sequences and devices to be tested. Figure 2.5 provides an

example of susceptibility artifact on an MR image collected using the grided phantom

method in the research done by Venook et al[52].
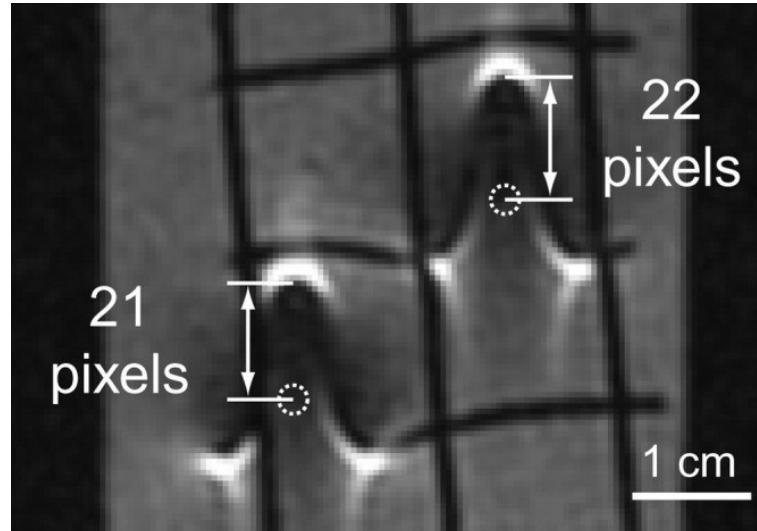


Figure 2.5 "Artifact measurement example, coronal image of an agarose gel phantom
with grid and titanium alloy screws at 1.5T"[52] reproduced from John Wiley and Sons
under license number 5673221008469. © 2006 Wiley-Liss, Inc.


## 2.2.2   ASTM F2119-Based Signal Thresholding Methods

ASTM released a standardized test method in 2001 to systematize the process of

characterizing susceptibility artifact[53]. The standard, listed under F2119, has quickly

become a point of reference for many researchers. The most current version of the

standard (F2119-07) indicates the medical device to be characterized should be

suspended in a phantom filled with a homogenous fluid. This fluid is prepared to have

MR relaxivity characteristics representative of the tissues where the medical device

would be found *in vivo*. In the image domain, artifactual voxels are defined as any voxel

with a signal intensity outside ± 30% of the mean background signal intensity and

thresholded to create a binary artifact map. ASTM requires that artifact be measured as

the longest linear distance measured between the edge of the device and the artifact

fringe (i.e., the location boundary where artifactual signal returns to background)[54]. This

poses a significant issue when the artifact is so substantial that the device void and

artifactual signal void are intertwined. In these cases, measurements of the device with

calipers may be subtracted from the artifact measurements[54].

In a field dependent study, Olsrud et al[55] measured the artifact produced by

various aneurysm clips and shunt valves. This study examined the field dependence of

artifact using 1.5 T and 3 T MRI scanners, applying many of the recommendations

provided by ASTM. The authors modified the artifact characterization method, instead

choosing to measure the maximum artifact in both in-plane directions. The dimensions of

the tested devices were measured before scanning and were aligned in the phantom,

allowing researchers to simply subtract the respective devices dimension from the total

disturbed area to produce a potentially more reliable method of artifact assessment. Other

researchers, such as Shellock et al[56,57], extended the assessment of artifact in some

situations to be the maximum in-plane artifact area. In-plane artifact area may provide a

more representative measurement of artifact, particularly for large solid devices.

Imai et al[58] conducted further research on the field dependence of susceptibility

artifacts at 1.5 T and 3 T. The effect of background signal selection on measured artifact

size was evaluated when using the threshold method. Nearly any region outside the

disturbed area produced a reliable assessment of artifact. These researchers also

improved upon the assessment of artifacts by generating a three-dimensional model of

artifactual regions, from which the volume of the device can be subtracted. Their work

also confirmed the previously observed reduction in artifact size associated with either

aligning the long axis of the device with the main magnetic field or setting the frequency encoding direction along the device's longest axis in the plane of interest. The volume artifact method accounts for both in-plane and through-plane artifacts. However, this may be difficult to implement with very small devices or for comparison between pulse sequences with different slice thicknesses and/or spacings.

### 2.2.3   Simulation-Based Methods

A final susceptibility artifact characterization method is to simulate the artifact. Spronk et al[59] recently developed a method that uses JEMRIS, a pulse sequence development tool, along with phantom models and calculated susceptibility maps, to predict susceptibility artifact area. The model was validated with passive metal rods against experimental data collected at 1.5 T, 3 T, and 7 T. Simulated artifact was found to have a similarity as high as 84% to measured data. Despite the promising results, it has not yet been validated at low fields or with more complex clinical protocols.

### 2.3   RF Shielding Artifacts

### 2.3.1   RF Shielding in MRI

RF shielding artifacts only affect metallic devices containing conducting loops that enclose or partially enclose a region of interest, such as a stent. The frequency-selective RF excitation pulse generates an eddy current within devices containing these conducting loops. Lenz's law dictates that the induced eddy current will oppose the magnetic field that created it, which in this case is the RF excitation pulse. The visual effect of RF shielding is primarily a reduction of image signal intensity in the lumen of the device with larger signal variations possible near the device[3,60]. The combination of RF shielding and susceptibility artifacts produced by vascular stents can inhibit the ability of magnetic

resonance angiography (MRA) to evaluate lumen accurately. Figure 2.6 provides

anatomic and phantom images of RF shielding in stents when imaged with MRA. The

arteries (both anatomical and simulated) show bright signal. Examining subfigure (**a**)

stents can be seen bilaterally in the carotid arteries approximately two-thirds of the way

up the image. Subfigure (**b**) provides an image of a stent in a high-quality vascular

phantom exhibiting the characteristic in-stent signal loss.
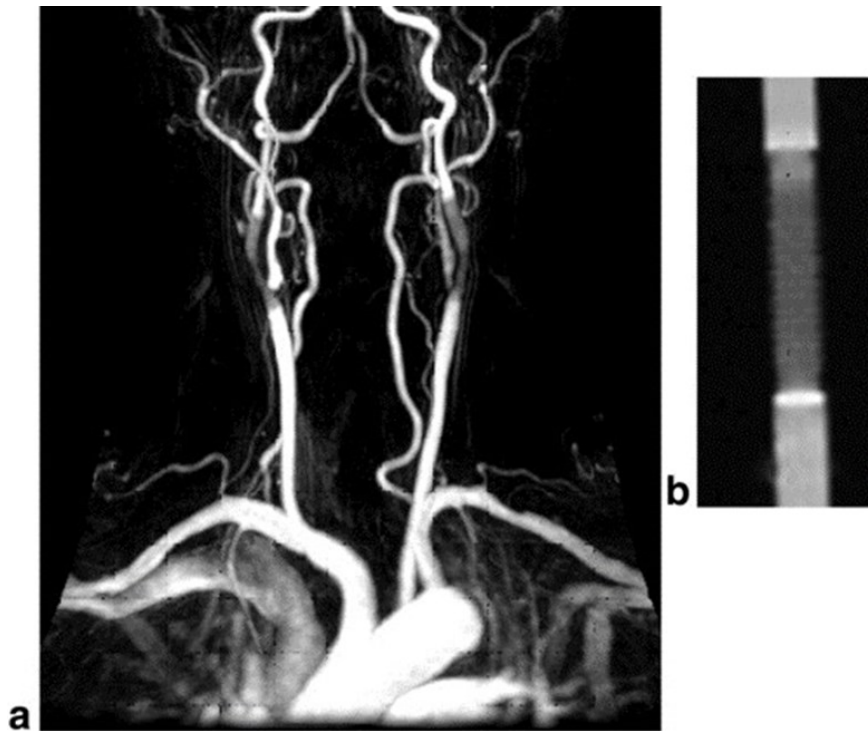


Figure 2.6 "SMART stents (a) in the left and right carotid arteries and (b) in a phantom"[3] reproduced from John Wiley and Sons under license number 5673760233944. © 2003 Wiley-Liss, Inc. MRA images of stents *in vivo* (**a**) and *in vitro* (**b**) using a vascular phantom.

## 2.3.2   RF Shielding Characterization Methods

Several variations of RF characterization have been developed to improve stent lumen

visibility through reduced RF shielding effects in MRA. Bartels et al[61] proposed a model

to alleviate shielding effects by selecting optimal RF pulse flip angles, and therefore RF

transmit power. Their model could be used to determine a flip angle that would provide

the most SNR from stent lumen. The SNR was measured by manually selecting regions

of interest (ROI) within the stent lumen as compared to background noise, like how SNR

is calculated. This model accounted for susceptibility artifacts as well as flow related

artifacts. The flow artifacts appeared as a shifting of the in-stent artifacts downstream,

exhibiting "rocket artifact". This can be seen in subfigure (**b**) of Figure 2.6. However,

this model required the use of a complex vascular phantom[61].

Due to the intertwined nature of susceptibility artifact and RF shielding in stents,

Wang et al[61] produced a separate model to measure their relative contributions artifact.

This phantom-based research determined that RF shielding was the primary contributor

to artifact within the lumen of stents of low magnetic susceptibility. In these stents,

susceptibility factors accounted for less than 1% of signal variance from background.

They also showed the decrease in signal caused by RF shielding occurred not only near

the stent wall, but also in the center of the lumen, well away from the susceptibility

artifact boundary[3]. Stent susceptibility and RF shielding factors are shown in Figure 2.7.
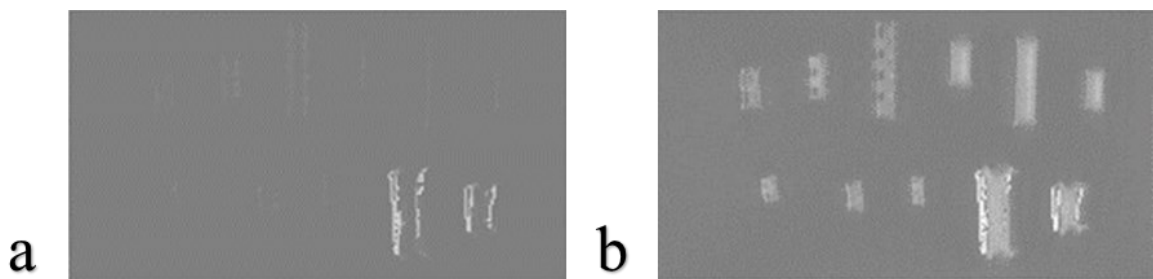


Figure 2.7 "Stents with their axes perpendicular to $B_0$"[3] reproduced from John Wiley and Sons under license number 5673760233944. © 2003 Wiley-Liss, Inc. (**a**) depicts the susceptibility factors and (**b**) depicts the RF shielding factors. Stents on the top row of both subfigures are stents composed of nitinol. Brighter shades of gray indicate a larger factor.

The effects of magnetic susceptibility and RF shielding were further examined by

Kato et al[62] focusing on improving stent lumen visibility in time-of-flight magnetic

resonance angiography (TOF-MRA) pulse sequences. They employed another ROI-based method to compare the lumen signal to background signal proximal to the stent. Flip angle was the driving factor in stent lumen visibility, as echoed by Choi et al[60].

# Chapter 3: Methodology

This chapter thoroughly examines the methodology used to conduct this *in vitro* phantom study based on test standard ASTM F2119-07. It covers the MRI systems, materials, and devices used to acquire data, provides an overview of the routine brain imaging protocol, develops the artifact characterization framework, and discusses statistical hypothesis testing.

## 3.1    Data Acquisition

### 3.1.1    MRI Scanners

Modern MRI systems routinely used for clinical exams at our institution were selected for this study. The following three clinical MRI scanners available for research use at Queen Elizabeth II Health Sciences Centre (Halifax, Nova Scotia, Canada) were selected:

- 0.5 T – Synaptive Medical Evry (Toronto, Ontario, Canada):

    - Low-field head-only scanner

    - Maximum gradient amplitude: 100 millitesla per meter (mT/m)

    - Maximum gradient slew rate: 400 Tesla per meter per second (T/m/s)

    - 16-channel RF receive coil

- 1.5 T – GE HealthCare Signa HDxt (Waukesha, Wisconsin, USA):

    - Mid-field full body scanner

    - Maximum gradient amplitude: 33 mT/m

    - Maximum gradient slew rate: 120 T/m/s

    - 8-channel RF receive coil

- 3 T – GE HealthCare Discovery MR750 (Waukesha, Wisconsin, USA):

    - High-field full body scanner

- o Maximum gradient amplitude: 50 mT/m

- o Maximum gradient slew rate: 200 T/m/s

- o 32-channel RF receive coil

These scanners were operated in first level controlled operating mode with the assumption of a 91-kilogram (200-pound) patient. SAR values for all tested MRIs and pulse sequences complied with the MR-conditional requirements of the tested passive device.

### 3.1.2 Passive Medical Devices

As the 0.5 T MRI is a head-only scanner, medical devices routinely encountered in or on the head were considered for this study. The following three passive medical devices were selected:

- 3M Precise TM Vista Disposable Skin Stapler (Product number 3995-35W): One skin staple ("staple") obtained from this stapler is used. The staple is composed of 316L stainless steel and measures approximately 7.2 millimeters (mm) wide by 4.3 mm tall by 0.55 mm thick. This medical device is listed as untested. However, 316L stainless steel is generally considered safe for use in the MR environment. These staples are routinely scanned in patients immediately after surgery at our institution, and similar staples produced by other manufacturers are listed as MR-conditional[41]. Magnetic susceptibility values for stainless steels range between 3520 – 6700 ppm depending on the composition and allotrope[47].

- Balt Extrusions Silk+ Intracerebral Self-Expandable Stent (Product number SILK3,5X35): This braided self-expanding flow-diverting stent ("stent") is composed of fine nitinol (nickel-titanium alloy) wires and is frequently used in

combination with endovascular coils for the treatment of cerebral aneurysm. The stent is a straight hollow cylinder with a measured unconstrained diameter of 3.9 mm and a length of 22.5 mm. The device is listed as MR-conditional[63]. The susceptibility of nitinol is approximately 245 ppm[47].

- MicroVention Terumo Hypersoft Finishing Coil, Helical (Product number 8510-0408): Endovascular embolization coil ("endovascular coil") composed of a tight winding of platinum wire. This device is 8 centimeters (cm) long and 0.25 mm in diameter. The device is listed as MR-conditional[64]. The susceptibility of platinum is approximately 279 ppm[47].

Photographs of each tested device are provided in Figure 3.1.
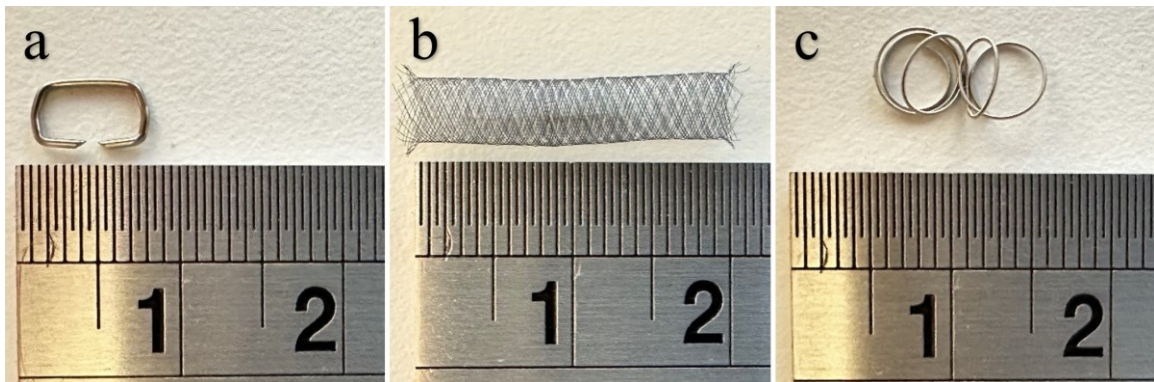


Figure 3.1 Photographs of tested medical devices. Major scale units are centimeters. Legend: (**a**) staple, (**b**) stent, and (**c**) endovascular coil.

These devices were selected due to their ubiquitous use at our institution and their ability to represent various geometries and materials frequently used in other medical devices. For example, the 316L stainless steel wire used to form the tested staple is the same material and has a similar diameter to the wire commonly used to manufacture orthodontic archwires[65].

### 3.1.3 Device Orientation

ASTM F2119-07 specifies testing passive medical devices in three mutually orthogonal orientations to $B_0$ and swapping the PE and FE directions in each orientation. While this level of testing is necessary for regulatory approval, it is deemed to be outside the scope of this work. Our interest lies in the field-dependence of artifacts, not ascertaining the absolute maximum artifact size for medical device labeling. Hence, the staple and stent will be imaged in two orientations: with their longest axis parallel to $B_0$ and perpendicular to $B_0$. These orientations are commonly reported to encompass the range of artifacts produced by a device and are considered adequate for our analysis. Figure 3.2 depicts the two tested orientations for the staple and stent. Conventional anatomic direction markers of left-right (LR), anterior-posterior (AP), and superior-inferior (SI) are provided.
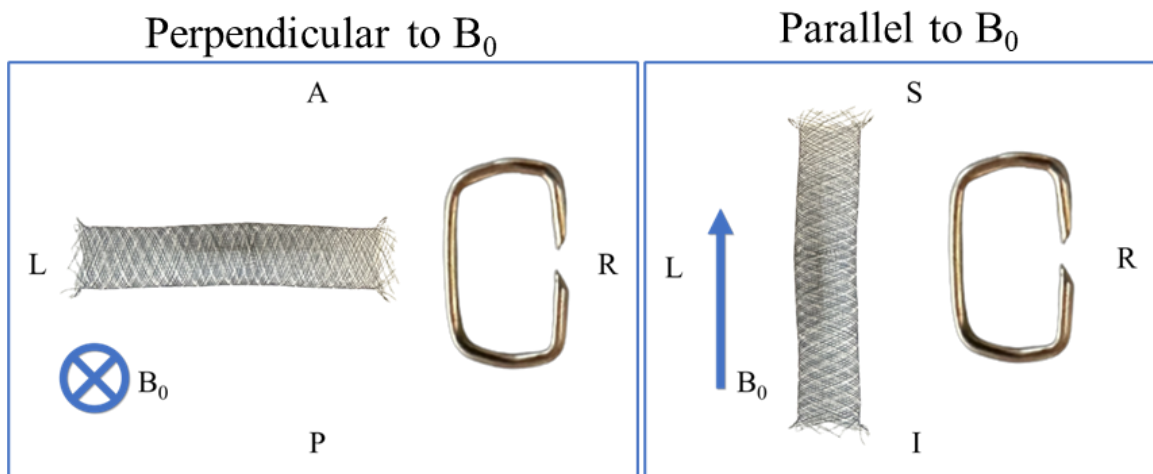


Figure 3.2 Diagram of the stent and staple orientations relative to $B_0$. Directional markers are included on each subfigure's top, bottom, and sides. Subfigure *Perpendicular to $B_0$* on the left is shown in the axial plane, with $B_0$ pointing directly into the plane and across the smallest axis of the devices. Subfigure *Parallel to $B_0$* on the right is shown in the coronal plane, with $B_0$ pointing vertically and along the longest axis of the devices.

Only one orientation will be collected for the endovascular coil due to limitations

associated with accurately representing *in vivo* geometry and with the artifact

measurement pipelines ability to measure the device as tested. Figure 3.3 provides a

diagram of the tested orientation of the endovascular coil.
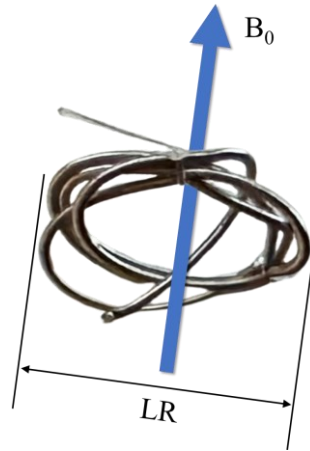


Figure 3.3 Diagram of endovascular coil orientation relative to $B_0$. This perspective view is in an oblique plane. The endovascular coil is secured in a circular shape using a thin nylon string. In the axial plane, the projection of the endovascular coil is nearly circular. However, considerable variation is observed across the SI direction. In clinical use the endovascular coils are constrained by the outer walls of the aneurysm. The lack of suitable constraining material resulted in the 2D approximation tested here. The variation along the SI direction in the 2D approximation also limits the ability of the artifact width measurement pipeline to produce accurate measurements.

### 3.1.4 Imaging Phantom

The imaging phantom developed for use in this research fully complies with ASTM

F2119-07 requirements. A two-part 12 cm diameter acrylic spherical container houses the

test solution and medical device. When subjected to applied magnetic fields, the uniform

internal magnetization of spherical objects[47] ensures the production of a homogeneous

signal within the test solution. A gelatine solution (2.5% gelatine by weight) immerses

the medical device within the phantom and provides mechanical support during scanning.

The gelatine solution is doped with manganese chloride tetrahydrate to a final

concentration of 0.1 millimolar to produce representative relaxation times of tissues found in the head[55,66–68].

Each phantom contains a single medical device secured near the center with a thin nylon string. The nylon string is anchored to a 3D-printed polyethylene terephthalate glycol (PETG) ring sitting just inside the equatorial perimeter of the spherical container. This ring ensures the device remains in an area of homogenous signal at least 4 cm from the side of the container. The similar magnetic susceptibility[69] of PETG plastic and water allows the ring to be used as a reference scale to ensure image-based measurements are accurate. The PETG ring has a height of 5.0 mm, and a radial thickness of 5.3 mm. Detailed phantom construction methods are provided in Appendix A. Representative photographs of the phantom are provided in Figure 3.4.
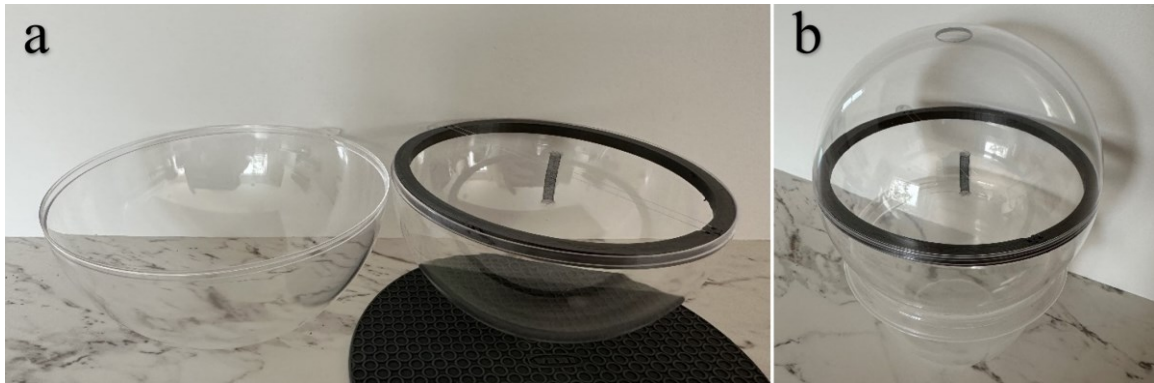


Figure 3.4 Photographs of phantom containing the stent. As shown, the phantom has yet to be sealed in the center. (**a**) depicts the phantom before joining the two halves of the spherical container, while (**b**) depicts the assembled phantom prior to sealing and adding doped gelatine through the top fill hole. The stent can be seen supported by a thin nylon string attached to a gray PETG ring in both images.

## 3.2 Routine Brain Imaging Protocol

### 3.2.1 Selected Pulse Sequences

Pulse sequences from the routine brain imaging protocols currently used at the Queen Elizabeth II Health Sciences Centre (Halifax, Nova Scotia, Canada) were selected for this

work. They represent the standard of care, non-contrast enhanced sequences in clinical use as of November 2023. This exam represents the first set of scans a patient might receive during a follow-up examination. They are clinically protocolled for diagnostic utility and have not been optimized for imaging near metal devices. Our testing protocol consists of the following institutional routine brain imaging protocol pulse sequences:

1. Balanced steady-state free precession imaging (bSSFP)

2. Diffusion-weighted imaging (DWI)

3. T1-weighted fluid-attenuated inversion recovery imaging (T1 FLAIR)

4. T2-weighted imaging (T2WI)

5. T2-weighted fluid-attenuated inversion recovery imaging (T2 FLAIR)

6. Time-of-flight magnetic resonance angiography (TOF-MRA)

A TR-matched bSSFP (TRM bSSFP) is also included in the test protocol. Further discussion of TRM bSSFP is provided in 3.3.2.

The routine brain imaging protocol typically also includes susceptibility-weighted imaging. This sequence enhances physiological magnetic susceptibility differences to aid the detection of pathologies often associated with trauma and stroke[70]. However, it has been excluded here to prevent the misinterpretation of intentional contrast enhancements as metal artifacts.

The protocol choices here represent a significant deviation from ASTM F2119-07, which requires the collection of two image sets in each orientation with swapped PE and FE directions using simple SE and GRE sequences. As discussed in Section 3.1.3, this will not be considered here as it conflicts with our objective.

### 3.2.2 bSSFP

bSSFP is a fast GRE pulse sequence with apparent T2/T1-weighted contrast resulting from its balanced and steady-state acquisition. This SNR efficient sequence is frequently used for high-resolution imaging of the internal auditory canal and cranial nerves[7,71]. GE HealthCare refers to its bSSFP sequence as FIESTA (fast imaging employing steady-state acquisition). However, the vendor-neutral sequence name of bSSFP will be used for consistency in this work. A summary of bSSFP pulse sequence parameters is provided in Table 3.1.

Table 3.1 bSSFP pulse sequence parameters.

| $B_0$ | 0.5 T | 1.5 T | 3 T |
|---|---|---|---|
| Flip angle (degrees) | 60 | 60 | 60 |
| TR (ms) | 7.0 | 5.8 | 5.7 |
| BW (Hz) | ± 70,000 | ± 62,500 | ± 62,500 |
| FOV (cm) | 18 | 18 | 18 |
| BW/FOV (Hz/cm) | 7,778 | 6,944 | 6,944 |
| FE direction | AP | AP | AP |
| Acquisition matrix (FE x PE) | 300 x 300 | 300 x 300 | 300 x 300 |
| Acquired voxel thickness (mm) | 0.6 | 0.6 | 0.6 |
| Number of slice-direction PEs | 164 | 68 | 68 |
| Scan time (minutes:seconds) | 4:36 | 5:12 | 3:56 |

In bSSFP, steady-state magnetization in the transverse plane is quickly achieved and maintained throughout the acquisition. RF pulses, typically alternating polarity, are applied successively over short repetition times (TR) of 5 – 10 ms, with PE and FE encoding occurring within each TR. The complete rewinding, or balancing, of gradients (i.e., the gradient area between subsequent TRs is 0) to recover transverse magnetization after each FE step and before the next RF pulse is what differentiates bSSFP from other

fast GRE sequences. Although the high SNR efficiency associated with maintaining a coherent transverse magnetization is beneficial, the accompanying sensitivity to field homogeneity is not. Any changes to the expected resonant frequency results in phase offsets to the transverse magnetization during TR. When phase offsets of $\pm\,180°$ from expected occur with TR, the refocusing mechanism during FE fails, resulting in complete signal loss. This leads to dark bands in spatial locations with frequency offsets of $\pm\frac{1}{2\cdot TR}$, and multiples thereof[72–74]. Therefore, minimizing TR will increase the frequency offsets required to produce these banding artifacts, thus decreasing the effects of magnetic field inhomogeneities.

The 3 T MRI uses a modified version of bSSFP based on the constructive interference in steady state method[28,75]. The GE HealthCare-specific name for the variant is FIESTA-C, which, for consistency, will be referred to as bSSFP (FIESTA-C) when the distinction is relevant. In bSSFP (FIESTA-C), using various under-sampling techniques, the higher SNR available at 3 T is traded for reduced scan time. This allows collecting two different image sets of the desired anatomy in approximately the same scan time needed to produce one set at low field. The key to bSSFP (FIESTA-C) is the first image is acquired using alternating polarity RF excitation pulses, while the second image is acquired using only positive polarity pulses. This offsets the location of banding artifacts in the images relative to each other, causing the banding artifacts, or stop bands, in one image to correspond with the center of the passband in the other. During image reconstruction, a maximum intensity projection (MIP) extracts the highest signal intensity at each spatial location, which naturally comes from the passbands. The resulting image will primarily consist of passband signal to minimize banding artifacts[75].

### 3.2.3 DWI

Diffusion restriction is a biomarker for many pathologies, including acute ischemic stroke, medulloblastoma, lymphoma, and cholesteatoma. Various methods can be used to implement DWI, but the most common combines a preparation sequence to introduce diffusion weighting followed by a rapid acquisition of the diffusion-weighted signal. Diffusion weighting is achieved using a pulsed gradient spin echo (PGSE), which is like a traditional SE sequence but includes two large identical gradients. The first gradient is applied after the 90° RF pulse and the second follows the 180° RF pulse. Different combinations of x-, y-, and z-gradients allow directional evaluation of diffusion processes. The sensitivity of DWI to field inhomogeneity arises from the echo planar imaging (EPI – a type of GRE sequence that rapidly traverses k-space in a single excitation) acquisition of the diffusion-weighted signal[76], which results in poor performance near metal[77]. The clinically protocolled DWI tested here all utilize the standard PGSE and 2D EPI combination. The combined b1000 images were selected for use in our study. DWI pulse sequence parameters are provided in Table 3.2.

Table 3.2 DWI pulse sequence parameters.

| $B_0$ | 0.5 T | 1.5 T | 3 T |
|---|---|---|---|
| Diffusion directions[a] | 3 | 3 | 4 |
| Effective TE[b] (ms) | 79.2 | 83.4 | 58.4 |
| PI acceleration factor | 2 | 2 | 4 |
| BW (Hz) | ± 192,000 | ± 250,000 | ± 250,000 |
| FOV (cm) | 24 | 22 | 22 |
| BW/FOV (Hz/cm) | 16,000 | 22,727 | 22,727 |
| FE Direction | LR | LR | LR |
| Acquisition matrix (FE x PE) | 120 x 120 | 192 x 160 | 128 x 128 |
| Slice thickness (mm) | 5.5 | 5.0 | 5.0 |
| Number of slices | 28 | 30 | 22 |
| Scan time (minutes:seconds) | 1:40 | 1:20 | 1:20 + 0:22[c] |

[a]Number of directions in which diffusion is evaluated. The 0.5/1.5 T evaluates diffusion in cardinal directions; the 3 T evaluates diffusion in tetrahedral directions.
[b]Effective TE for EPI pulse sequences is the time required to collect the central lines of k-space.
[c]Routine protocol includes a high-order shim calculation before running the DWI sequence.

### 3.2.4 T1 FLAIR

The T1 FLAIR sequence is often used to distinguish between grey matter, white matter, and lesioned tissue in the brain, which have good T1 contrast. The fast SE-based sequences here employ an inversion recovery pulse[*] to null cerebrospinal fluid (CSF) and other relevant fluids before spatial encoding the signal[7,78]. A summary of T1 FLAIR pulse sequence parameters is provided in Table 3.3.

---

[*]Inversion recovery pulses are not expected effect measured artifact widths. Inversion recovery is the recommended method for suppressing fat signal near metal when frequency-based fat saturation methods fail [43].

Table 3.3 T1 FLAIR pulse sequence parameters.

| B$_0$ | 0.5 T | 1.5 T | 3 T |
|---|---|---|---|
| BW (Hz) | ± 32,000 | ± 31,250 | ± 31,250 |
| FOV (cm) | 24 | 24 | 24 |
| BW/FOV (Hz/cm) | 2,667 | 2,604 | 2,604 |
| FE Direction[a] | SI | SI | SI |
| Acquisition matrix (FE x PE) | 300 x 300 | 320x 192 | 320 x 224 |
| Slice thickness (mm) | 5.0 | 5.0 | 5.0 |
| Number of slices | 22 | 21 | 20 |
| Scan time (minutes:seconds) | 4:24 | 2:12 | 1:12 |

[a]The axial acquisition for the endovascular coil is frequency encoded in the AP direction.

### 3.2.5   T2WI

T2WI is a SE-based sequence used extensively throughout the body, offering contrast based on the T2 relaxivity of tissues. A summary of T2WI pulse sequence parameters is provided in Table 3.4.

Table 3.4 T2WI pulse sequence parameters.

| B$_0$ | 0.5 T | 1.5 T | 3 T |
|---|---|---|---|
| BW (Hz) | ± 72,000 | ± 62,500 | ± 50,000 |
| FOV (cm) | 25 | 22 | 22 |
| BW/FOV (Hz/cm) | 5,760 | 5862 | 4,545 |
| Frequency Encode Direction | AP | NA[a] | NA[a] |
| Acquisition matrix (FE, PE) | 272 x 200 | 320[1] | 512[1] |
| Slice thickness (mm) | 5.5 | 5.0 | 5.0 |
| Number of slices | 28 | 30 | 22 |
| Scan time (minutes:seconds) | 4:26 | 3:08 | 2:19 |

[a]The T2WI sequences on the 1.5 and 3 T systems are PROPELLER acquisitions.

A technique called PROPELLER (periodically rotated overlapping parallel lines with enhanced reconstruction) is used by the 1.5 T and 3 T MRIs to reduce motion and pulsation artifacts. PROPELLER samples k-space in a series of radial acquisitions that

are rotated around the center until the FOV is fully sampled. The center of k-space is inherently oversampled, averaging motion effects during image reconstruction at the cost of scan time[79].

### 3.2.6   T2 FLAIR

The T2 FLAIR is extensively utilized in the clinical setting along with the T2WI and includes the addition of an inversion recovery to null CSF, like the T1 FLAIR. The parameters for this fast SE-based sequence are provided in Table 3.5.

Table 3.5 T2 FLAIR pulse sequence parameters.

| $B_0$ | 0.5 T | 1.5 T | 3 T |
|---|---|---|---|
| BW (Hz) | ± 48,000 | ± 25,000 | ± 41,670 |
| FOV (cm) | 25 | 22 | 22 |
| BW/FOV (Hz/cm) | 3,840 | 2,273 | 3,788 |
| FE Direction | AP | AP | RL |
| Acquisition matrix (FE, PE) | 250 x 216 | 256 x 224 | 320 x 192 |
| Slice thickness (mm) | 5.5 | 5.0 | 5.0 |
| Number of slices | 28 | 30 | 22 |
| Scan time (minutes:seconds) | 4:26 | 3:36 | 5:26 |

It is interesting to note the difference in FE direction between 0.5/1.5T and 3 T. This may be due to the increased pulsatile flow and anatomically-derived susceptibility artifacts at higher field strengths[80]. The protocolling decision to use the slower FE direction may be a trade-off where the artifacts are sufficiently shifted from the regions of interest without requiring the slower and higher SAR PROPELLER acquisition.

### 3.2.7   TOF-MRA

TOF-MRA is a GRE-based sequence used to image vasculature without contrast. This

sequence uses saturation pulses[*] to null the signal from a slab of static tissue. Fresh blood

flowing into the imaging area was not exposed to the saturation pulse and will have an

equilibrium longitudinal magnetization. The slab is then imaged using flow-compensated

GRE techniques. The blood produces a strong signal relative to the saturated tissues,

appearing bright on images. A MIP of the images in different orientations allows detailed

views of the vasculature[15]. However, the high resolution and large FOV required by these

sequences result in a low SNR efficiency, providing an advantage for higher field

strengths[81,82]. A summary of TOF-MRA pulse sequence parameters is provided in Table

3.6.

Table 3.6 TOF-MRA pulse sequence parameters.

| $B_0$ | 0.5 T | 1.5 T | 3 T |
|---|---|---|---|
| TE (ms) | 6.0 | 2.6 | 3.1 |
| BW (Hz) | ± 10,000 | ± 31,250 | ± 31,250 |
| FOV (cm) | 16 | 20 | 22 |
| BW/FOV (Hz/cm) | 1,250 | 3,125 | 2,841 |
| FE Direction | AP | AP | AP |
| Acquisition matrix (FE x PE) | 220 x 200 | 320 x 192 | 384 x 256 |
| Acquired voxel thickness (mm) | 1 | 1.4 | 1.0 |
| Number of slice-direction PEs | 80 | 88 | 80 |
| Scan time (minutes:seconds) | 7:38 | 5:56 | 2:30 |

## 3.3   Artifact Characterization Framework

The following framework has been created to characterize metal artifacts in MRI. It

consists of three components: a susceptibility artifact width measurement pipeline, a

TRM-bSSFP field distortion model, and an RF shielding assessment methodology. The

---

*RF pulses that are applied and subsequently spoiled, resulting in an incoherent transverse magnetization.

susceptibility artifact width measurement pipeline is used to measure the artifact width on tested images for primary hypothesis testing. A TRM bSSFP field distortion model is used to evaluate susceptibility-induced field distortions around the staple and provides an example of a matched pulse sequence that does not include the effects of clinical protocolling. Finally, the RF shielding assessment evaluates the relative in-stent signal at each field strength.

### 3.3.1 Susceptibility Artifact Width Measurement Pipeline

Susceptibility artifact is defined here as signal that falls outside of $\pm$ 30% of background signal intensity. Total artifact area or volume measurements represent reasonable methods to assess the extent of susceptibility artifact, particularly with larger solid medical devices. However, we aim for a like-to-like comparison between field strengths related to the established literature and ASTM F2119-07. As such, susceptibility-induced artifact is primarily characterized as artifact width. The artifact width is the maximum measured in-plane distance from the device periphery to the artifact fringe (i.e., location where signal returns to $\pm$ 30% of background), evaluated across all slices in a pulse sequence. Unique morphological features of artifacts are also characterized visually, emphasizing the various hypointensities, hyperintensities, and geometric distortions.

An automated measurement tool has been developed using MATLAB to measure artifact width rapidly. The program allows batch characterization of MRI exam data in DICOM file format. The first step in the characterization process involves automatically selecting a principal ROI containing the medical device surrounded by a homogenous background signal. Figure 3.5 provides a visualization of the ROI placement process.
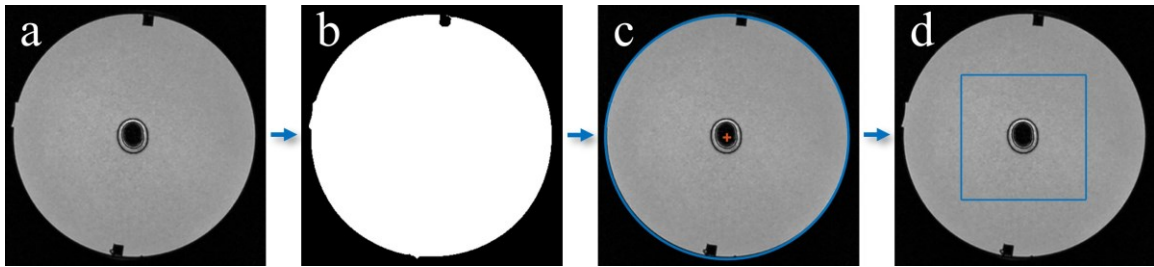
Figure 3.5 Principal ROI selection process. The process begins in (**a**) when the program loads the pixel data of an MRI image. The Sobel edge detection method and other MATLAB Image Processing Toolbox[83] tools are used to separate phantom signals from background noise, as shown in (**b**). A circle is fit to the detected edge to enforce the known circular cross-section of the spherical phantom using a Pratt direct least-squares spherical fitting method[84,85] in (**c**). The circle coordinates are used to place the vertices of the principal ROI inbound of the phantom's perimeter by approximately one-third of the phantom's radius. The principal ROI is the area bound within the four vertices and can be seen as the blue box in (**d**).

Once the principal ROI is selected, four additional background locations are chosen to measure background signal intensity accurately. One background region is placed inside each corner of the principal ROI with dimensions of 20 x 20 voxels. This background region size has been proven adequate in other ASTM F2119-07-based works[58]. The mean background signal intensity obtained by averaging the signal across the background regions is used to threshold the principal ROI to create a binary map. Voxels with signal intensity values outside the ± 30% artifact threshold are considered artifactual and assigned a value of '1', while all other voxels are set to '0'. The artifactual voxels are then measured vertically and horizontally and compared to the known device dimensions. The program outputs the results from each pulse sequence into an Excel spreadsheet to compare to other trials and to reduce the possibility of manual transcription errors. Images of the selected ROI and binary artifact images are also saved as a collection for rapid visual validation of program function. Figure 3.6 provides representative images from this pipeline.
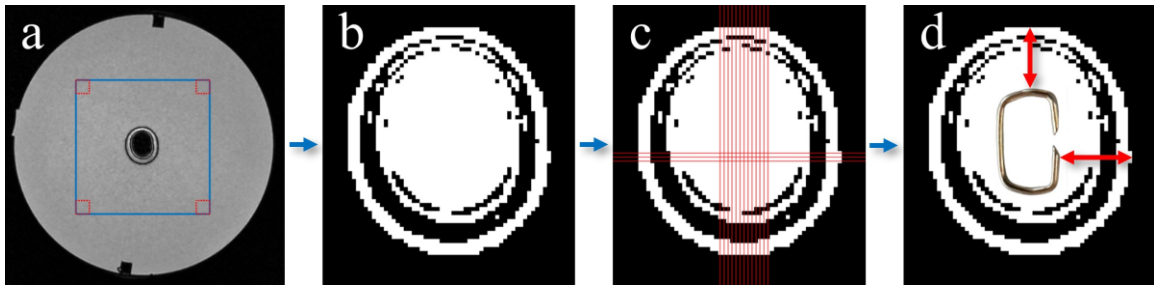
Figure 3.6 Images from the artifact width measurement pipeline. The principal ROI can be seen in (**a**) as the blue bounding box. The four background regions used to measure background signal intensity are included in the inner corners of the principal ROI and can also be seen in (**a**). This background signal thresholds the principal ROI, producing an artifact map shown in (**b**). The red lines in (**c**) represent the locations where the longest discontinuous artifact was measured in the vertical and horizontal directions using matrix operations. The pixel distance measured in (**c**) is converted to a physical distance by multiplication with the pixel spacing values in the DICOM. The appropriate device dimension, measured with a set of calipers prior to encapsulation in the phantom, is subtracted from the artifact measurement calculated in (**c**). This new measurement is divided by two to produce a representative measurement of artifact width as defined by ASTM F2119-07. A visual representation of artifact width is provided in (**d**). This process is repeated for all images within one pulse sequence, with the largest measured artifact width being used to characterize susceptibility artifacts.

### 3.3.2   TRM bSSFP Field Distortion Model

As discussed in Section 3.2.2, bSSFP produces banding artifacts at frequency offset

multiples of $\pm\frac{1}{2\cdot TR}$. Therefore, if the TR values are matched on two different MRIs, the

banding artifacts will represent the same field offsets, regardless of field strength. If we

assume[*] the primary contributor to off-resonance frequencies in the phantom are

susceptibility-induced field distortions caused by medical devices, bSSFP sequences can

---

*In practice, $B_0$ and phantom construction inhomogeneities will contribute to the location of bSSFP bands. These effects are expected to be small compared to the effects of the staple and are approximately equal for each MRI. The use of a numerical simulation would be a valuable future addition to this work to validate this model.

be used to model the associated magnetic field distortions. Additionally, this sequence negates protocolling effects, so any differences between bSSFP and TRM bSSFP artifact widths can be attributed to clinical protocolling decisions.

TRM bSSFP sequences were created on the 1.5 T (TR = 7.1 ms) and 3 T (TR = 7.0 ms), which closely matched the 0.5 T (TR = 7.0 ms) bSSFP. It should be noted that the modified bSSFP sequences were not based on bSSFP (FIESTA-C). The TRM bSSFP sequence is used whenever the routine brain imaging protocols are in this study.

The field distortion model is applied to the staple and evaluates both orientations relative to $B_0$. The distortions are quantified by measuring the center-to-center distance of the outermost bands in each anatomical direction with the open-source image processing package FIJI[86]. The device dimensions are then subtracted from this measurement and divided by two, providing a similar measurement to artifact width. The process is repeated for each trial so descriptive statistics can be provided.

### 3.3.3 RF Shielding Measurement

RF shielding is characterized by comparing the signal intensity near the center of the stent lumen with the background signal intensity. FIJI[86] is used for this ROI-based method. Signal intensities are measured in the center of the stent lumen and an annular background location only on TOF-MRA images. The average signal obtained from the lumen is divided by the average background signal to provide a measure of the relative in-stent signal, following the methodology used by Choi et al[60]. As discussed in Section 2.3.2, the relative in-stent signal measurements will include some susceptibility artifact, as the two effects are intimately related. Figure 3.7 provides a representation of the RF shielding measurement.
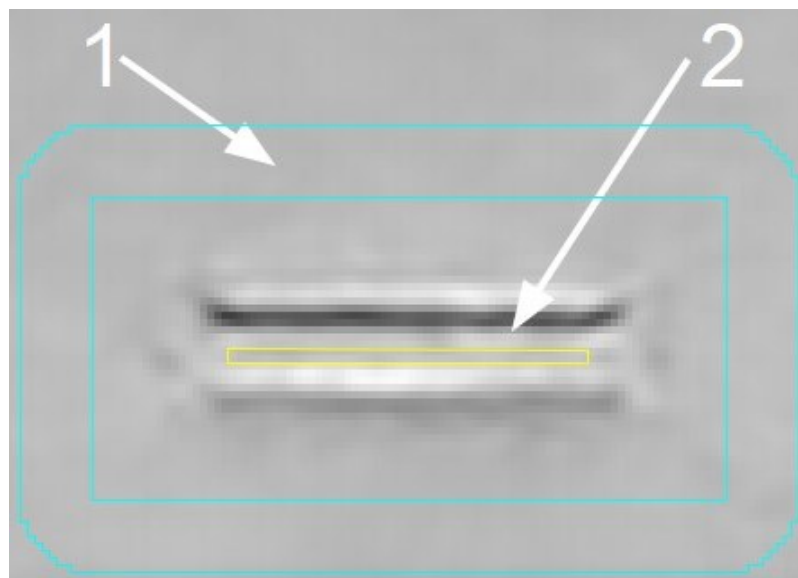
Figure 3.7 Relative in-stent signal measurement. Arrow (**1**) indicates the background signal region bound by the inner and outer cyan lines. Arrow (**2**) indicates the stent lumen assessment area bound by the yellow line. Placing the stent lumen assessment area approximately 1 mm away from the stent wall and just inboard of the ends reduces susceptibility artifact contributions.

## 3.4 Statistical Hypothesis Testing

The ability of MRIs to produce highly repeatable images is crucial, given their clinical use. Daily quality assurance (QA) checks are completed with imaging phantoms to validate the systems. Owusu and Magnotta reviewed the results of daily QA checks, finding approximately half of phantom measurement variability was due to phantom placement and landmarking in the scanner[87]. Despite the slight variability in test-retest with MRI, three image sets of each pulse sequence, orientation, device, and field strength were acquired. This allows statistical hypothesis testing and the calculation of descriptive statistics.

The primary hypothesis is evaluated by comparing artifact width measurements obtained at 0.5 T, 1.5 T, and 3 T. Data is grouped based on device and orientation as follows:

- Staple in the parallel orientation

- Staple in the perpendicular orientation

- Stent in the parallel orientation

- Stent in the perpendicular orientation

- Endovascular coil in the perpendicular orientation

Within each above grouping, a two-factor ordinary analysis of variance (ANOVA) is conducted, where the factors are MRI field strength and pulse sequence, and the dependent variable is artifact width. Multiple comparison testing is limited to evaluating differences in mean artifact width between field strengths for each pulse sequence. The Benjamini and Hochberg (BH) False Discovery Rate (FDR) method is applied with an FDR of 5% (i.e., Q value of 0.05). Therefore, of the comparisons deemed to be statistically significant[*] (i.e., q<Q, where the q value is the FDR-adjusted P value) here, approximately 5% can be assumed to be false positives[88]. The BH FDR method was selected as has increased statistical power relative to other post hoc methods such as Bonferroni correction. The BH FDR method is particularly beneficial in exploratory research, where the cost of missing a finding or research opportunity is large (i.e., high cost to false negatives) relative to the cost of future experiments[89].

    The following secondary analyses are included to provide a more comprehensive overview of metal artifact in modern low-field MRI:

- One-factor ordinary ANOVA with BH FDR (Q value of 0.05) to test the dependence of average artifact width (across all clinically protocoled sequences)

---

[*] The technical term used by Benjamini and Hochberg for a significant result after post hoc correction with the FDR method is "discovery", however, we defer to the more commonly used term of "statistically significant" for readability in this work.

on the factor of MRI field strength/orientation. Separate ANOVA's are conducted for the staple and the stent.

- Two-factor ordinary ANOVA with BH FDR (Q value of 0.05) to test the dependence of RF shielding via measurement of in-stent signal reduction on MRI field strength and stent orientation. Multiple comparisons of in-stent signal reduction values are made between field strength results for each orientation.

- Two-factor ordinary ANOVA with BH FDR (Q value of 0.05) to test the dependence of field distortion distance from the staple on MRI field strength/orientation (e.g., 0.5 T parallel) and direction (e.g., SI). Multiple comparisons of distortion distance measurements are made between directions for each MRI field strength/orientation.

All statistical analyses were conducted in GraphPad Prism version 10.1.1 [90].

# Chapter 4: Results

This chapter summarizes the results obtained with the developed artifact characterization framework. Bar charts are used extensively to visually convey the results of many tests and observed patterns. Each bar represents the average of three measurements, with error bars representing the standard deviation (SD) of those values. The columns are differentiated from one another using a color-blind safe palette; however, they are also consistently listed in order of increasing field strength from left to right within a given grouping. Recall a grouping primarily refers to the data and results for a given device, orientation, and pulse sequence (e.g., bSSFP of staple parallel to $B_0$). Groups are also listed from left to right in a consistent manner within each section to facilitate chart interpretation and inter-chart comparison.

All tested comparisons are included on figures in this chapter and are indicated by a pairwise comparison arrow. An asterisk above a pairwise comparison arrow represents a significant result, while "nd" indicates no discovery (i.e., the compared means do not vary significantly). It should be reiterated that statistical testing was only applied within a particular grouping. Caution must be used to avoid inferring statistical significance, or lack thereof, between adjacent groupings on a common plot or between plots without a pairwise comparison arrow. Additionally, all provided numerical values are accompanied by their respective SD indicated by the plus-minus symbol. Supplementary data summary tables are provided in Appendix B, and statistical testing summary tables are provided in Appendix C.

## 4.1    Susceptibility Artifact Characterization and Width Measurement

Groups are plotted together based on the tested device and orientation, highlighting the

effect of field strength and pulse sequences. Visual descriptions of artifacts are provided

for each device before the susceptibility artifact width measurements are presented.

### 4.1.1 Staple Results

Figure 4.1 provides representative images of artifacts produced by the staple when

imaged with different pulse sequences. Note that the staple is not visible, as the artifact

volume is sufficiently large to obscure the device. All images of ROIs exhibit large areas

of signal hypointensity in the staple's location. Hyperintense regions are found near the

artifact's periphery, close to the artifact fringe. These images provide an example of the

range of artifacts produced by different pulse sequences, which cannot be predicted *a*

*priori*, particularly for more complex variants.
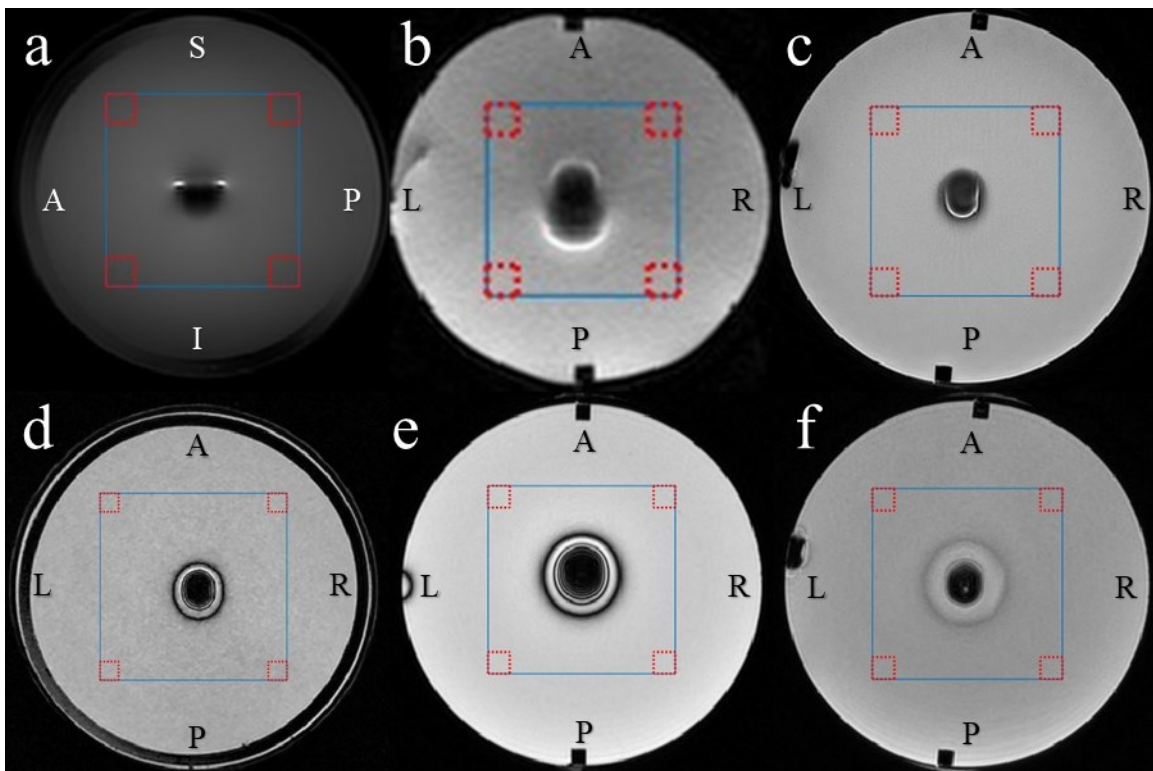


Figure 4.1 Representative images of staple susceptibility artifact. All presented images are of the staple perpendicular to $B_0$ to visually compare artifact patterns between pulse sequences. Images obtained in the parallel orientation exhibit similar artifact levels; however, the artifact morphology varies due to the associated differences in the staple's axial project. Legend: (**a**) T1 FLAIR at 3 T (recall the T1 FLAIR is a sagittal

acquisition), (**b**) DWI at 1.5 T, (**c**) T2WI at 3 T, (**d**) bSSFP at 0.5 T, (**e**) TRM bSSFP at 3 T, and (**f**) bSSFP (FIESTA-C) at 3T.

Although qualitative, the field dependence of banding artifact in bSSFP images is easily seen when examining subfigures in Figure 4.1: (**d**) bSSFP clinically protocolled at 0.5 T (**e**) TRM bSSFP at 3 T with TR matched to that of 0.5 T, and (**f**) bSSFP (FIESTA-C) clinically protocolled at 3 T. By comparing (**d**) to (**e**), the size of the characteristic bSSFP banding artifacts can be seen to change dramatically when moving from 0.5 T to 3 T using matched pulse sequences. Additionally, the effect of clinical protocolling can be seen by comparing (**e**) to (**f**), where (**f**) is the clinically optimized protocol version of (**e**). The quantitative results of the artifact width measurements allow for a more detailed description of the metal artifact. The average parallel and perpendicular artifact width measurements for the staple are plotted in Figure 4.2 and Figure 4.3 , respectively.
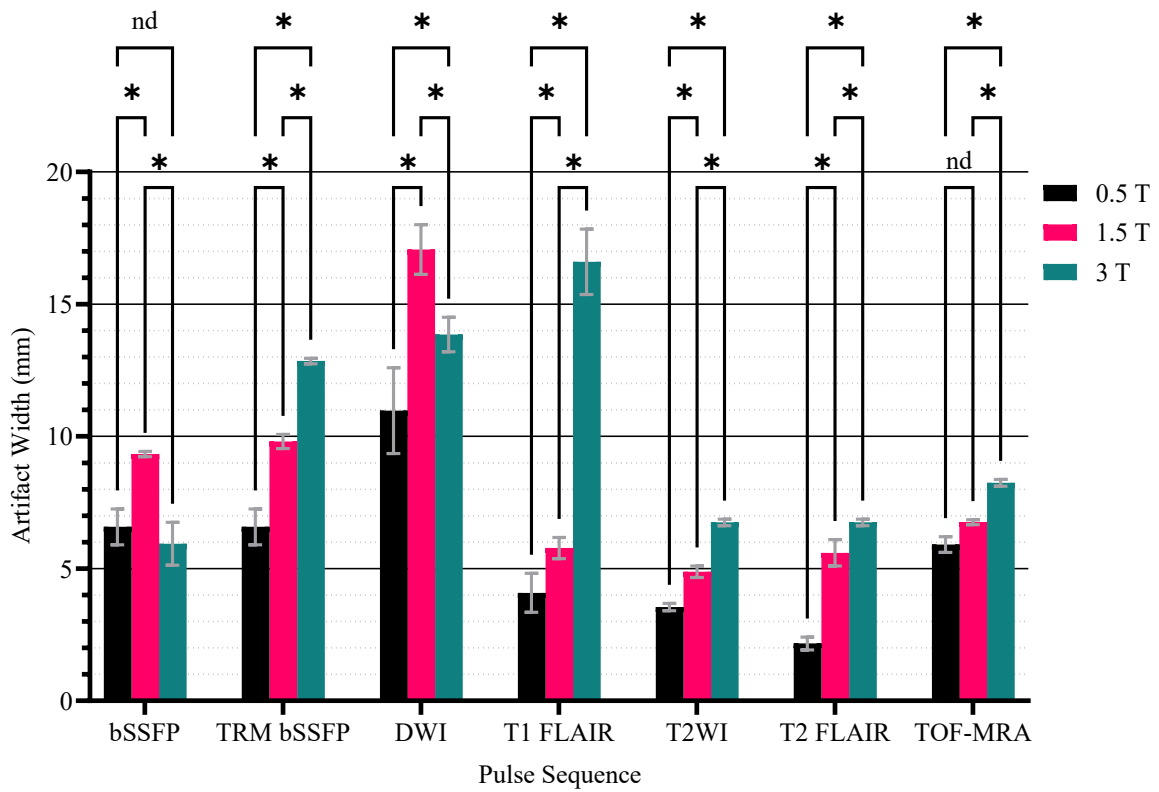
Figure 4.2 Artifact width produced by the staple in parallel orientation.
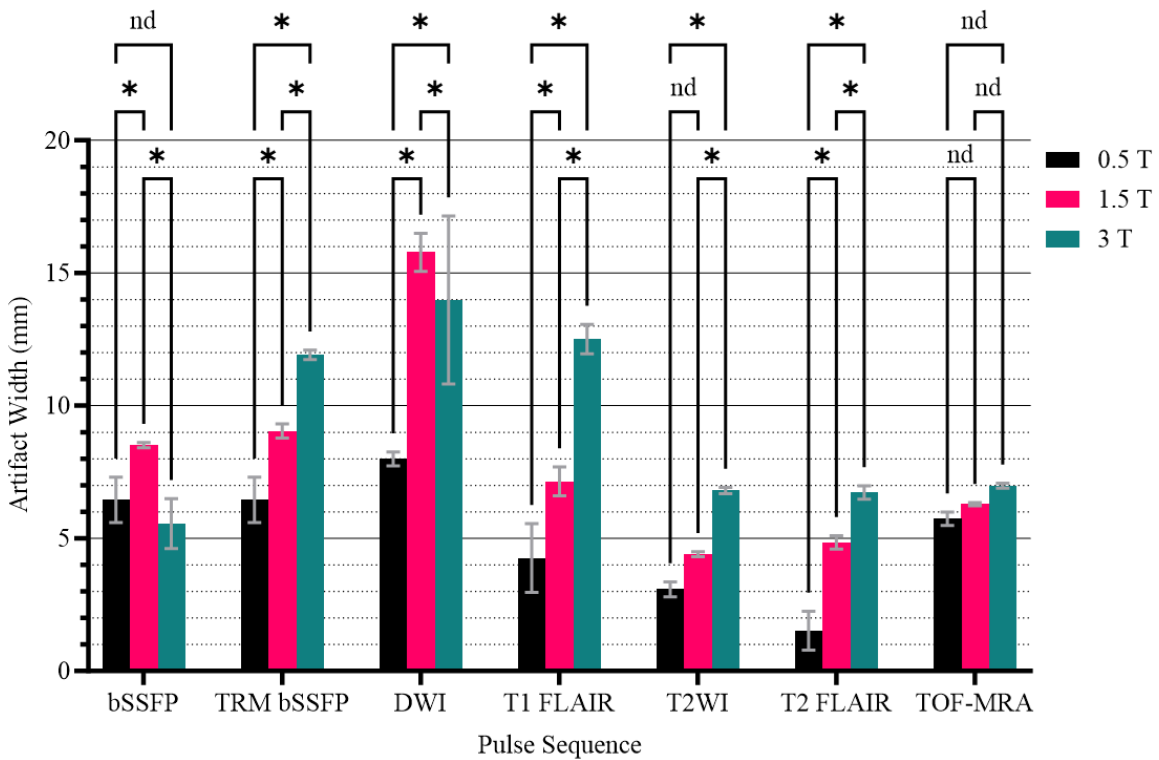


Figure 4.3 Artifact width produced by the staple in perpendicular orientation.

Statistical testing was completed on 14 comparisons between 0.5 T and 1.5 T, 14 comparisons between 0.5 T and 3 T, and 14 comparisons between 1.5 T and 3 T. Of the 28 tested comparisons between 0.5 T and 1.5/3T, 22 tests were deemed significant following FDR correction. All 22 comparisons indicated 0.5 T produced less artifact width than the comparator MRI. The remaining six tests did not reach significance; therefore, no statistical tests indicated that artifact width was increased at 0.5 T relative to 1.5 T or 3 T for the staple. The artifact widths produced by the staple averaged across the clinical pulse sequences and orientations are $5.19 \pm 2.65$ mm, $8.03 \pm 4.09$ mm, and $9.22 \pm 3.85$ mm, corresponding to the 0.5 T, 1.5 T, and 3 T MRIs, respectively. Recall the TRM bSSFP is not a clinical pulse sequence. Despite the observed trend in the bulk average artifact width, the relatively large standard deviations and two-factor ANOVA results ($p<0.001$ for parallel and perpendicular orientations) indicate a significant variation in artifact size as a function of pulse sequence, which is also visually evidenced in Figure 4.2 and Figure 4.3.

Artifact width at 0.5 T was significantly lower than that measured at 1.5 T and 3 T when imaging the staple, regardless of tested orientation when imaged using TRM bSSFP, DWI, T1 FLAIR, and T2 FLAIR. This trend was altered slightly with T2WI, where only one comparison between 0.5 T and 1.5/3 T (0.5 T vs 1.5 T perpendicular) did not reach significance. Notably there were no statistical differences in artifact width using TOF-MRA in the perpendicular orientation ($5.74 \pm 0.25$ mm at 0.5 T, $6.28 \pm 0.06$ mm at 1.5 T, and $6.98 \pm 0.09$ mm at 3 T), while the two significant results in the parallel orientation were 0.5 T < 3 T and 1.5 T < 3 T ($5.91 \pm 0.30$ mm at 0.5 T, $6.76 \pm 0.10$ mm at 1.5 T, and $8.25 \pm 0.12$ mm at 3 T) .

The effects of clinical protocolling are further evaluated by comparing the relative performances of bSSFP and TRM bSSFP. The 0.5 T produced images with significantly reduced artifact width relative to the four tested parameter-matched TRM bSSFP comparisons. Counter to our field dependence expectations, bSSFP at 3 T produced comparable artifact width to 0.5 T in the parallel ($6.41 \pm 0.81$ mm at 3 T vs. $6.68 \pm 0.68$ mm at 0.5 T) and perpendicular ($5.56 \pm 0.94$ mm at 3 T vs. $6.45 \pm 0.85$ mm at 0.5 T) orientation. Additionally, bSSFP on both the 0.5 T and 3 T MRIs produced less artifact width than the 1.5 T ($9.34 \pm 0.10$ mm in the parallel orientation and $8.52 \pm 0.10$ mm in the perpendicular orientation). Additionally, DWI at 3 T had significantly reduced artifact width relative to 1.5 T in parallel ($13.85 \pm 0.65$ mm at 3 T vs. $17.07 \pm 0.94$ mm at 1.5 T) and perpendicular ($13.98 \pm 3.16$ mm at 3 T vs. $15.78 \pm 0.72$ mm at 1.5 T) orientation. These deviations from expectation provide considerable evidence of clinical protocolling effects.

Arranging the above statistical tests by orientation reveals that 19 out of 21 comparisons reached significance in the parallel orientation, which drops slightly to 16 out of 21 tests in the perpendicular orientation. The exact 16 comparisons that exhibited a significant difference in the parallel orientation were also present in the perpendicular orientation. The three additional artifact width comparisons reaching significance in the parallel orientation were one T2WI (0.5 T < 1.5 T) and two TOF MRA (0.5 T < 3 T and 1.5 T < 3 T) pulse sequences. The average artifact width in the parallel orientation across all pulse sequences, excluding TRM bSSFP, was $5.54 \pm 2.99$ mm, $8.24 \pm 4.34$ mm, and $9.69 \pm 4.21$ mm for the 0.5 T, 1.5 T, and 3 T MRIs, respectively. The equivalent results in the perpendicular orientation were $4.84 \pm 2.30$ mm, $7.83 \pm 4.09$ mm, and $8.76 \pm 3.52$

mm, respectively. Artifact width dependence on orientation was not found to be statistically significant for any field strength. The bulk orientation effect results for the staple are presented in Figure 4.4.
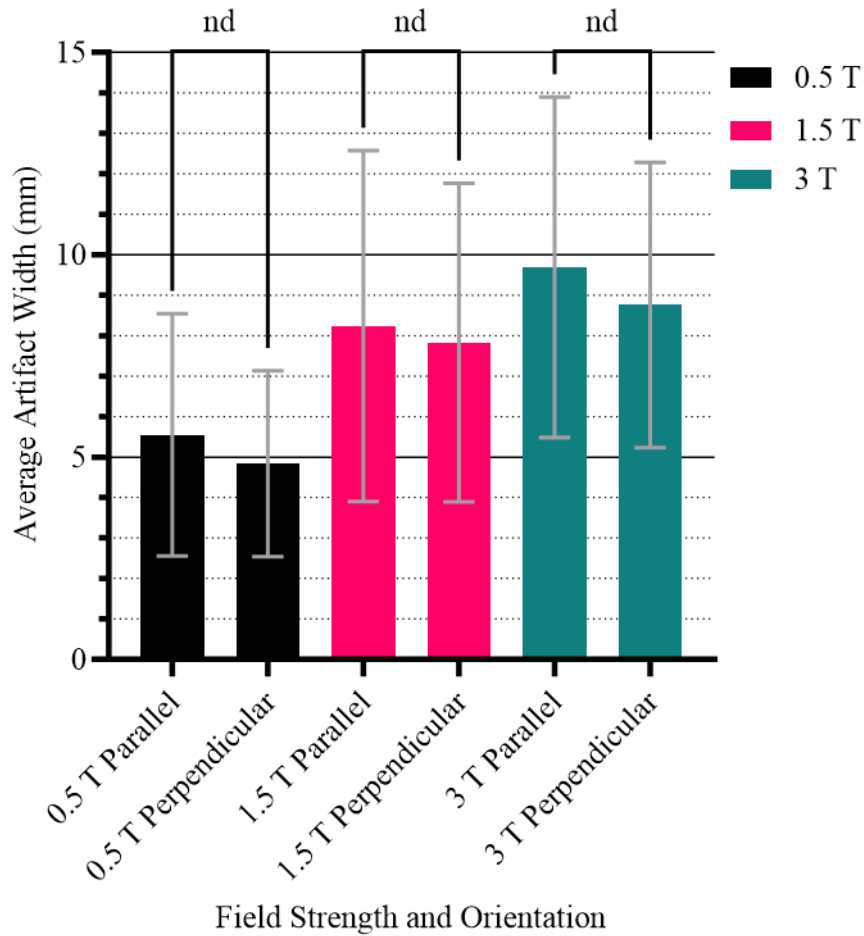


Figure 4.4: Bulk device orientation effects for the staple.

### 4.1.2    Stent Results

A representative selection of ROI images displaying the various morphologies of susceptibility artifacts caused by the stent is provided in Figure 4.5. Hyperintense and hypointense regions were present to varying degrees on the image but were drastically reduced relative to those seen with the staple in Figure 4.1. The approximate geometry of the stent could be visualized to varying degrees, as seen in subfigures of Figure 4.1: (**a**) parallel TOF-MRA at 0.5 T, (**b**) perpendicular TOF-MRA at 3 T, (**c**) parallel DWI at 0.5

T, and (**d**) perpendicular DWI at 0.5 T. In these TOF-MRA images, the decreased signal

intensity is proximal to the stent, while the hyperintense regions are relegated slightly

further to the periphery. The artifact fringe appears close to the stent, allowing

visualization of the lumen and the subtle features such as the slight bend in the stent. In

contrast, the DWI images of (**c**) and (**d**) only portray the general cylindrical shape of the

stent and have more pronounced hyperintense and hypointense regions.
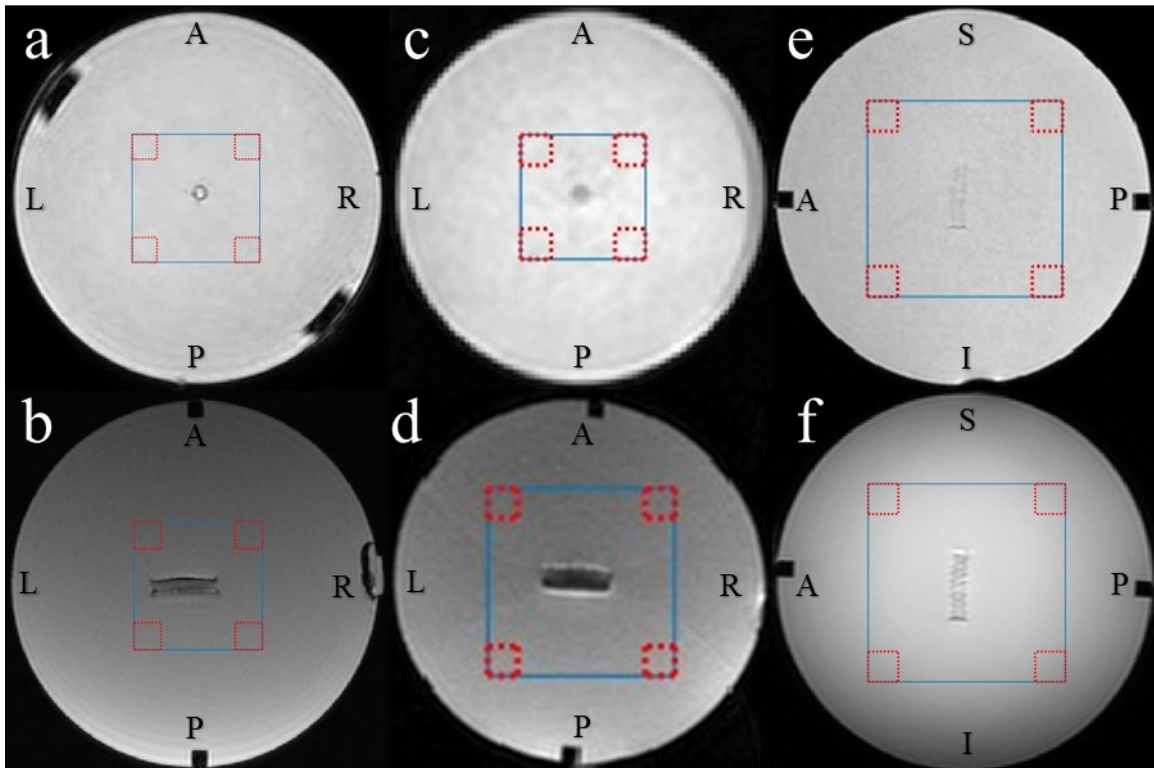


Figure 4.5 Representative images of stent susceptibility artifact. Legend: (a) parallel TOF-MRA at 0.5 T, (b) perpendicular TOF-MRA at 3 T, (c) parallel DWI at 0.5 T, (d) perpendicular DWI at 1.5 T, (e) parallel T1 FLAIR at 0.5 T, and (f) parallel T1 FLAIR at 3 T.

Stent artifact images also exhibited greater asymmetry in the distribution of

hyperintense and hypointense signal that was not apparent in the staple images,

particularly at higher fields. Examining the T1 FLAIR image at 3 T shown in subfigure

(**f**) of Figure 4.5, artifacts near the openings of the stent appear to be considerably larger

than those seen near the center of the stent. Additionally, each end displays a different type of artifact, with the top showing hyperintensity and the bottom showing hypointensity. The measurements of stent artifact width allow a more comprehensive description of artifact, the results of which are provided in Figure 4.6 and Figure 4.7 for the parallel and perpendicular orientation, respectively.
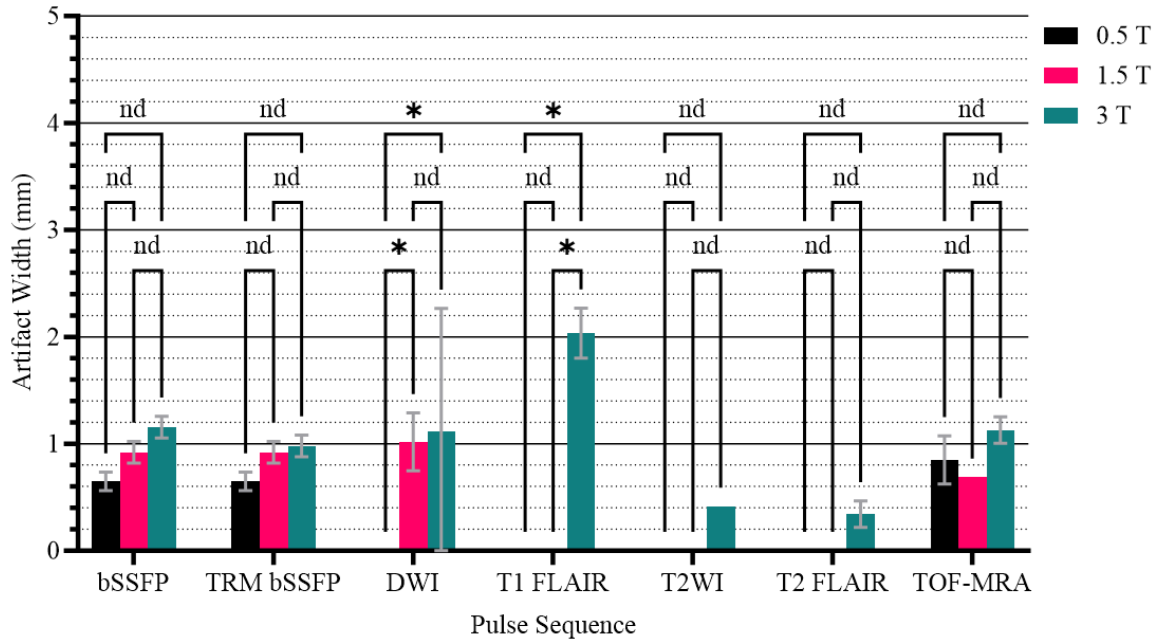


Figure 4.6 Artifact width produced by the stent in parallel orientation.
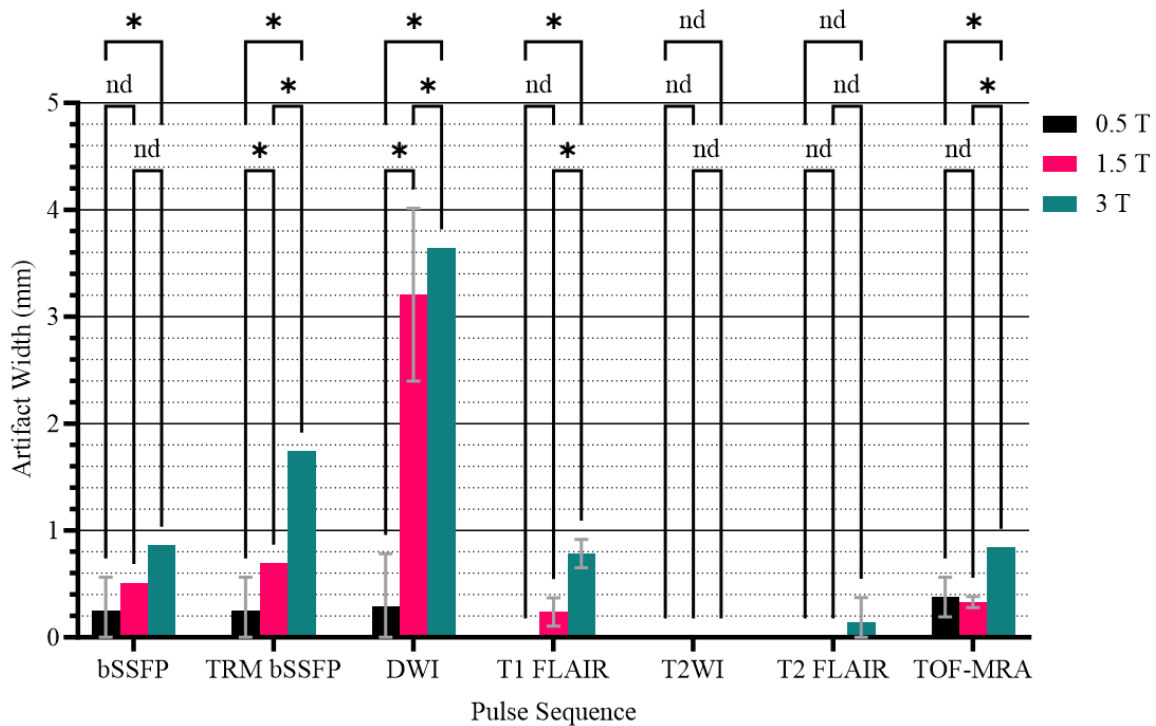
Figure 4.7 Artifact width produced by the stent in perpendicular orientation.

In Figure 4.6 and Figure 4.7 the observation of minimal data variation or non-existent measurable artifact width is a notable finding. Due to the reduced artifact width produced by the stent, it was observed that the artifact width measurements calculated through the artifact measurement pipeline become increasingly granular as a function of the lower number of voxels exhibiting artifactual signal. This is evidenced by the lack of error bars on some measurements, where triplicate measurements occurred.

Of the 28 tested comparisons between 0.5 T and 1.5/3T, 10 tests were deemed significant following FDR correction. Those 10 statistically significant comparisons indicated that 0.5 T produced less artifact width than the 1.5/3 T MRIs. The remaining 18 tests did not reach significance; therefore, no statistical tests indicated that the artifact width was increased at 0.5 T relative to 1.5 T or 3 T for the stent. The artifact widths produced by the stent averaged across clinical pulse sequences and orientations are 0.20 ± 0.33 mm, 0.58 ± 0.91 mm, and 1.04 ± 1.00 mm, corresponding to the 0.5 T, 1.5 T, and

3 T MRIs, respectively. As seen with the staple, there is considerable variability between pulse sequence results. Artifact widths ranged in size from no measurable artifact up to $3.64 \pm 0.00$ mm (triplicate measurements) produced by DWI at 3 T in the perpendicular orientation.

Clinical protocolling effects are still apparent between TRM bSSFP and bSSFP in perpendicular orientation comparisons. The TRM bSSFP results displayed a significant field dependent trend in artifact width ($0.25 \pm 0.31$ mm at 0.5 T, $0.69 \pm 0.00$ mm at 1.5 T, and $1.74 \pm 0.00$ mm at 3 T). In contrast, the only bSSFP comparison to reach significance was between 0.5 T ($0.25 \pm 0.31$ mm) and 3 T ($0.86 \pm 0.00$ mm).

Regarding orientation effects, four out of 21 tested comparisons were found to be significant when the stent is oriented along the field, where two out of four significant comparisons are between 0.5 T and 3 T. In the perpendicular orientation, the number of statistically significant differences increased to 11 out of 21 tested comparisons. In the parallel orientation, the average artifact width measurements for the stent were $0.25 \pm 0.38$ mm, $0.44 \pm 0.47$ mm, and $1.03$ mm $\pm 0.71$ mm, which correspond to the 0.5 T, 1.5 T, and 3 T systems, respectively. The corresponding average stent artifact widths in the perpendicular orientation are $0.15 \pm 0.27$ mm, $0.71 \pm 1.20$ mm, and $1.04 \pm 1.25$ mm, respectively. These two sets of average measurements do not include the TRM bSSFP pulse sequence results. In agreement with the staple's results, the dependence of artifact width on orientation was not found to be statistically significant for any field strength. The bulk orientation effect results for the stent are presented in Figure 4.8.

65
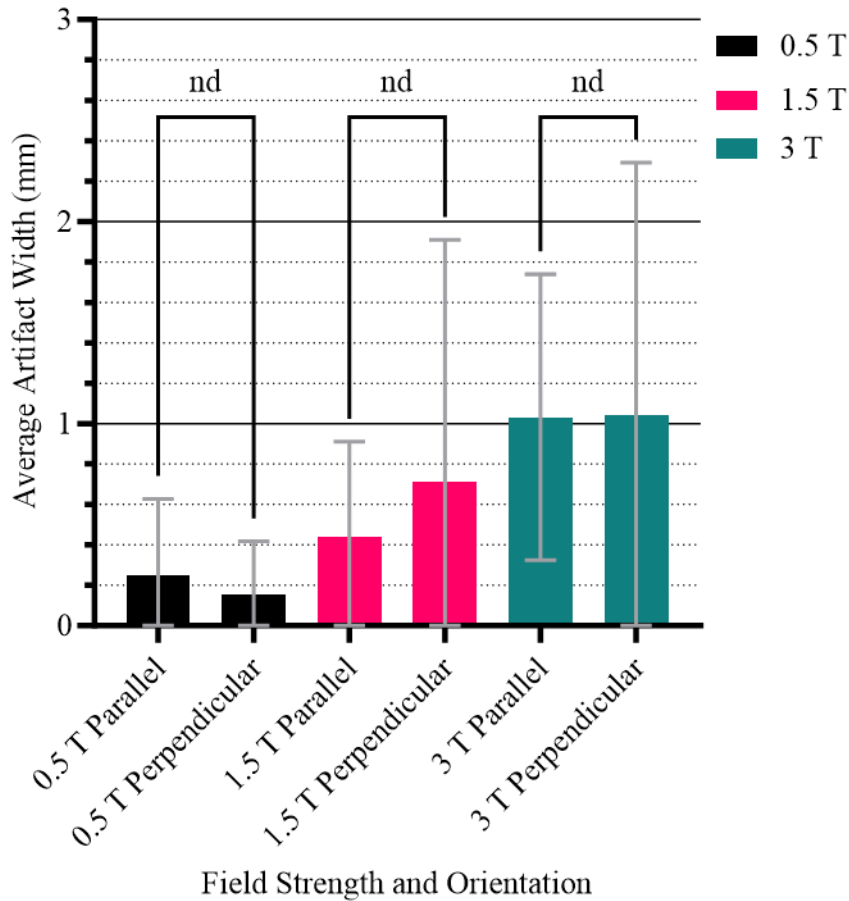
Figure 4.8: Bulk device orientation effects for the stent.

### 4.1.3 Endovascular Coil Results

Images of the endovascular coil appeared to be the least affected by susceptibility artifacts relative to the staple and stent. Representative images of the artifact produced by the endovascular coil are provided in Figure 4.9. Artifacts consisted of a decrease in signal intensity close to the device with limited areas of hyperintense signal near the periphery. Examples can be seen in subfigures (**a**) and (**b**) of Figure 4.9, which are both TOF-MRA. Despite the presence of some hyperintense and hypointense regions, the DWI images, shown in (**c**) and (**d**), were able to resolve the general shape of the endovascular coil, and could even visualize the center of the device in (**d**). Some pulse sequences, like the T2WI shown in (**e**) and (**f**), produced no measurable artifact.

However, some hyperintensity still appears where there should not be any signal (i.e., in the device's location).
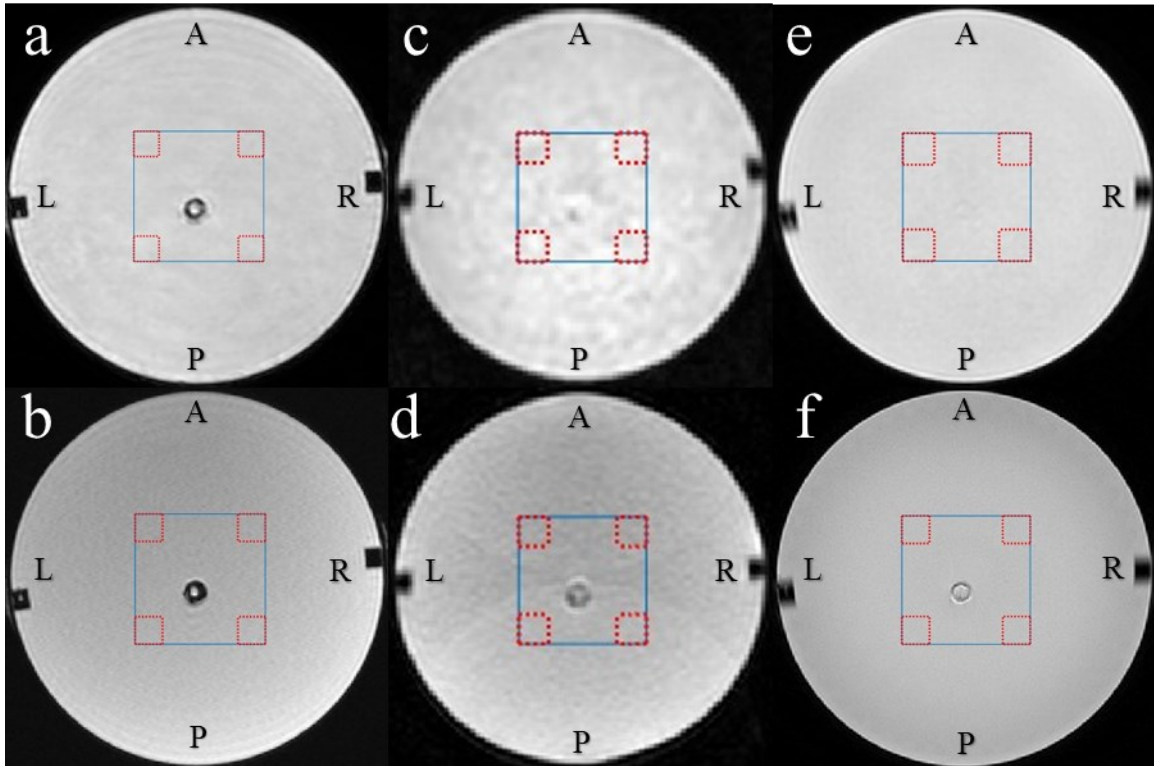


Figure 4.9 Representative images of endovascular coil susceptibility artifact. Recall the endovascular coil is only imaged in the perpendicular orientation. Legend: (**a**) TOF-MRA at 0.5 T, (**b**) TOF-MRA at 3 T, (**c**) DWI at 0.5 T, (**d**) DWI at 1.5 T, (**e**) T2WI at 0.5 T, and (**f**) T2WI at 3 T.

Artifact width measurement results for the endovascular coil are provided in Figure 4.10.
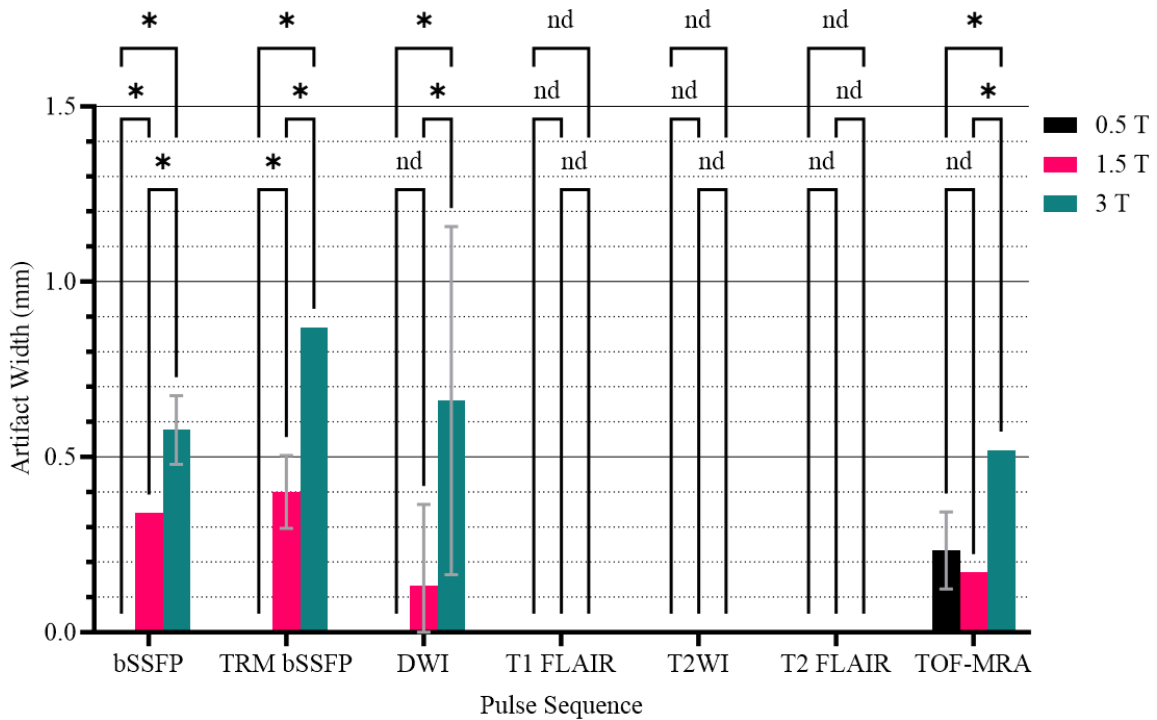
Figure 4.10 Artifact width produced by the endovascular coil in perpendicular orientation. Recall the T1 FLAIR has been reoriented from the sagittal to the axial plane for the endovascular coil.

In agreement with a visual examination of the images of the endovascular coil in Figure 4.9, the measured artifact width was minimal relative to the other two tested devices. As with the decreased artifact observed with the stent, the further reduced artifact width here results in additional granularity and replicate results. However, 10 out of 21 comparisons reached significance for the endovascular coil, of which six indicated artifact reduction at 0.5 T relative to 1.5/3T. In the TRM bSSFP and bSSFP sequences the 0.5 T had significantly reduced artifact relative to 1.5 T and 3 T, while only outperforming the 3 T in DWI and TOF-MRA. The remaining four significant comparisons indicated reduced artifact at 1.5 T relative to 3 T.

The artifact width for the endovascular coil ranged from no measurable artifact up to a maximum average of $0.87 \pm 0.00$ mm for the TRM bSSFP at 3 T. The three SE-based sequences (T1 FLAIR, T2WI, and T2 FLAIR) did not produce any measurable

artifact width, which agrees with the expectation of reduced artifacts when using SE

imaging. Across the clinical pulse sequences, the average artifact width for 0.5 T, 1.5 T,

and 3 T MRIs is $0.04 \pm 0.10$ mm, $0.11 \pm 0.15$ mm, and $0.29 \pm 0.35$ mm, respectively.

Again, these do not include the TRM bSSFP pulse sequence. It should also be noted that

these standard deviation values are approaching or below the smallest pixel size

(approximately 0.3 mm) of the tested pulse sequences.

Parameter-matching effects are less apparent with the endovascular coil than with

other tested devices. Both the bSSFP and TRM bSSFP results displayed a significant

field dependent trend in both orientations, with the lower fields consistently producing

less artifact width than higher fields.

## 4.2 TRM bSSFP Field Distortion Model

Representative images from the TRM bSSFP field distortion model are provided in

Figure 4.11.
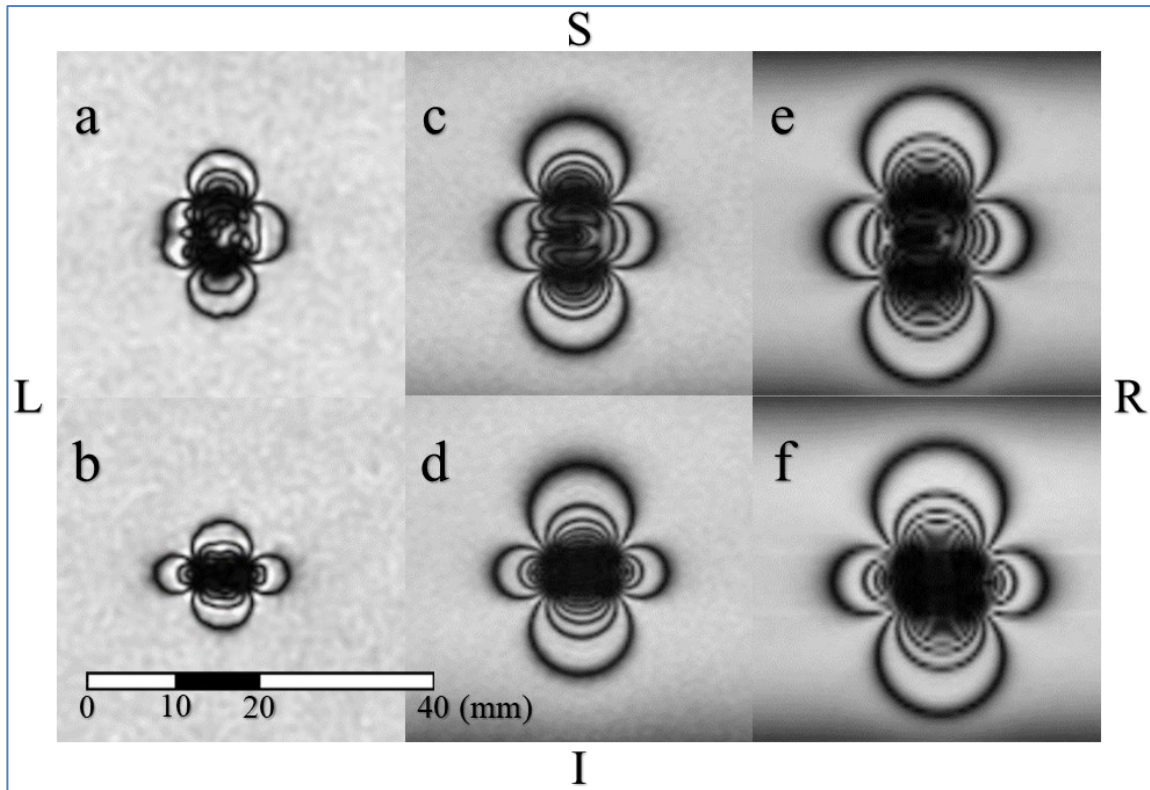
Figure 4.11 Coronal reformatted images of TRM bSSFP field distortion model. Legend: **(a)** parallel at 0.5 T, **(b)** perpendicular at 0.5 T, **(c)** parallel at 1.5 T, **(d)** perpendicular at 1.5 T, **(e)** parallel at 3 T, and **(f)** perpendicular at 3 T.

Coronal reformatted images are displayed in Figure 4.11 as they exhibit the characteristic dipolar field pattern. All subfigures use the scale in the figure's bottom left-hand side. From left to right on the top row, subfigures **(a)**, **(c)**, and **(e)** are the staple in the parallel orientation. While the **(b)**, **(d)**, and **(f)** in the bottom row represent the same field progression but with the staple in the perpendicular orientation. The outermost banding artifact for a TR of 7 ms occurs at a field offset equal to a ± 70 Hz shift from the expected resonant frequency. The field dependence of susceptibility-induced field distortions is immediately apparent in these images. The banding artifacts are confined at 0.5 T, where the "C" shape of the staple is nearly discernable in **(a)**. As the field strength increases to 3 T, the field distortions spread further away from the device, and the bands become smoother and more symmetrical around the staple. Measurements from the TRM

bSSFP field distortion model are provided in Figure 4.12.
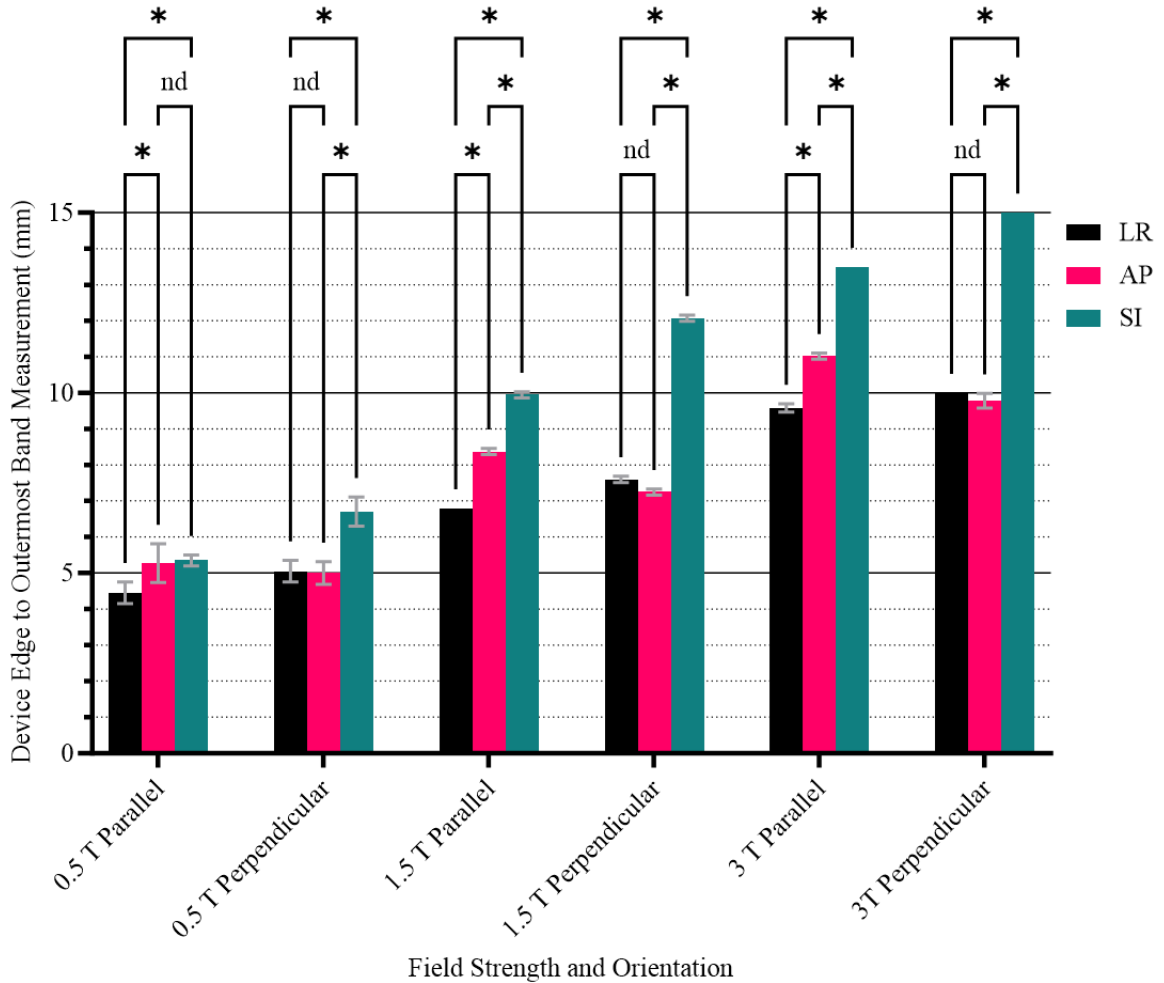


Figure 4.12 TRM bSSFP field distortion model banding artifact measurements.

The results shown in Figure 4.12 represent the average measured distance from

the staple to the location where the field offset reaches $\pm70$ Hz of background in each

cardinal direction. Two key patterns are immediately apparent: the distortion created by

the staple does not extend uniformly from the device, and the staple's orientation relative

to $B_0$ impacts the morphology of the field distortion. Examining the results in Figure

4.12, the field distortions extended significantly further away from the device in the SI

direction compared to both the AP and LR direction for all fields and device orientations

with the exception of SI and AP distortions being comparable at 0.5 T in the parallel

orientation (AP = 5.28 ± 0.54 mm and SI = 5.35 ± 0.15 mm). A notable difference can

also be observed when comparing parallel and perpendicular results. In the parallel

orientation the distortions lying in the axial plane are asymmetric, with field distortions

projecting significantly further from the staple in the AP direction than the LR. However,

there is no statistical difference between AP and LR distortions when the staple is in the

perpendicular orientation.

## 4.3    RF Shielding Characterization

A summary of the in-stent lumen signal reduction measurements is provided in Figure

4.13.
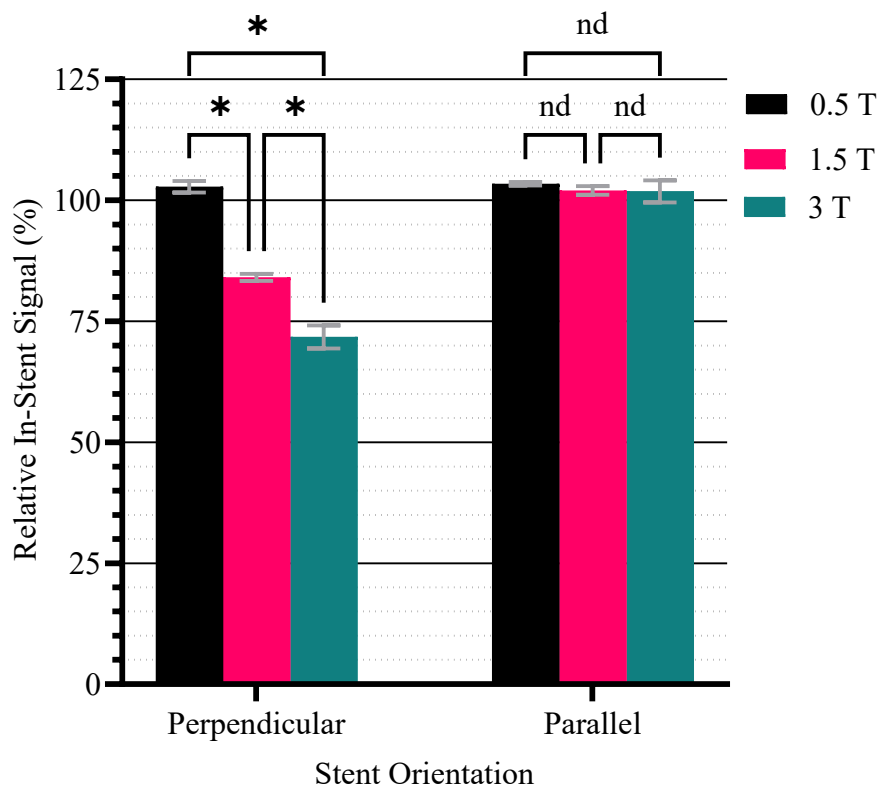


Figure 4.13 Average in-stent signal relative to background with TOF-MRA pulse
sequences.

When the stent was oriented parallel to $B_0$, the relative in-stent signal was

measured to be 103.4 ± 0.4%, 102.0 ± 0.9%, and 101.8 ± 2.3% at 0.5 T, 1.5 T, and 3 T

respectively. Furthermore, statistical testing did not find a significant relationship between relative in-stent signal and field strength in the parallel orientation. Conversely, in the perpendicular orientation the equivalent results were $102.8 \pm 1.2\%$, $84.1 \pm 0.7\%$, and $71.8 \pm 2.4\%$, respectively, which were all found to be statistically different from one another. This indicates a strong field dependence of RF shielding in the perpendicular orientation.

# Chapter 5: Discussion and Conclusions

The results discussed here provide insights into the characteristics of susceptibility-induced artifacts created by passive metal devices. Our findings indicate the field strength of the MRI does not solely determine artifacts. Various factors, including device geometry and composition, the pulse sequence used, and notably the compromises and trade-offs made during clinical protocolling, were observed to influence artifact width. This chapter first discusses the device-related effects, including results of the TRM bSSFP distortion model, followed by a review of pulse sequence and clinical protocolling effects. The merits of the TRM bSSFP distortion model are examined before the RF shielding results are reviewed. This research's potential clinical implications and limitations are provided before presenting recommendations for future work and overall conclusions.

## 5.1 Medical Device Effects

The susceptibility artifacts produced by the staple, stent, and endovascular coil each present unique challenges in MRI. Specifically, their material of construction and geometric design influence the susceptibility artifact width they produce. This section discusses these aspects for each device. Additionally, Section 5.1.1 will emphasize the link between artifact width and the TRM bSSFP field distortion model results.

### 5.1.1 Staple Discussion

The staple produced the largest and most severe artifacts of the tested devices based on the observed large hypointense and hyperintense regions as well as the complete obscuration of the device. This aligns with expectations, as the magnetic susceptibility values for stainless steel is on the order of 3500 – 6700 ppm, which is more than an order

of magnitude larger the values for nitinol (245 ppm) and platinum (279 ppm)[47]. The susceptibility-induced field distortions created by the staple ultimately result in large spatial-frequency mapping errors, indicating the hypointensities and hyperintensities observed on the images are signal voids and pileups, respectively. Some amount of accelerated dephasing is contributing to the signal void near the staple in GRE-based pulse sequences. However, distinguishing between the two mechanisms when using protocolled sequences is difficult.

The 0.5 T MRI demonstrated a reduction in artifact width across various orientations and sequences for the staple, with 22 out of 28 t-tests proving a statistically significant reduction relative to 1.5/3 T. A few of the notable exceptions are discussed in Section 5.2.

Bulk orientation effects for the staple were not found to have a statistically significant effect on measured artifact width. Initially, this finding is surprising because it contradicts the common advice of aligning the long axis of devices with the main magnetic field to reduce susceptibility artifacts[58,91,92]. The approximately oval shape of the staple may explain the exception. In cases with round or circular devices, the concept of a "long axis" for alignment and artifact reduction is less applicable. In such cases, artifacts are typically more problematic, and orientation has limited effect[91].

The TRM bSSFP distortion model highlighted the complexity of susceptibility-induced distortions that objects with unique geometry like the staple can induce. Distortions in the SI direction were nearly always significantly larger than those in the AP or LR direction. In the axial plane with the staple in the perpendicular orientation, no significant difference was found between field distortions extending from the staple in

the AP and LR directions. Alternatively, when oriented parallel to the main field, the distortions were greater in the AP than the LR direction. These observations only speak to the overall extent of the field distortion, with greater complexity possible closer to the staple. The complex distortion pattern likely explains the minor dependence of artifact width on device orientation. These effects are discussed further on a pulse sequence basis in 5.2.

Except for T2WI and T2 FLAIR, the direction of phase and frequency encoding in the routine brain imaging protocol tested here were consistent across each field strength. Therefore, the observed field dependence of artifact width does not depend on FE and PE directions, with the exception of T2WI and T2 FLAIR (discussed further in 5.2.4 and 5.2.5, respectively).

### 5.1.2 Stent Discussion

While markedly reduced compared to the staple, the susceptibility artifacts associated with the stent still presented measurable artifacts that could affect the diagnostic utility of the images. The outside of the stent and the stent lumen can be visualized in most pulse sequences to varying degrees. The notable exception here is the DWI sequence. RF shielding factors contribute to stent lumen visibility and are further discussed in Section 5.4. The reduced magnetic susceptibility of the nitinol used to construct the stent relative to the higher susceptibility 316L stainless steel staple is likely the primary reason for the artifact reduction. Researchers who have compared different types of stents observed similar results when comparing nitinol and stainless steel. For example, Heinrich et al[93] found the artifact produced by stainless steel stents could produce artifact widths up to six times larger than that produced by nitinol stents when using gradient echo pulse

sequences.

Stent orientation was not found to significantly affect artifact width results. Our contradictory results do not fully align with reports of reduced artifact when stents are oriented parallel to $B_0$ [2,93], which would be expected to apply here given similar geometry and materials used. Upon further review, the methods of assessing artifacts in both referenced works differ from those used here. We consider signal void and pileup artifacts and measure the stent in many possible horizontal and vertical locations to capture the largest artifact width. Whereas the work done by Klemm et al[2] measures signal void but not signal pileup, and Heinrich et al[93] only considers artifacts in the stent diameter dimension, which is measured semi-automatically in one location. These methodological differences coupled with the potentially confounding effects of a small sample size appear to account for the observed discrepancies. The location where the largest artifact was measured in this study often varied between the radial and longitudinal dimensions of the stent, with several of the largest artifacts being measured at the very end of the stent, where the field distortion appears to bloom near the pointed ends of the stent wires.

### 5.1.3 Endovascular Coil Discussion

Visual observation and artifact width measurements indicate the endovascular coil produced the smallest artifacts of the tested devices. The artifact appeared confined very close to the endovascular coil, aligning with observations made by Shellock et al[94] in another endovascular coil artifact study. The low artifact width is likely due to its light weight, small size, and platinum's low magnetic susceptibility. The T1 FLAIR, T2WI, and T2 FAIR produced no measurable artifact width at all tested fields. The small and

consistent size of the measured artifact width indicates the design of the tested

endovascular coil is relatively well suited for use where follow-up imaging is expected.

However, as artifacts are still present in TOF-MRA, there may be specific imaging

scenarios where artifacts hinder detailed visualization of the tissues adjacent to the

endovascular coil.

We did not test the orientation effects on susceptibility artifacts as they are

generally irrelevant given the spherical-like morphology of endovascular coils within an

aneurysm, flexible and variable geometry, and the frequent use of multiple endovascular

coils. It is essential to acknowledge these limitations when interpreting the results of our

single endovascular coil phantom test. However, our results indicate a general field-

dependent behavior of artifact width for the three tested devices, each having unique

geometry and materials of construction. Therefore, 0.5 T would be expected to produce

less artifact width relative to 1.5/3 T, particularly in a patient with multiple endovascular

coils, as we observed greater advantages at 0.5 T when larger susceptibility distortions

were present.

## 5.2 Pulse Sequences and Clinical Protocolling Effects

This section examines each pulse sequence and discusses relevant aspects of clinical

protocolling that likely contributed to the susceptibility artifact width results. The pulse

sequences are discussed alphabetically as they have been presented thus far.

### 5.2.1 bSSFP Discussion

As discussed in Section 3.2.2 and Section 3.3.2, the banding artifacts in bSSFP sequences

are a function of the induced field distortion and TR, with a shorter TR resulting in

reduced artifact for a given field distortion. In the protocolled bSSFP sequences, the TR

values of 7.0 ms, 5.8 ms, and 5.7 ms correspond to 0.5 T, 1.5 T, and 3 T, respectively. The trade-off made at higher fields to create a pulse sequence more resistant to banding artifact is a minor loss in SNR efficiency, as it is proportional to the square root of TR[74].

The more advanced bSSFP (FIESTA-C) technique is employed at 3 T only. The power of the 3 T bSSFP (FIESTA-C) technique is most evident when compared to the 0.5 T bSSFP and the 3 T TRM bSSFP staple artifact width measurements presented in Figure 4.2 and Figure 4.3. The protocolled bSSFP (FIESTA-C) produces comparable artifact width at 3 T to the bSSFP at 0.5 T, despite the 6-fold increase in field strength. These results are visually echoed in Figure 4.1, by comparing subfigures (**d**) 0.5 T bSSFP to (**e**) 3 T TRM bSSFP and (**f**) 3 T bSSFP (FIESTA-C). It must be noted that the bSSFP (FIESTA-C) method can still break down in areas with large susceptibility distortions, as seen near the staple in Figure 4.1 subfigure (**f**). This may contribute to decreased bSSFP (FIESTA-C) performance when imaging the stent and endovascular coil. As their reduced magnetic susceptibility results in decreased field distortions, the location of the outermost banding artifact is moved close to the device where the susceptibility-induced magnetic fields have larger spatial gradients.

Overall, clinical protocoling of bSSFP (FIESTA-C) at 3 T reduced visual artifacts and artifact widths to levels comparable to 0.5 T, effectively minimizing the impact of increased magnetic susceptibility-induced field distortions. However, the trade-off cost to implement this technique is essentially doubling in scan time. The scan time of bSSFP (FIESTA-C) at 3 T requires 3 minutes and 56 seconds, while 4 minutes and 36 seconds is necessary for bSSFP at 0.5 T. Therefore, although the protocolling decisions mitigated artifacts at 3 T, the trade-off in scan time lessened the impact of longer scan times at

lower fields, resulting in comparable scan times at 0.5 T.

## 5.2.2 DWI Discussion

Several trade-offs were identified at 1.5/3 T to mitigate susceptibility artifacts in DWI scans: increasing BW/FOV, reducing effective TE, and increasing the acquisition matrix size. At 1.5 T and 3 T, BW/FOV is 22,727 Hz/cm, whereas at 0.5 T, it is only 16,000 Hz/cm. Higher BW/FOV is feasible at higher fields as the SNR is sufficient to be traded for greater receiver BW while maintaining short scans and appropriate FOV. In theory, for a given field distortion, an increase in BW/FOV equal to that observed here would result in a nearly 30% reduction to in-plane FE errors due to signal displacement.

When imaging at 3 T, additional SNR was available to further accelerate the EPI acquisition by using a PI factor of 4 instead of the factor of 2 used at 0.5 T and 1.5 T. Completing the EPI acquisition faster reduces the time available for accelerated intravoxel phase dispersion due to susceptibility distortions, thus reducing artifacts. By increasing the PI factor from 2 to 4, the effective TE value can be decreased from the ~80 ms values seen at 0.5 T and 1.5 T to 58 ms at 3 T. This minimization of effective TE while maintaining sufficient SNR is in line with the results of a DWI protocol optimization study[95].

The slice thicknesses were nearly identical (5.5 mm at 0.5 T and 5 mm at 1.5/3 T), but the acquisition matrix was substantially larger at 1.5 T (acquisition matrix sizes are 120 x 120 at 0.5 T, 192 x 160 at 1.5 T, and 128 x 128 at 3 T). Increasing the matrix size reduces the effects of accelerated intravoxel dephasing, resulting in reduced signal loss.

Despite the protocolling choices made to limit the extent of susceptibility artifact

in the DWI pulse sequences, DWI artifact widths were often the largest of the tested sequences. This is attributed to the EPI-based acquisition, which is highly sensitive to magnetic field distortions.

### 5.2.3 T1 FLAIR Discussion

None of the tested T1 FLAIR sequences used advanced artifact reduction techniques. Slice thickness measured 5 mm on all scanners, while BW/FOV is set to $\pm$ 2,667 Hz/cm at 0.5 T and $\pm$ 2,604 Hz/cm at both 1.5 T and 3 T. The similarity in these parameters indicates that trade-offs to increase the susceptibility artifact resistance of these sequences are typically not required in the routine case for a sagittal prescription. This agrees with the general use of T1 FLAIR in areas with relatively low anatomical susceptibility-induced field distortions and the increased robustness of a SE sequence.

The T1 FLAIR is the only pulse sequence imaged in the sagittal plane. The exception is axial prescription used for the endovascular coil due to phantom and geometrical limitations. Field dependence was generally followed and there were no cases where measured artifact width was reduced at a higher field. Additionally, artifact width was significantly decreased at 0.5 T in six out of the 10 statistically tested comparisons. As demonstrated with the TRM bSSFP model, the staple's orientation relative to $B_0$ appears to have a larger effect on field distortions produced in the SI direction compared to the AP or LR directions. This may explain some orientation-dependent variability in the T1 FLAIR artifact width measurements.

### 5.2.4 T2WI Discussion

As with the T1 FLAIR, the 2D fast SE-based T2WI followed the expected field dependence in all tested conditions. Recall the T2WI has a cartesian acquisition at 0.5 T

and a PROPELLER acquisition at 1.5 T and 3 T. The PROPELLER acquisition has improved resistance to motion and pulsation artifact[80] but is more sensitive to susceptibility-induced field distortions[96] and requires longer scan times. The BW/FOV values of ± 5,760 Hz/cm at 0.5 T, ± 5,862 Hz/cm at 1.5 T, and ± 4,545 Hz/cm at 3 T, were the largest of the tested SE sequences by a considerable margin. The T2WI artifact widths were comparable to T2 FLAIR and consistently produced below-average artifact widths. The T2WI artifact width was significantly reduced at 0.5 T in three out of four tested comparisons with the staple. When imaging the stent and coil, artifact width was not found to be significantly reduced at 0.5 T, primarily due to a lack of artifact width at all field strengths. This trend aligns with what would be expected of a large BW/FOV SE sequence at 0.5 T.

### 5.2.5   T2 FLAIR Discussion

The T2 FLAIR is the final 2D SE sequence. Unlike the T2WI, this sequence uses a cartesian acquisition at all field strengths. The slice thicknesses are 5.5 mm, at 0.5 T, and 5 mm at 1.5 T and 3 T, which are identical to T2WI values. BW/FOV values for this sequence are ± 3,840 Hz/cm at 0.5 T, ± 2,273 Hz/cm at 1.5 T, and ± 3,788Hz/cm at 3 T. The statistical decrease in artifact at 0.5 T in all four tested comparisons with the staple is understood by considering the large BW/FOV at 0.5T and its decreased field strength. This is further evidenced in the general lack of artifact width when imaging the lower susceptibility stent and coil.

Interestingly, the BW/FOV values were considerably lower with T2 FLAIR than with T2WI despite the comparable artifact widths at 1.5/3 T. This may be a result of the T2WIs PROPELLER acquisition increasing artifact but also SNR, which is subsequently

reined in by increasing BW/FOV.

## 5.2.6   TOF-MRA Discussion

Significant artifact width reduction using the 0.5 T relative to 1.5/3 T was only found when imaging the staple. However, the 0.5 T did not offer a vast improvement over that of 1.5 T and 3 T, with approximately 2.5 mm separating the three average artifact width measurements for the staple. In the stent and endovascular coil tests, the 1.5 T produced comparable artifact width to 0.5 T, and the 3 T produced comparable artifact width to 0.5 T with the stent in the parallel orientation. This can be attributed to protocolling decisions affecting the TE, BW, and acquisition matrix size. The BW/FOV at 0.5 T was $\pm$ 1,250 Hz/cm, rising to $\pm$ 3,125 Hz/cm at 1.5 T and $\pm$ 2,841 Hz/cm at 3 T. The TE at 0.5 T was 6.0 ms, compared to the much shorter TEs of 2.6 ms and 3.1 ms at 1.5 T and 3 T, respectively. Considering this along with the increased acquisition matrix size at 1.5 T and 3 T, the comparable artifact width can be contextualized. Protocolling decisions leveraged the higher SNR available in TOF-MRA at 1.5/3 T to mitigate the effects of susceptibility-induced field distortions while providing improved scan times.

## 5.3   TRM bSSFP Field Distortion Model

This model provides a visual description of the field distortion pattern produced by the staple and provides valuable context to the artifact width results discussed in Sections 5.1 and 5.2. The field distortions produced by the staple appear complex and have some orientation dependence. The low measurement variability is a good indication of the model's reliability. However, a numerical magnetostatic field simulation is recommended to validate the model's assumptions.

## 5.4   RF Shielding

The orientation dependence observed in the RF shielding results are likely due to the stent's construction. Bouillot et al[97] thoroughly investigated the effects of stent orientation and construction on RF shielding effects. Specifically, they suggest the contact points where individual wires overlap in braided stents have insufficient conductance. This low conductance minimizes the magnitude of any induced eddy currents. Conversely, the wires themselves have a helical coil-like shape and would be expected to have relatively high conductance. This leads to shielding effects that depend on device orientation relative to the incident RF pulses. In MRI, the direction of the RF pulse is always oriented perpendicular to the main magnetic field[98]. The loops in which this changing magnetic field can induce current will also be perpendicular to the main magnetic field. This rationale explains why the stent lumen is shielded in the perpendicular orientation but not the parallel orientation.

Concerning the differences in RF shielding observed in the perpendicular orientation, the concept of skin depth provides a likely explanation. Skin depth is the distance an electromagnetic wave will penetrate a conductor before its amplitude is attenuated to about 37%[*] of its initial value. It is a function based on the shielding material properties and the incident wave frequency, with higher frequency waves being attenuated in a shorter distance[99]. RF pulses represent the incident waves in MRI, which have frequencies determined by the magnet's field strength. Therefore, for a given device, the lower frequency RF pulses inherent to low-field MRI will be attenuated to a lesser degree than those at mid and high field, resulting in reduced RF shielding and greater

---

*More specifically, the attenuation factor is $\frac{1}{e}$.

luminal signal intensity.

Another imaging advantage for low-field MRI is reduced SAR, which is relevant when using high SAR pulse sequences such as TOF-MRA. Klemm et al[2] demonstrated that relative in-stent signal is a function of flip angle, field strength, and stent properties such as material and construction. Kato et al[62] recently furthered this work, demonstrating that the optimal flip angle varied considerably between two stents, determining the optimal flip angle for one of the stents was 45°. This is much higher than the conventionally used 20°, which is the angle used by TOF-MRA at 1.5 T and 3 T. Therefore, the potential advantage to 0.5 T is the ability to use higher flip angles, and therefore greater SAR, as needed to better resolve stent lumen. This would not impose SAR-based constraints at low-field but may be a factor at 1.5 T and higher due to the SAR-intensive nature of TOF-MRA[38].

## 5.5   Clinical Implications

The findings of this study highlight the potential clinical implications for patient care, particularly for those with implanted or secured medical devices. The advantages of low-field MRI are evident, mainly by reducing susceptibility artifact caused by passive MR conditional devices without the use of specialized pulse sequences or the requirement for considerable trade-offs during protocolling. While the artifacts at lower fields do not disappear entirely, the reduced artifact size could lead to more accurate diagnoses and better treatment planning while providing better value in healthcare.

## 5.6   Challenges and Limitations

One limitation in this work is the small sample size, which is particularly relevant to the stent and endovascular coil artifact width results. A superficial visual assessment of the

stent artifact width results suggests there may be a larger advantage to low field than can be concluded here based on our statistical testing. However, many significant differences were found, and the overall trends point to a considerable advantage at 0.5 T.

Concerning potential errors in artifact width measurements, the devices were only measured before encapsulation in the phantom; as such, their dimensions may have changed slightly as the gelatine congealed. This may result in a slight incremental error in artifact width results, but this should not affect the conclusions of the work. To remediate this potential offset to the artifact widths presented here, an X-ray image or similar measurement could be used to validate device measurement post encapsulation.

Another device-specific limitation applies to the method in which the endovascular coil was secured within the phantom. We followed a similar methodology to a study performed by Shellock et al[94] but this is not entirely representative of how the endovascular coil is oriented *in vivo*. Multiple endovascular coils are used to embolize an aneurysm, resulting in a larger volume of magnetic material and a unique three-dimensional geometry. Our methodology was consistent between each field strength so a field dependence of artifact width would still be expected *in vivo*, but with the distinct possibility of increased artifact size. T1 FLAIR was also prescribed in the axial plane for the endovascular coil. This was required as the method used by the artifact characterization pipeline cannot handle the asymmetrical geometry of the endovascular coil in the SI direction and would likely produce considerable measurement errors affecting the study's results.

A setup limitation specific to the stent was the lack of flow effects. When a stent is implanted in a blood vessel, blood – having different magnetic properties than doped

gelatine – flows through it. Flow effects were not considered in this work as our methods were based on the ASTM F2119-07 standard, and the added cost and complexity associated with a vascular apparatus were deemed prohibitive to the scope of this work. Research evaluating the impact of flowing blood observed a phenomenon termed "rocket artifact," which is the displacement of the artifact along the direction of flow[61]. Figure 2.6 subfigure (**b**) shows a visual representation of this effect, where the hyperintensity at the upper side of the stent is shifted into the lumen. In contrast, at the bottom a larger hyperintensity appears to be exiting the stent. This type of effect is expected to be consistent across fields, and as such, our results should generally approximate the *in vivo* environment.

Finally, the routine brain imaging protocol used here is specific to our institution. Many different protocols and pulse sequence variations exist in the realm of MRI, often with institutional "flavors" of protocols and pulse sequences. However, the evidence of artifact field dependence when imaging with clinical protocols presented here could generally be expected at other institutions when using protocols of similar function. It is also important to note that the MRIs used in this study may differ from those available at other institutions.

## 5.7    Recommendations for Future Work

Three primary directions would be appropriate to extend this work. The first and most crucial avenue would be to plan and implement an *in vivo* validation study. Including radiologists in this work would enable the comparative evaluation of diagnostic utility between 0.5 T images and those produced on 1.5 and 3 T. This research would further clarify the role of modern low-field MRI in the clinic.

The second would extend the phantom methodology to include more commonly used passive devices and materials. These devices might include orthopedic hardware, surgical adjuncts, and orthodontic brackets and guidewires, which are expected to produce more substantial artifacts than the staple, stent, and endovascular coil tested here due to their size and magnetic susceptibility.

Finally, a framework should be created to evaluate the safety of active devices in low-field MRI. From an artifact and safety perspective, these are commonly the most problematic to image, as active devices such as hearing implants often require permanent magnets. Depending on these devices' design, the permanent magnet's surgical removal can be necessary before scanning at 1.5 T or 3 T [100]. The 0.5 T MRI may offer a potential safety advantage for imaging around active devices while reducing the extent of susceptibility artifact. The susceptibility characterization framework developed here could be combined with the recommended development of a safety assessment framework to evaluate active devices in low-field MRI efficiently.

## 5.8 Conclusions

A metal artifact characterization framework was developed primarily for systematically evaluating susceptibility artifacts in MRI. We hypothesized that when using routine imaging protocols, 0.5 T would produce images with less artifact width than 1.5 T and 3 T. Three high-use passive devices were evaluated *in vitro* with routine brain imaging protocols in current clinical use at our institution. Our hypothesis that metal artifacts would be reduced at 0.5 T relative to 1.5/3 T was statistically tested and proven true for many devices and pulse sequences, but not all. Ultimately, this study underscores the impact both field strength and clinical protocolling have on susceptibility

artifacts in MRI. However, the typical reduction in artifact width at low field strengths offers promising future avenues for improving the diagnostic quality of images in the presence of susceptibility-induced field distortions.

The observed benefits of low-field MRI systems suggest a potential shift in the paradigm of imaging patients with MR-conditional devices, particularly those made from higher magnetic susceptibility materials. Low-field MRI could be preferentially employed to optimize image quality and diagnostic utility in traditionally challenging imaging areas while improving value in health care. Recommended future research to make this a reality includes planning and conducting *in vivo* artifact studies to validate our findings and developing and implementing methodology to evaluate active devices from a safety and artifact perspective.

# References

1. CADTH. *The Canadian Medical Imaging Inventory 2019-2020*. CADTH health technology review; 2021. https://cadth.ca/sites/default/files/ou-tr/op0546-cmii3-final-report.pdf

2. Klemm T, Duda S, Machann J, et al. MR imaging in the presence of vascular stents: A systematic assessment of artifacts for various stent orientations, sequence types, and field strengths. *J Magn Reson Imaging*. 2000;12(4):606-615. doi:10.1002/1522-2586(200010)12:4<606::AID-JMRI14>3.0.CO;2-J

3. Wang Y, Truong TN, Yen C, et al. Quantitative evaluation of susceptibility and shielding effects of nitinol, platinum, cobalt-alloy, and stainless steel stents. *Magn Reson Med*. 2003;49(5):972-976. doi:10.1002/mrm.10450

4. Koch KM, Hargreaves BA, Pauly KB, Chen W, Gold GE, King KF. Magnetic resonance imaging near metal implants. *J Magn Reson Imaging*. 2010;32(4):773-787. doi:10.1002/jmri.22313

5. Patzig M, Forbrig R, Gruber M, Liebig T, Dorn F. The clinical value of ceMRA versus DSA for follow-up of intracranial aneurysms treated by coil embolization: an assessment of occlusion classifications and impact on treatment decisions. *Eur Radiol*. 2021;31(6):4104-4113. doi:10.1007/s00330-020-07492-3

6. U.S. Food & Drug Administration. Recognized Consensus Standards: Medical Devices - ASTM  F2119-07. Published online September 11, 2023. https://www.accessdata.fda.gov/scripts/cdrh/cfdocs/cfstandards/detail.cfm?standard__identification_no=31055

7. Bitar R, Leung G, Perng R, et al. MR Pulse Sequences: What Every Radiologist Wants to Know but Is Afraid to Ask. *RadioGraphics*. 2006;26(2):513-537. doi:10.1148/rg.262055063

8. Ehman EC, Johnson GB, Villanueva-Meyer JE, et al. PET/MRI: Where might it replace PET/CT? *Magnetic Resonance Imaging*. 2017;46(5):1247-1262. doi:10.1002/jmri.25711

9. Thompson SM, Gorny KR, Koepsel EMK, et al. Body Interventional MRI for Diagnostic and Interventional Radiologists: Current Practice and Future Prospects. *RadioGraphics*. 2021;41(6):1785-1801. doi:10.1148/rg.2021210040

10. Lurie DJ, Sharp PF. In memoriam: John R. Mallard (1927-2021). *Magnetic Resonance in Med*. 2021;86(4):1815-1817. doi:10.1002/mrm.28838

11. Smith FW, Mallard JR, Hutchison JMS, Reid A. NUCLEAR MAGNETIC RESONANCE TOMOGRAPHIC IMAGING IN LIVER DISEASE.: *Journal of Computer Assisted Tomography*. 1982;6(1):221. doi:10.1097/00004728-198202000-00071

12. Ai T, Morelli JN, Hu X, et al. A Historical Overview of Magnetic Resonance Imaging, Focusing on Technological Innovations: *Investigative Radiology*. 2012;47(12):725-741. doi:10.1097/RLI.0b013e318272d29f

13. Runge VM, Heverhagen JT. Advocating the Development of Next-Generation, Advanced-Design Low-Field Magnetic Resonance Systems. *Invest Radiol*. 2020;55(12):747-753. doi:10.1097/RLI.0000000000000703

14. Barisano G, Sepehrband F, Ma S, et al. Clinical 7 T MRI: Are we there yet? A review about magnetic resonance imaging at ultra-high field. *BJR*. 2019;92(1094):20180492. doi:10.1259/bjr.20180492

15. Hashemi RH, Lisanti CJ, Bradley WG. *MRI: The Basics*. Fourth edition. Wolters Kluwer; 2018.

16. Department of Veterans Affairs. MRI Design Guide. Published online April 2008. https://www.vendorportal.ecms.va.gov/FBODocumentServer/DocumentServer.aspx?DocumentId=2788394&FileName=VA261-16-R-0652-A00004002.pdf

17. Arnold TC, Freeman CW, Litt B, Stein JM. Low-field MRI: Clinical promise and challenges. *Magnetic Resonance Imaging*. 2023;57(1):25-44. doi:10.1002/jmri.28408

18. Swensen SJ, Johnson CD. Radiologic Quality and Safety: Mapping Value Into Radiology. *Journal of the American College of Radiology*. 2005;2(12):992-1000. doi:10.1016/j.jacr.2005.08.003

19. Sharma PS, Saindane AM. Standardizing Magnetic Resonance Imaging Protocols Across a Large Radiology Enterprise: Barriers and Solutions. *Current Problems in Diagnostic Radiology*. 2020;49(5):312-316. doi:10.1067/j.cpradiol.2020.01.012

20. Glazer DI, DiPiro PJ, Shinagare AB, et al. CT and MRI Protocol Variation and Optimization at an Academic Medical Center. *Journal of the American College of Radiology*. 2018;15(9):1254-1258. doi:10.1016/j.jacr.2018.06.002

21. Brown AD, Marotta TR. Using machine learning for sequence-level automated MRI protocol selection in neuroradiology. *Journal of the American Medical Informatics Association*. 2018;25(5):568-571. doi:10.1093/jamia/ocx125

22. Society for Cardiovascular Magnetic Resonance, Board of Trustees Task Force on Standardized Protocols, Kramer CM, et al. Standardized cardiovascular magnetic resonance (CMR) protocols 2013 update. *J Cardiovasc Magn Reson*. 2013;15(1):91. doi:10.1186/1532-429X-15-91

23. Brown RW, Cheng YCN, Haacke EM, Thompson MR, Venkatesan R. *Magnetic Resonance Imaging: Physical Principles and Sequence Design, 2nd Edition*. Second edition. John Wiley & Sons, Inc; 2014.

24. Traboulsee A, Simon JH, Stone L, et al. Revised Recommendations of the Consortium of MS Centers Task Force for a Standardized MRI Protocol and Clinical Guidelines for the Diagnosis and Follow-Up of Multiple Sclerosis. *AJNR Am J Neuroradiol*. 2016;37(3):394-401. doi:10.3174/ajnr.A4539

25. Westbrook C, Talbot J. *MRI in Practice*. Fifth edition. Wiley; 2018.

26. Jungmann PM, Agten CA, Pfirrmann CW, Sutter R. Advances in MRI around metal: MRI Around Metal. *J Magn Reson Imaging*. 2017;46(4):972-991. doi:10.1002/jmri.25708

27. Kabasawa H. MR Imaging in the 21st Century: Technical Innovation over the First Two Decades. *MRMS*. 2022;21(1):71-82. doi:10.2463/mrms.rev.2021-0011

28. Chavhan GB, Babyn PS, Jankharia BG, Cheng HLM, Shroff MM. Steady-State MR Imaging Sequences: Physics, Classification, and Clinical Applications. *RadioGraphics*. 2008;28(4):1147-1160. doi:10.1148/rg.284075031

29. Hennig J, Nauerth A, Friedburg H. RARE imaging: A fast imaging method for clinical MR. *Magn Reson Med*. 1986;3(6):823-833. doi:10.1002/mrm.1910030602

30. Roemer PB, Edelstein WA, Hayes CE, Souza SP, Mueller OM. The NMR phased array. *Magnetic Resonance in Med*. 1990;16(2):192-225. doi:10.1002/mrm.1910160203

31. Sodickson DK, Manning WJ. Simultaneous acquisition of spatial harmonics (SMASH): Fast imaging with radiofrequency coil arrays. *Magn Reson Med*. 1997;38(4):591-603. doi:10.1002/mrm.1910380414

32. Sodickson DK, Griswold MA, Jakob PM, Edelman RR, Manning WJ. Signal-to-noise ratio and signal-to-noise efficiency in SMASH imaging. *Magn Reson Med*. 1999;41(5):1009-1022. doi:10.1002/(SICI)1522-2594(199905)41:5<1009::AID-MRM21>3.0.CO;2-4

33. Marques JP, Simonis FFJ, Webb AG. Low-field MRI: An MR physics perspective. *Magnetic Resonance Imaging*. 2019;49(6):1528-1542. doi:10.1002/jmri.26637

34. Hori M, Hagiwara A, Goto M, Wada A, Aoki S. Low-Field Magnetic Resonance Imaging: Its History and Renaissance. *Invest Radiol*. 2021;56(11):669-679. doi:10.1097/RLI.0000000000000810

35. Shellock FG, Rosen MS, Webb A, et al. Managing Patients With Unlabeled Passive Implants on MR Systems Operating Below 1.5 T. *Magnetic Resonance Imaging*. Published online September 28, 2023:jmri.29002. doi:10.1002/jmri.29002

36. Panych LP, Madore B. The physics of MRI safety. *Magnetic Resonance Imaging*. 2018;47(1):28-43. doi:10.1002/jmri.25761

37. Delfino JG, Krainak DM, Flesher SA, Miller DL. MRI-related FDA adverse event reports: A 10-yr review. *Med Phys*. 2019;46(12):5562-5571. doi:10.1002/mp.13768

38. Allison J, Yanasak N. What MRI Sequences Produce the Highest Specific Absorption Rate (SAR), and Is There Something We Should Be Doing to Reduce the SAR During Standard Examinations? *American Journal of Roentgenology*. 2015;205(2):W140-W140. doi:10.2214/AJR.14.14173

39. U.S. Food & Drug Administration. *Testing and Labeling Medical Devices for Safety in the Magnetic Resonance (MR) Environment*.; 2023. https://www.fda.gov/media/74201/download

40. Shellock FG, Woods TO, Crues JV. MR Labeling Information for Implants and Devices: Explanation of Terminology. *Radiology*. 2009;253(1):26-30. doi:10.1148/radiol.2531091030

41. Shellock FG. *Reference Manual for Magnetic Resonance Safety, Implants, and Devices*. 2012 ed. Biomedical Research Publishing Group; 2012.

42. Kawabata I, Imai H, Kanno Z, et al. Three-dimensional quantification of magnetic resonance imaging artifacts associated with shape factors. *Dent Mater J*. 2019;38(4):638-645. doi:10.4012/dmj.2018-197

43. Hargreaves BA, Worters PW, Pauly KB, Pauly JM, Koch KM, Gold GE. Metal-Induced Artifacts in MRI. *American Journal of Roentgenology*. 2011;197(3):547-555. doi:10.2214/AJR.11.7364

44. Olsen RV, Munk PL, Lee MJ, et al. Metal Artifact Reduction Sequence: Early Clinical Applications. *RadioGraphics*. 2000;20(3):699-712. doi:10.1148/radiographics.20.3.g00ma10699

45. Viano AM, Gronemeyer SA, Haliloglu M, Hoffer FA. Improved MR imaging for patients with metallic implants☆. *Magnetic Resonance Imaging*. 2000;18(3):287-295. doi:10.1016/S0730-725X(99)00135-6

46. Chen CA, Chen W, Goodman SB, et al. New MR imaging methods for metallic implants in the knee: Artifact correction and clinical impact. *J Magn Reson Imaging*. 2011;33(5):1121-1127. doi:10.1002/jmri.22534

47. Schenck JF. The role of magnetic susceptibility in magnetic resonance imaging: MRI magnetic compatibility of the first and second kinds. *Med Phys*. 1996;23(6):815-850. doi:10.1118/1.597854

48. Khan S. Synaptive Medical Secures Health Canada Approval for Evry™. Synaptive Medical. Published February 20, 2020. Accessed September 17, 2023. https://www.synaptivemedical.com/synaptive-medical-secures-health-canada-approval-for-evry/

49. Lu W, Pauly KB, Gold GE, Pauly JM, Hargreaves BA. SEMAC: Slice encoding for metal artifact correction in MRI. *Magn Reson Med*. 2009;62(1):66-76. doi:10.1002/mrm.21967

50. Koch KM, Lorbiecki JE, Hinks RS, King KF. A multispectral three-dimensional acquisition technique for imaging near metal implants. *Magn Reson Med*. 2009;61(2):381-390. doi:10.1002/mrm.21856

51. Wichmann W, Von Ammon K, Fink U, Weik T, Yasargil GM. Aneurysm clips made of titanium: magnetic characteristics and artifacts in MR. *AJNR Am J Neuroradiol*. 1997;18(5):939-944.

52. Venook RD, Matter NI, Ramachandran M, et al. Prepolarized magnetic resonance imaging around metal orthopedic implants. *Magn Reson Med*. 2006;56(1):177-186. doi:10.1002/mrm.20927

53. Woods TO. Standards for medical devices in MRI: Present and future. *J Magn Reson Imaging*. 2007;26(5):1186-1189. doi:10.1002/jmri.21140

54. ASTM Committee F04 on Medical and Surgical Materials and Devices. *F2119-07(2013) Standard Test Method for Evaluation of MR Image Artifacts from Passive Implants*. ASTM International doi:10.1520/F2119-07R13

55. Olsrud J, Lätt J, Brockstedt S, Romner B, Björkman-Burtscher IM. Magnetic resonance imaging artifacts caused by aneurysm clips and shunt valves: Dependence on field strength (1.5 and 3 T) and imaging parameters. *J Magn Reson Imaging*. 2005;22(3):433-437. doi:10.1002/jmri.20391

56. Shellock FG, Cosendai G, Park SM, Nyenhuis JA. Implantable microstimulator: magnetic resonance safety at 1.5 Tesla. *Invest Radiol*. 2004;39(10):591-599. doi:10.1097/01.rli.0000138090.43450.ec

57. Shellock FG, Shellock VJ. Metallic stents: evaluation of MR imaging safety. *American Journal of Roentgenology*. 1999;173(3):543-547. doi:10.2214/ajr.173.3.10470877

58. Imai H, Tanaka Y, Nomura N, et al. Three-dimensional quantification of susceptibility artifacts from various metals in magnetic resonance images. *Acta Biomaterialia*. 2013;9(9):8433-8439. doi:10.1016/j.actbio.2013.05.017

59. Spronk T, Kraff O, Kreutner J, Schaefers G, Quick HH. Development and evaluation of a numerical simulation approach to predict metal artifacts from passive implants in MRI. *Magn Reson Mater Phy*. 2022;35(3):485-497. doi:10.1007/s10334-021-00966-5

60. Choi JW, Roh HG, Moon WJ, Chun YI, Kang CH. Optimization of MR Parameters of 3D TOF-MRA for Various Intracranial Stents at 3.0T MRI. *Neurointervention*. 2011;6(2):71. doi:10.5469/neuroint.2011.6.2.71

61. Bartels LW, Smits HFM, Bakker CJG, Viergever MA. MR Imaging of Vascular Stents: Effects of Susceptibility, Flow, and Radiofrequency Eddy Currents. *Journal of Vascular and Interventional Radiology*. 2001;12(3):365-371. doi:10.1016/S1051-0443(07)61918-6

62. Kato H, Ootani N, Abiru K, Okahara M. Investigating Signal Loss due to a Carotid Artery Stent in 3D-TOF-MRA. *MRMS*. 2021;20(3):303-311. doi:10.2463/mrms.mp.2019-0083

63. Shellock R & D Services, Inc. *Silk Artery Reconstruction Device Status*.; 2023. https://www.mrisafety.com/TMDL_view.php?editid1=5612

64. HyperSoft™ 3D & HyperSoft™ Helical | MicroVention. Accessed September 17, 2023. https://www.microvention.com/products/hypersoft-family/additional-information/mri-safety-information

65. Zheng LW, Wang JY, Qing Yu R. Biomaterials in Dentistry. In: *Encyclopedia of Biomedical Engineering*. Elsevier; 2019:278-288. doi:10.1016/B978-0-12-801238-3.11033-5

66. Nofiele JT, Cheng HLM. Ultrashort Echo Time for Improved Positive-Contrast Manganese-Enhanced MRI of Cancer. Bathen TF, ed. *PLoS ONE*. 2013;8(3):e58617. doi:10.1371/journal.pone.0058617

67. Bojorquez JZ, Bricq S, Acquitter C, Brunotte F, Walker PM, Lalande A. What are normal relaxation times of tissues at 3 T? *Magnetic Resonance Imaging*. 2017;35:69-80. doi:10.1016/j.mri.2016.08.021

68. Kurmis AP, Barber C, Slavotinek JP, Fazzalari NL. A MnCl2-based MR signal intensity linear response phantom. *Radiol Technol*. 2007;79(2):119-125.

69. Li L. Magnetic susceptibility quantification for arbitrarily shaped objects in inhomogeneous fields. *Magnetic Resonance in Med*. 2001;46(5):907-916. doi:10.1002/mrm.1276

70. Halefoglu AM, Yousem DM. Susceptibility weighted imaging: Clinical applications and future directions. *World J Radiol*. 2018;10(4):30-45. doi:10.4329/wjr.v10.i4.30

71. Sheth S, Branstetter BF, Escott EJ. Appearance of Normal Cranial Nerves on Steady-State Free Precession MR Images. *RadioGraphics*. 2009;29(4):1045-1055. doi:10.1148/rg.294085743

72. Hargreaves B. Rapid gradient-echo imaging. *Magnetic Resonance Imaging*. 2012;36(6):1300-1313. doi:10.1002/jmri.23742

73. Scheffler K, Lehnhardt S. Principles and applications of balanced SSFP techniques. *Eur Radiol*. 2003;13(11):2409-2418. doi:10.1007/s00330-003-1957-x

74. Bieri O, Scheffler K. Fundamentals of balanced steady state free precession MRI: Fundamentals of Balanced SSFP MRI. *J Magn Reson Imaging*. 2013;38(1):2-11. doi:10.1002/jmri.24163

75. Casselman JW, Kuhweide R, Deimling M, Ampe W, Dehaene I, Meeus L. Constructive interference in steady state-3DFT MR imaging of the inner ear and cerebellopontine angle. *AJNR Am J Neuroradiol*. 1993;14(1):47-57.

76. Baliyan V, Das CJ, Sharma R, Gupta AK. Diffusion weighted imaging: Technique and applications. *WJR*. 2016;8(9):785. doi:10.4329/wjr.v8.i9.785

77. Koch KM, Bhave S, Gaddipati A, et al. Multispectral diffusion-weighted imaging near metal implants. *Magnetic Resonance in Med*. 2018;79(2):987-993. doi:10.1002/mrm.26737

78. Melhem ER, Israel DA, Eustace S, Jara H. MR of the spine with a fast T1-weighted fluid-attenuated inversion recovery sequence. *AJNR Am J Neuroradiol*. 1997;18(3):447-454.

79. Forbes KPN, Pipe JG, Bird CR, Heiserman JE. PROPELLER MRI: Clinical testing of a novel technique for quantification and compensation of head motion. *Magnetic Resonance Imaging*. 2001;14(3):215-222. doi:10.1002/jmri.1176

80. Lavdas E, Mavroidis P, Kostopoulos S, et al. Improvement of image quality using BLADE sequences in brain MR imaging. *Magnetic Resonance Imaging*. 2013;31(2):189-200. doi:10.1016/j.mri.2012.08.001

81. Willinek WA, Born M, Simon B, et al. Time-of-Flight MR Angiography: Comparison of 3.0-T Imaging and 1.5-T Imaging—Initial Experience. *Radiology*. 2003;229(3):913-920. doi:10.1148/radiol.2293020782

82. Tang H, Hu N, Yuan Y, et al. Accelerated Time-of-Flight Magnetic Resonance Angiography with Sparse Undersampling and Iterative Reconstruction for the Evaluation of Intracranial Arteries. *Korean J Radiol*. 2019;20(2):265. doi:10.3348/kjr.2017.0634

83. MathWorks. Image Processing Toolbox. Published online 2021. https://www.mathworks.com/products/image.html

84. Pratt V. Direct least-squares fitting of algebraic surfaces. *SIGGRAPH Comput Graph*. 1987;21(4):145-152. doi:10.1145/37402.37420

85. Nikolai Chernov. Nikolai Chernov (2022). Circle Fit (Pratt method) (https://www.mathworks.com/matlabcentral/fileexchange/22643-circle-fit-pratt-method), MATLAB Central File Exchange. Retrieved January 5, 2022. Published online January 10, 2009. Nikolai Chernov (2022). Circle Fit (Pratt method) (https://www.mathworks.com/matlabcentral/fileexchange/22643-circle-fit-pratt-method), MATLAB Central File Exchange. Retrieved January 5, 2022.

86. Schindelin J, Arganda-Carreras I, Frise E, et al. Fiji: an open-source platform for biological-image analysis. *Nat Methods*. 2012;9(7):676-682. doi:10.1038/nmeth.2019

87. Owusu N, Magnotta VA. Factors influencing daily quality assurance measurements of magnetic resonance imaging scanners. *Radiol Phys Technol*. 2021;14(4):396-401. doi:10.1007/s12194-021-00638-y

88. Benjamini Y, Hochberg Y. Controlling the False Discovery Rate: A Practical and Powerful Approach to Multiple Testing. *Journal of the Royal Statistical Society: Series B (Methodological)*. 1995;57(1):289-300. doi:10.1111/j.2517-6161.1995.tb02031.x

89. Lee S, Lee DK. What is the proper way to apply the multiple comparison test? *Korean J Anesthesiol*. 2018;71(5):353-360. doi:10.4097/kja.d.18.00242

90. GraphPad Software. GraphPad Prism version 10.1.1 for Windows. www.graphpad.com

91. Lee EM, Ibrahim ESH, Dudek N, et al. Improving MR Image Quality in Patients with Metallic Implants. *RadioGraphics*. 2021;41(4):E126-E137. doi:10.1148/rg.2021200092

92. Port JD, Pomper MG. Quantification and Minimization of Magnetic Susceptibility Artifacts on GRE Images: *Journal of Computer Assisted Tomography*. 2000;24(6):958-964. doi:10.1097/00004728-200011000-00024

93. Heinrich A, Güttler FV, Schlesies F, Aschenbach R, Eckardt N, Teichgräber UKM. In vitro stent assessment by MRI: visibility of lumen and artifacts for 27 modern stents. *Biomedical Engineering / Biomedizinische Technik*. 2017;62(6):565-573. doi:10.1515/bmt-2016-0008

94. Shellock FG, Gounis M, Wakhloo A. Detachable Coil for Cerebral Aneurysms: In Vitro Evaluation of Magnetic Field Interactions, Heating, and Artifacts at 3T. Published online 2005.

95. Celik A. Effect of imaging parameters on the accuracy of apparent diffusion coefficient and optimization strategies. *Diagn Interv Radiol*. 2015;22(1):101-107. doi:10.5152/dir.2015.14440

96. Dietrich TJ, Ulbrich EJ, Zanetti M, Fucentese SF, Pfirrmann CWA. PROPELLER Technique to Improve Image Quality of MRI of the Shoulder. *American Journal of Roentgenology*. 2011;197(6):W1093-W1100. doi:10.2214/AJR.10.6065

97. Bouillot P, Brina O, Delattre BMA, et al. Neurovascular stent artifacts in 3D-TOF and 3D-PCMRI: Influence of stent design on flow measurement. *Magnetic Resonance in Med*. 2019;81(1):560-572. doi:10.1002/mrm.27352

98. Gruber B, Froeling M, Leiner T, Klomp DWJ. RF coils: A practical guide for nonphysicists. *Magnetic Resonance Imaging*. 2018;48(3):590-604. doi:10.1002/jmri.26187

99. Riad SM, Salama IM. *Electromagnetic Fields and Waves: Fundamentals of Engineering*. McGraw Hill; 2020.

100. Fruehwald-Pallamar J, Fruehwald F, Holzer-Fruehwald L, Nolz R, Stoiber C, Sprinzl GM. Magnetic Resonance Imaging with Active Implantable Hearing Devices: Reports from the Daily Radiological Routine in an Outpatient MR Center. *JPM*. 2023;13(8):1220. doi:10.3390/jpm13081220

## Appendix A: Phantom Construction Methods

Imaging phantoms are assembled in the following stepwise fashion:

1. A hole is drilled in the upper hemisphere of the spherical container to allow for the addition of gelatine at a later step.

2. The device is secure near the center of the PETG ring with a thin nylon string.

3. The PETG ring-device assembly is inserted into the lower hemisphere of the container.

4. The spherical container is closed and sealed with a high-quality silyl-modified polymeric adhesive. The sealant must be allowed to cure at room temperature in a well-ventilated area for at least 24 hours before continuing.

5. Gelatine solution is prepared by first heating distilled water to approximately 50 degrees Celsius (°C)

6. Dry collagen-based gelatine (Knox Gelatine) is mixed into the water to a final concentration of 2.5 weight-percent. The solution must be mixed until the gelatine is fully dissolved.

7. The gelatine solution is further heated to approximately 90 °C, when manganese chloride tetrahydride solution is added to a final concentration of 0.1 millimolar.

8. The gelatine solution is further heated until the boiling point to fully degasify the solution before removing from the heat source.

9. The phantom is filled with the hot gelatine solution and allowed to cool at room temperature. Excess gelatine solution is stored in an insulated container and pipetted into the phantom every 20 minutes for four hours to account for temperature-driven volume.

10. The top hole of the phantom is sealed with thick flexible tape before being stored in a refrigerated set to approximately 4 °C for at least 12 hours to allow the gelatine solution to set.

11. The phantom is stored in a refrigerator when not in use and has a shelf-life of approximately 30 days. Before imaging, the phantom is allowed to acclimatize to room temperature.

# Appendix B: Supplementary Data Summary Tables

Table B.1 Artifact width measurement summary for staple in parallel orientation

| Trial number | B₀ | Artifact width (mm) | | | | | | |
|---|---|---|---|---|---|---|---|---|
| | | bSSFP | DWI | T1 FLAIR | T2WI | T2 FLAIR | TOF-MRA | TRM bSSFP |
| 1 | 0.5 T | 6.63 | 12.85 | 3.24 | 3.63 | 1.92 | 6.17 | 6.63 |
| 2 | 0.5 T | 7.23 | 10.04 | 4.41 | 3.39 | 2.17 | 5.98 | 7.23 |
| 3 | 0.5 T | 5.88 | 10.04 | 4.60 | 3.63 | 2.41 | 5.58 | 5.88 |
| Mean | - | 6.58 | 10.98 | 4.09 | 3.55 | 2.17 | 5.91 | 6.58 |
| SD | - | 0.68 | 1.62 | 0.74 | 0.14 | 0.24 | 0.30 | 0.68 |
| 1 | 1.5 T | 9.39 | 18.01 | 6.01 | 4.67 | 6.17 | 6.76 | 9.57 |
| 2 | 1.5 T | 9.22 | 17.07 | 6.01 | 4.88 | 5.31 | 6.85 | 9.75 |
| 3 | 1.5 T | 9.39 | 16.13 | 5.31 | 5.10 | 5.31 | 6.66 | 10.10 |
| Mean | - | 9.34 | 17.07 | 5.78 | 4.88 | 5.60 | 6.76 | 9.80 |
| SD | - | 0.10 | 0.94 | 0.41 | 0.21 | 0.50 | 0.10 | 0.27 |
| 1 | 3 T | 6.41 | 14.61 | 17.07 | 6.60 | 6.82 | 8.32 | 12.73 |
| 2 | 3 T | 5.00 | 13.48 | 15.20 | 6.82 | 6.82 | 8.32 | 12.91 |
| 3 | 3 T | 6.41 | 13.48 | 17.54 | 6.82 | 6.60 | 8.10 | 12.91 |
| Mean | - | 5.94 | 13.85 | 16.60 | 6.74 | 6.74 | 8.25 | 12.85 |
| SD | - | 0.81 | 0.65 | 1.24 | 0.12 | 0.12 | 0.12 | 0.10 |

Table B.2 Artifact width measurement summary for staple in perpendicular orientation

| Trial number | B₀ | Artifact width (mm) | | | | | | |
|---|---|---|---|---|---|---|---|---|
| | | bSSFP | DWI | T1 FLAIR | T2WI | T2 FLAIR | TOF-MRA | TRM bSSFP |
| 1 | 0.5 T | 7.15 | 8.16 | 4.88 | 3.24 | 1.53 | 5.97 | 7.15 |
| 2 | 0.5 T | 6.70 | 7.69 | 5.12 | 2.75 | 2.24 | 5.78 | 6.70 |
| 3 | 0.5 T | 5.50 | 8.12 | 2.77 | 3.24 | 0.78 | 5.47 | 5.50 |
| Mean | - | 6.45 | 7.99 | 4.26 | 3.07 | 1.52 | 5.74 | 6.45 |
| SD | - | 0.85 | 0.26 | 1.29 | 0.28 | 0.73 | 0.25 | 0.85 |
| 1 | 1.5 T | 8.57 | 16.56 | 6.52 | 4.35 | 4.56 | 6.25 | 9.10 |
| 2 | 1.5 T | 8.40 | 15.15 | 7.46 | 4.51 | 4.99 | 6.35 | 9.28 |
| 3 | 1.5 T | 8.57 | 15.62 | 7.46 | 4.35 | 4.99 | 6.25 | 8.75 |
| Mean | - | 8.52 | 15.78 | 7.15 | 4.40 | 4.85 | 6.28 | 9.04 |
| SD | - | 0.10 | 0.72 | 0.54 | 0.09 | 0.25 | 0.06 | 0.27 |
| 1 | 3 T | 6.64 | 17.62 | 12.85 | 6.87 | 6.87 | 7.09 | 11.91 |
| 2 | 3 T | 5.01 | 12.46 | 11.87 | 6.66 | 6.87 | 6.93 | 12.09 |
| 3 | 3 T | 5.01 | 11.87 | 12.81 | 6.87 | 6.44 | 6.93 | 11.74 |
| Mean | - | 5.56 | 13.98 | 12.51 | 6.80 | 6.73 | 6.98 | 11.91 |
| SD | - | 0.94 | 3.16 | 0.55 | 0.12 | 0.25 | 0.09 | 0.18 |

Table B.3 Artifact width measurement summary for stent in parallel orientation

| Trial number | $B_0$ | Artifact width (mm) | | | | | | |
|---|---|---|---|---|---|---|---|---|
| | | bSSFP | DWI | T1 FLAIR | T2WI | T2 FLAIR | TOF-MRA | TRM bSSFP |
| 1 | 0.5 T | 0.60 | 0.00 | 0.00 | 0.00 | 0.00 | 0.98 | 0.60 |
| 2 | 0.5 T | 0.60 | 0.00 | 0.00 | 0.00 | 0.00 | 0.59 | 0.60 |
| 3 | 0.5 T | 0.75 | 0.00 | 0.00 | 0.00 | 0.00 | 0.98 | 0.75 |
| Mean | - | 0.65 | 0.00 | 0.00 | 0.00 | 0.00 | 0.85 | 0.65 |
| SD | - | 0.09 | 0.00 | 0.00 | 0.00 | 0.00 | 0.23 | 0.09 |
| 1 | 1.5 T | 0.86 | 0.86 | 0.00 | 0.00 | 0.00 | 0.69 | 1.04 |
| 2 | 1.5 T | 1.04 | 1.33 | 0.00 | 0.00 | 0.00 | 0.69 | 0.86 |
| 3 | 1.5 T | 0.86 | 0.86 | 0.00 | 0.00 | 0.00 | 0.69 | 0.86 |
| Mean | - | 0.92 | 1.02 | 0.00 | 0.00 | 0.00 | 0.69 | 0.92 |
| SD | - | 0.10 | 0.27 | 0.00 | 0.00 | 0.00 | 0.00 | 0.10 |
| 1 | 3 T | 1.04 | 1.06 | 2.27 | 0.41 | 0.41 | 1.06 | 1.04 |
| 2 | 3 T | 1.21 | 2.30 | 1.80 | 0.41 | 0.20 | 1.06 | 0.86 |
| 3 | 3 T | 1.21 | 0.00 | 2.03 | 0.41 | 0.41 | 1.27 | 1.04 |
| Mean | - | 1.16 | 1.12 | 2.03 | 0.41 | 0.34 | 1.13 | 0.98 |
| SD | - | 0.10 | 1.15 | 0.23 | 0.00 | 0.12 | 0.12 | 0.10 |

Table B.4: Artifact width measurement summary for stent in perpendicular orientation

| Trial number | $B_0$ | Artifact width (mm) | | | | | | |
|---|---|---|---|---|---|---|---|---|
| | | bSSFP | DWI | T1 FLAIR | T2WI | T2 FLAIR | TOF-MRA | TRM bSSFP |
| 1 | 0.5 T | 0.15 | 0.86 | 0.00 | 0.00 | 0.00 | 0.59 | 0.15 |
| 2 | 0.5 T | 0.00 | 0.00 | 0.00 | 0.00 | 0.00 | 0.27 | 0.00 |
| 3 | 0.5 T | 0.60 | 0.00 | 0.00 | 0.00 | 0.00 | 0.27 | 0.60 |
| Mean | - | 0.25 | 0.29 | 0.00 | 0.00 | 0.00 | 0.38 | 0.25 |
| SD | - | 0.31 | 0.50 | 0.00 | 0.00 | 0.00 | 0.18 | 0.31 |
| 1 | 1.5 T | 0.51 | 2.74 | 0.16 | 0.00 | 0.00 | 0.30 | 0.69 |
| 2 | 1.5 T | 0.51 | 2.74 | 0.39 | 0.00 | 0.00 | 0.39 | 0.69 |
| 3 | 1.5 T | 0.51 | 4.14 | 0.16 | 0.00 | 0.00 | 0.30 | 0.69 |
| Mean | - | 0.51 | 3.21 | 0.24 | 0.00 | 0.00 | 0.33 | 0.69 |
| SD | - | 0.00 | 0.81 | 0.14 | 0.00 | 0.00 | 0.06 | 0.00 |
| 1 | 3 T | 0.86 | 3.64 | 0.86 | 0.00 | 0.41 | 0.84 | 1.74 |
| 2 | 3 T | 0.86 | 3.64 | 0.63 | 0.00 | 0.00 | 0.84 | 1.74 |
| 3 | 3 T | 0.86 | 3.64 | 0.86 | 0.00 | 0.00 | 0.84 | 1.74 |
| Mean | - | 0.86 | 3.64 | 0.78 | 0.00 | 0.14 | 0.84 | 1.74 |
| SD | - | 0.00 | 0.00 | 0.14 | 0.00 | 0.24 | 0.00 | 0.00 |

Table B.5: Artifact width measurement summary for endovascular coil in perpendicular orientation

| Trial number | B₀ | Artifact width (mm) | | | | | | |
|---|---|---|---|---|---|---|---|---|
| | | bSSFP | DWI | T1 FLAIR | T2WI | T2 FLAIR | TOF-MRA | TRM bSSFP |
| 1 | 0.5 T | 0.00 | 0.00 | 0.00 | 0.00 | 0.00 | 0.17 | 0.00 |
| 2 | 0.5 T | 0.00 | 0.00 | 0.00 | 0.00 | 0.00 | 0.17 | 0.00 |
| 3 | 0.5 T | 0.00 | 0.00 | 0.00 | 0.00 | 0.00 | 0.36 | 0.00 |
| Mean | - | 0.00 | 0.00 | 0.00 | 0.00 | 0.00 | 0.23 | 0.00 |
| SD | - | 0.00 | 0.00 | 0.00 | 0.00 | 0.00 | 0.11 | 0.00 |
| 1 | 1.5 T | 0.34 | 0.00 | 0.00 | 0.00 | 0.00 | 0.17 | 0.52 |
| 2 | 1.5 T | 0.34 | 0.00 | 0.00 | 0.00 | 0.00 | 0.17 | 0.34 |
| 3 | 1.5 T | 0.34 | 0.40 | 0.00 | 0.00 | 0.00 | 0.17 | 0.34 |
| Mean | - | 0.34 | 0.13 | 0.00 | 0.00 | 0.00 | 0.17 | 0.40 |
| SD | - | 0.00 | 0.23 | 0.00 | 0.00 | 0.00 | 0.00 | 0.10 |
| 1 | 3 T | 0.52 | 0.95 | 0.00 | 0.00 | 0.00 | 0.52 | 0.87 |
| 2 | 3 T | 0.52 | 0.95 | 0.00 | 0.00 | 0.00 | 0.52 | 0.87 |
| 3 | 3 T | 0.69 | 0.09 | 0.00 | 0.00 | 0.00 | 0.52 | 0.87 |
| Mean | - | 0.58 | 0.66 | 0.00 | 0.00 | 0.00 | 0.52 | 0.87 |
| SD | - | 0.10 | 0.50 | 0.00 | 0.00 | 0.00 | 0.00 | 0.00 |

Table B.6 TRM bSSFP field distortion model summary for parallel staple

| Trial number | B0 | SI direction | | LR direction | | AP direction | |
|---|---|---|---|---|---|---|---|
| | | Band-band | Device-band | Band-band | Device-band | Band-band | Device-band |
| 1 | 0.5 T | 17.90 | 5.35 | 13.20 | 4.45 | 11.40 | 5.43 |
| 2 | 0.5 T | 17.60 | 5.20 | 13.80 | 4.75 | 12.00 | 5.73 |
| 3 | 0.5 T | 18.20 | 5.50 | 12.60 | 4.15 | 9.90 | 4.68 |
| Mean | 0.5 T | 17.90 | 5.35 | 13.20 | 4.45 | 11.10 | 5.28 |
| SD | 0.5 T | 0.30 | 0.15 | 0.60 | 0.30 | 1.08 | 0.54 |
| 1 | 1.5 T | 27.00 | 9.90 | 17.90 | 6.80 | 17.20 | 8.33 |
| 2 | 1.5 T | 27.30 | 10.05 | 17.90 | 6.80 | 17.20 | 8.33 |
| 3 | 1.5 T | 27.00 | 9.90 | 17.90 | 6.80 | 17.50 | 8.48 |
| Mean | 1.5 T | 27.10 | 9.95 | 17.90 | 6.80 | 17.30 | 8.38 |
| SD | 1.5 T | 0.17 | 0.09 | 0.00 | 0.00 | 0.17 | 0.09 |
| 1 | 3 T | 34.20 | 13.50 | 23.20 | 9.45 | 22.50 | 10.98 |
| 2 | 3 T | 34.20 | 13.50 | 23.60 | 9.65 | 22.80 | 11.13 |
| 3 | 3 T | 34.20 | 13.50 | 23.60 | 9.65 | 22.50 | 10.98 |
| Mean | 3 T | 34.20 | 13.50 | 23.47 | 9.58 | 22.60 | 11.03 |
| SD | 3 T | 0.00 | 0.00 | 0.23 | 0.12 | 0.17 | 0.09 |

Note: All measurements provided in mm.

Table B.7 TRM bSSFP field distortion model summary for perpendicular staple

| Trial number | $B_0$ | SI direction | | LR direction | | AP direction | |
| --- | --- | --- | --- | --- | --- | --- | --- |
| | | Band-band | Device-band | Band-band | Device-band | Band-band | Device-band |
| 1 | 0.5 T | 13.50 | 6.48 | 15.00 | 5.35 | 17.70 | 5.25 |
| 2 | 0.5 T | 13.50 | 6.48 | 14.40 | 5.05 | 17.40 | 5.10 |
| 3 | 0.5 T | 14.90 | 7.18 | 13.80 | 4.75 | 16.50 | 4.65 |
| Mean | 0.5 T | 13.97 | 6.71 | 14.40 | 5.05 | 17.20 | 5.00 |
| SD | 0.5 T | 0.81 | 0.40 | 0.60 | 0.30 | 0.62 | 0.31 |
| 1 | 1.5 T | 24.90 | 12.18 | 19.30 | 7.50 | 21.80 | 7.30 |
| 2 | 1.5 T | 24.60 | 12.03 | 19.60 | 7.65 | 21.50 | 7.15 |
| 3 | 1.5 T | 24.60 | 12.03 | 19.60 | 7.65 | 21.80 | 7.30 |
| Mean | 1.5 T | 24.70 | 12.08 | 19.50 | 7.60 | 21.70 | 7.25 |
| SD | 1.5 T | 0.17 | 0.09 | 0.17 | 0.09 | 0.17 | 0.09 |
| 1 | 3 T | 31.80 | 15.63 | 24.30 | 10.00 | 27.00 | 9.90 |
| 2 | 3 T | 31.80 | 15.63 | 24.30 | 10.00 | 27.00 | 9.90 |
| 3 | 3 T | 32.40 | 15.93 | 24.30 | 10.00 | 26.30 | 9.55 |
| Mean | 3 T | 32.00 | 15.73 | 24.30 | 10.00 | 26.77 | 9.78 |
| SD | 3 T | 0.35 | 0.17 | 0.00 | 0.00 | 0.40 | 0.20 |

Note: All measurements provided in mm.

Table B.8 RF shielding assessment summary for parallel stent

| Trial number | $B_0$ | Lumen signal intensity | Background signal intensity | Relative in-stent signal |
|---|---|---|---|---|
| 1 | 0.5 T | 8156 | 7915 | 103% |
| 2 | 0.5 T | 8669 | 8382 | 103% |
| 3 | 0.5 T | 8275 | 7974 | 104% |
| Mean | 0.5 T | 8367 | 8090 | 103% |
| SD | 0.5 T | 268 | 254 | 0% |
| 1 | 1.5 T | 368 | 361 | 102% |
| 2 | 1.5 T | 366 | 355 | 103% |
| 3 | 1.5 T | 344 | 340 | 101% |
| Mean | 1.5 T | 359 | 352 | 102% |
| SD | 1.5 T | 13 | 11 | 1% |
| 1 | 3 T | 745 | 746 | 100% |
| 2 | 3 T | 803 | 793 | 101% |
| 3 | 3 T | 649 | 622 | 104% |
| Mean | 3 T | 732 | 720 | 102% |
| SD | 3 T | 78 | 89 | 2% |

Table B.9 RF shielding assessment summary for perpendicular stent

| Trial number | $B_0$ | Lumen signal intensity | Background signal intensity | Relative in-stent signal |
|---|---|---|---|---|
| 1 | 0.5 T | 7480 | 7365 | 102% |
| 2 | 0.5 T | 7162 | 6892 | 104% |
| 3 | 0.5 T | 6241 | 6064 | 103% |
| Mean | 0.5 T | 6961 | 6773 | 103% |
| SD | 0.5 T | 644 | 658 | 1% |
| 1 | 1.5 T | 272 | 325 | 84% |
| 2 | 1.5 T | 267 | 320 | 84% |
| 3 | 1.5 T | 262 | 309 | 85% |
| Mean | 1.5 T | 267 | 318 | 84% |
| SD | 1.5 T | 5 | 8 | 1% |
| 1 | 3 T | 505 | 718 | 70% |
| 2 | 3 T | 525 | 704 | 75% |
| 3 | 3 T | 504 | 715 | 70% |
| Mean | 3 T | 511 | 712 | 72% |
| SD | 3 T | 12 | 7 | 2% |

# Appendix C: Statistical Testing Summary Tables

Table C.1 Two-factor ANOVA summary for staple in parallel orientation

| Pulse sequence | Comparison | P value | q value | Significant? |
|---|---|---|---|---|
| bSSFP | 0.5 T vs. 1.5 T | <0.0001 | <0.0001 | Yes |
| | 0.5 T vs. 3 T | 0.2213 | 0.2213 | No |
| | 1.5 T vs. 3 T | <0.0001 | <0.0001 | Yes |
| TRM bSSFP | 0.5 T vs. 1.5 T | <0.0001 | <0.0001 | Yes |
| | 0.5 T vs. 3 T | <0.0001 | <0.0001 | Yes |
| | 1.5 T vs. 3 T | <0.0001 | <0.0001 | Yes |
| DWI | 0.5 T vs. 1.5 T | <0.0001 | <0.0001 | Yes |
| | 0.5 T vs. 3 T | <0.0001 | <0.0001 | Yes |
| | 1.5 T vs. 3 T | <0.0001 | <0.0001 | Yes |
| T1 FLAIR | 0.5 T vs. 1.5 T | 0.0021 | 0.0021 | Yes |
| | 0.5 T vs. 3 T | <0.0001 | <0.0001 | Yes |
| | 1.5 T vs. 3 T | <0.0001 | <0.0001 | Yes |
| T2WI | 0.5 T vs. 1.5 T | 0.0132 | 0.0132 | Yes |
| | 0.5 T vs. 3 T | <0.0001 | <0.0001 | Yes |
| | 1.5 T vs. 3 T | 0.0008 | 0.0012 | Yes |
| T2 FLAIR | 0.5 T vs. 1.5 T | <0.0001 | <0.0001 | Yes |
| | 0.5 T vs. 3 T | <0.0001 | <0.0001 | Yes |
| | 1.5 T vs. 3 T | 0.0311 | 0.0311 | Yes |
| TOF-MRA | 0.5 T vs. 1.5 T | 0.1080 | 0.1080 | No |
| | 0.5 T vs. 3 T | <0.0001 | 0.0001 | Yes |
| | 1.5 T vs. 3 T | 0.0061 | 0.0091 | Yes |

Table C.2 Two-factor ANOVA summary for staple in perpendicular orientation

| Pulse sequence | Comparison | P value | q value | Significant? |
|---|---|---|---|---|
| bSSFP | 0.5 T vs. 1.5 T | 0.0062 | 0.0093 | Yes |
| | 0.5 T vs. 3 T | 0.2174 | 0.2174 | No |
| | 1.5 T vs. 3 T | 0.0002 | 0.0005 | Yes |
| TRM bSSFP | 0.5 T vs. 1.5 T | 0.0008 | 0.0008 | Yes |
| | 0.5 T vs. 3 T | <0.0001 | <0.0001 | Yes |
| | 1.5 T vs. 3 T | 0.0002 | 0.0004 | Yes |
| DWI | 0.5 T vs. 1.5 T | <0.0001 | <0.0001 | Yes |
| | 0.5 T vs. 3 T | <0.0001 | <0.0001 | Yes |
| | 1.5 T vs. 3 T | 0.0162 | 0.0162 | Yes |
| T1 FLAIR | 0.5 T vs. 1.5 T | 0.0002 | 0.0002 | Yes |
| | 0.5 T vs. 3 T | <0.0001 | <0.0001 | Yes |
| | 1.5 T vs. 3 T | <0.0001 | <0.0001 | Yes |
| T2WI | 0.5 T vs. 1.5 T | 0.0710 | 0.0710 | No |
| | 0.5 T vs. 3 T | <0.0001 | <0.0001 | Yes |
| | 1.5 T vs. 3 T | 0.0017 | 0.0026 | Yes |
| T2 FLAIR | 0.5 T vs. 1.5 T | <0.0001 | <0.0001 | Yes |
| | 0.5 T vs. 3 T | <0.0001 | <0.0001 | Yes |
| | 1.5 T vs. 3 T | 0.0120 | 0.0120 | Yes |
| TOF-MRA | 0.5 T vs. 1.5 T | 0.4522 | 0.4522 | No |
| | 0.5 T vs. 3 T | 0.0898 | 0.2695 | No |
| | 1.5 T vs. 3 T | 0.3339 | 0.4522 | No |

Table C.3 One-factor ANOVA summary for staple orientation comparison

| Field strength | Comparison | P value | q value | Significant? |
|---|---|---|---|---|
| 0.5 T | Parallel vs. Perpendicular | 0.5598 | 0.7361 | No |
| 1.5 T | Parallel vs Perpendicular | 0.7361 | 0.7361 | No |
| 3 T | Parallel vs. Perpendicular | 0.4425 | 0.7361 | No |

Table C.4 Two-factor ANOVA summary for stent in parallel orientation

| Pulse sequence | Comparison | P value | q value | Significant? |
|---|---|---|---|---|
| bSSFP | 0.5 T vs. 1.5 T | 0.2334 | 0.3023 | No |
|  | 0.5 T vs. 3 T | 0.0295 | 0.0886 | No |
|  | 1.5 T vs. 3 T | 0.3023 | 0.3023 | No |
| TRM bSSFP | 0.5 T vs. 1.5 T | 0.2334 | 0.3501 | No |
|  | 0.5 T vs. 3 T | 0.1490 | 0.3501 | No |
|  | 1.5 T vs. 3 T | 0.7953 | 0.7953 | No |
| DWI | 0.5 T vs. 1.5 T | <0.0001 | <0.0001 | Yes |
|  | 0.5 T vs. 3 T | <0.0001 | <0.0001 | Yes |
|  | 1.5 T vs. 3 T | 0.6603 | 0.6603 | No |
| T1 FLAIR | 0.5 T vs. 1.5 T | >0.9999 | >0.9999 | No |
|  | 0.5 T vs. 3 T | <0.0001 | <0.0001 | Yes |
|  | 1.5 T vs. 3 T | <0.0001 | <0.0001 | Yes |
| T2WI | 0.5 T vs. 1.5 T | >0.9999 | >0.9999 | No |
|  | 0.5 T vs. 3 T | 0.0726 | 0.1089 | No |
|  | 1.5 T vs. 3 T | 0.0726 | 0.1089 | No |
| T2 FLAIR | 0.5 T vs. 1.5 T | >0.9999 | >0.9999 | No |
|  | 0.5 T vs. 3 T | 0.1354 | 0.2031 | No |
|  | 1.5 T vs. 3 T | 0.1354 | 0.2031 | No |
| TOF-MRA | 0.5 T vs. 1.5 T | 0.4720 | 0.4720 | No |
|  | 0.5 T vs. 3 T | 0.2191 | 0.3287 | No |
|  | 1.5 T vs. 3 T | 0.0551 | 0.1652 | No |

Table C.5 One-factor ANOVA summary for stent orientation comparison

| Field strength | Comparison | P value | q value | Significant? |
|---|---|---|---|---|
| 0.5 T | Parallel vs. Perpendicular | 0.7179 | 0.9672 | No |
| 1.5 T | Parallel vs. Perpendicular | 0.3084 | 0.9251 | No |
| 3 T | Parallel vs. Perpendicular | 0.9672 | 0.9672 | No |

Table C.6 Two-factor ANOVA summary for stent in perpendicular orientation

| Pulse sequence | Comparison | P value | q value | Significant? |
|---|---|---|---|---|
| bSSFP | 0.5 T vs. 1.5 T | 0.1941 | 0.1941 | No |
| | 0.5 T vs. 3 T | 0.0035 | 0.0105 | Yes |
| | 1.5 T vs. 3 T | 0.0829 | 0.1244 | No |
| TRM bSSFP | 0.5 T vs. 1.5 T | 0.0309 | 0.0309 | Yes |
| | 0.5 T vs. 3 T | <0.0001 | <0.0001 | Yes |
| | 1.5 T vs. 3 T | <0.0001 | <0.0001 | Yes |
| DWI | 0.5 T vs. 1.5 T | <0.0001 | <0.0001 | Yes |
| | 0.5 T vs. 3 T | <0.0001 | <0.0001 | Yes |
| | 1.5 T vs. 3 T | 0.0334 | 0.0334 | Yes |
| T1 FLAIR | 0.5 T vs. 1.5 T | 0.2364 | 0.2364 | No |
| | 0.5 T vs. 3 T | 0.0003 | 0.0008 | Yes |
| | 1.5 T vs. 3 T | 0.0082 | 0.0123 | Yes |
| T2WI | 0.5 T vs. 1.5 T | >0.9999 | >0.9999 | No |
| | 0.5 T vs. 3 T | >0.9999 | >0.9999 | No |
| | 1.5 T vs. 3 T | >0.9999 | >0.9999 | No |
| T2 FLAIR | 0.5 T vs. 1.5 T | >0.9999 | >0.9999 | No |
| | 0.5 T vs. 3 T | 0.4918 | 0.7376 | No |
| | 1.5 T vs. 3 T | 0.4918 | 0.7376 | No |
| TOF-MRA | 0.5 T vs. 1.5 T | 0.8139 | 0.8139 | No |
| | 0.5 T vs. 3 T | 0.0235 | 0.0352 | Yes |
| | 1.5 T vs. 3 T | 0.0132 | 0.0352 | Yes |

Table C.7 Two-factor ANOVA summary for endovascular coil in perpendicular orientation

| Pulse sequence | Comparison | P value | q value | Significant? |
|---|---|---|---|---|
| bSSFP | 0.5 T vs. 1.5 T | 0.0019 | 0.0029 | Yes |
| | 0.5 T vs. 3 T | <0.0001 | <0.0001 | Yes |
| | 1.5 T vs. 3 T | 0.0262 | 0.0262 | Yes |
| TRM bSSFP | 0.5 T vs. 1.5 T | 0.0003 | 0.0003 | Yes |
| | 0.5 T vs. 3 T | <0.0001 | <0.0001 | Yes |
| | 1.5 T vs. 3 T | <0.0001 | <0.0001 | Yes |
| DWI | 0.5 T vs. 1.5 T | 0.2011 | 0.2011 | No |
| | 0.5 T vs. 3 T | <0.0001 | <0.0001 | Yes |
| | 1.5 T vs. 3 T | <0.0001 | <0.0001 | Yes |
| T1 FLAIR | 0.5 T vs. 1.5 T | >0.9999 | >0.9999 | No |
| | 0.5 T vs. 3 T | >0.9999 | >0.9999 | No |
| | 1.5 T vs. 3 T | >0.9999 | >0.9999 | No |
| T2WI | 0.5 T vs. 1.5 T | >0.9999 | >0.9999 | No |
| | 0.5 T vs. 3 T | >0.9999 | >0.9999 | No |
| | 1.5 T vs. 3 T | >0.9999 | >0.9999 | No |
| T2 FLAIR | 0.5 T vs. 1.5 T | >0.9999 | >0.9999 | No |
| | 0.5 T vs. 3 T | >0.9999 | >0.9999 | No |
| | 1.5 T vs. 3 T | >0.9999 | >0.9999 | No |
| TOF-MRA | 0.5 T vs. 1.5 T | 0.5406 | 0.5406 | No |
| | 0.5 T vs. 3 T | 0.0078 | 0.0118 | Yes |
| | 1.5 T vs. 3 T | 0.0014 | 0.0043 | Yes |

Table C.8 Two-factor ANOVA summary for TRM bSSFP field distortion model

| Field strength and orientation | Comparison | P value | q value | Significant? |
|---|---|---|---|---|
| 0.5 T Parallel | LR vs. AP | <0.0001 | <0.0001 | Yes |
| | LR vs. SI | <0.0001 | <0.0001 | Yes |
| | AP vs. SI | 0.6811 | 0.6811 | No |
| 0.5 T Perpendicular | LR vs. AP | 0.7840 | 0.7840 | No |
| | LR vs. SI | <0.0001 | <0.0001 | Yes |
| | AP vs. SI | <0.0001 | <0.0001 | Yes |
| 1.5 T Parallel | LR vs. AP | <0.0001 | <0.0001 | Yes |
| | LR vs. SI | <0.0001 | <0.0001 | Yes |
| | AP vs. SI | <0.0001 | <0.0001 | Yes |
| 1.5 T Perpendicular | LR vs. AP | 0.0611 | 0.0611 | No |
| | LR vs. SI | <0.0001 | <0.0001 | Yes |
| | AP vs. SI | <0.0001 | <0.0001 | Yes |
| 3 T Parallel | LR vs. AP | <0.0001 | <0.0001 | Yes |
| | LR vs. SI | <0.0001 | <0.0001 | Yes |
| | AP vs. SI | <0.0001 | <0.0001 | Yes |
| 3 T Perpendicular | LR vs. AP | 0.2392 | 0.2392 | No |
| | LR vs. SI | <0.0001 | <0.0001 | Yes |
| | AP vs. SI | <0.0001 | <0.0001 | Yes |

Table C.9 Two-factor ANOVA summary for RF shielding assessment

| Orientation | Comparison | P value | q value | Significant? |
|---|---|---|---|---|
| Perpendicular | 0.5 T vs. 1.5 T | <0.0001 | <0.0001 | Yes |
| | 0.5 T vs. 3 T | <0.0001 | <0.0001 | Yes |
| | 1.5 T vs. 3 T | <0.0001 | <0.0001 | Yes |
| Parallel | 0.5 T vs. 1.5 T | 0.2801 | 0.4202 | No |
| | 0.5 T vs. 3 T | 0.2262 | 0.4202 | No |
| | 1.5 T vs. 3 T | 0.8874 | 0.8874 | No |